POLITECNICO DI TORINO

Corso di Laurea Magistrale
in Ingegneria Meccanica

Tesi di Laurea Magistrale

Investigation on mixing process in a direct injection NG engine by means of PLIF investigation and data post-processing optimization

Supervisors:
Prof. Daniela Misul
Prof. Mirko Baratta

Candidate:
Wang Zhengwei

October 2018

Abstract

In order to realize low carbon emissions, the development directions for automobiles are hybridization and alternative fuels. The hybrid is complex both for structures and control, and has a limited emission reduction. Alternative fuels not only reduce Well-to-Wheel emissions, they are also sustainable. Otherwise, we can increase engine efficiency and compensate for reduced power through the technologies already used in traditional engines, including turbocharger, EGR, direct injection etc.

Natural gas is one of the most promising alternative fuels for cars applications with low carbon emissions. Natural gas is available all over the world, and has perfect intrinsic properties, including high detonation resistance, low carbon content and a wide range of stoichiometric operations. The high H/C ratio also offers benefits in terms of emissions. As for the safety, natural gas has a limited flammability and is lighter than air. In the ambient condition, natural gas is gaseous. Therefore, the direct injection and turbocharger technologies are fundamental for CNG applications in the future. In addition, natural gas has a high-octane number, which allows a higher compression ratio to increase the engine efficiency. And particularly in combination with the most of technologies have been already applied in current cars, for examples, variable valve actuation (VVA), turbulence in intake port and alternative combustion cycles. These applied technologies can effectively compensate for the reduction in power of the natural gas engine.

The speed and quanlity of the engine combustion are based on the control of the air/fuel mixing process before ignition. Therefore, the quantitative and quanlitative measurement techniques of the mixture formation between air and fuel are fundamental for increasing engine efficiency and power. PLIF (Planar Laser-Induced Fluorescence) is a technology has been successfully applied for optical non-invasive investigation of the fuel distribution in optically accessible engines. Under IC engine condition, the signal spectrum of the emitted PLIF and its intensity are influenced by pressure, temperature and gas composition, which makes the quantitative and quanlitative interpretation of LIF signals challenging.

The activity presented in this thesis concerns analyzing the mixing of natural gas during the compression stroke using PLIF technology. The engine considered in the study is a prototype specifically dedicated to CNG, and equipped with a system of direct injection, high tumble intake port and high compression ratio. And experimental activities and data measurements were carried out by AVL LIST GmbH. This thesis mainly contains two parts. The first part of the work is the study of the cylinder temperatures during the compression stroke using the TPA approach of the GT-Power Software, then compares the temperatures and pressures between fired and motored conditions during the compression stroke. Next, the second part of the work concerns the CNG mixing analisis to the three different injection strategies for the partial load operating points through PLIF images processing.

Acknowledgments

I would like to thank my supervisors Prof. Daniela Misul and Prof. Mirko Baratta, it has been an honour working with them during the 8 months of work, and they give me a lot of help and support.

I am also grateful to Ing. Jiajie Xu for the discussion of the work and his valuable help in processing and analyzing experimental data and calibration methodologies.

Contents

List of Figures

List of Tables

Symbols

Symbols

α	air fuel ratio
$\alpha_s t$	Stoichiometric air fuel ratio
η_u	Indicated Efficiency
λ	lambda: relative air fuel ratio
λ_V	Volumetric Efficiency
ν	Frequency
rho	Density
σ	Standard Deviation
φ	Equivalence Ratio
D	Bore
E	Energy
H_i	Heat Value
k	Relative rate
L	Stroke
$\dot{m}$	Mass Flow Rate
N	Number
n	Number density
P	Pressure
ppm	part per million
R	Gas Constant
rpm	Revolution Per Minute
S_0	Ground sate
S_1, S_2	Single excited state
T	Temperature
T_1	Triplet excited state

Indices

0	Nonimale
a	Air
abs	absorption
comp	Compression
em	emitted
EXH	exhaust
f	fuel
fl	fluorescence
ic	Internal conversion
id	ideal
INT	intake
isc	Intersystem crossing
max	maximal
methane	Methane
min	minimal
nr	non-radiative
oxy	Oxygen
O2	Oxygen
q	quenching
st	Stoichiometric
SV	Stern-Volmer
tot	Total
Val	Valve
Vol	Volume

Abbreviations

AFR	Air Fuel Ratio
BSFC	Brake Specific Fuel Consumption
BTDC	Before Top Dead Center
CA	Crank Angle
CCD	Charge Coupled Device
CNG	Compressed Natural Gas
CoV	Coefficient of Variation
CR	Compression Ratio
DI	Direct Injection
DING	Direct Injection Natural Gas
DOI	Duration Of Injection
EGR	Exhaust Gas Recirculation
EIVC	Early Intake Valve Closing
EOI	End Of Injection
EU	European Union
FAR	Fuel-Air Ratio
GDI	Gasoline Direct Injection
GHG	Greenhouse Gases
HTM	Heat Transfer Multiplier
IC	Internal Conversion
ICE	Internal Combustion Engine
IMEP	Indicted Mean Effective Pressure
ISC	Intersystem Crossing
IVC	Intake Valve Closure
K	coefficient
KrF	Krypton Fluoride
LDV	Light Duty Vehicle
L.H.V	Lower Heating Value
LIF	Laser Induced Fluorescence
MCE	Multi-Cylinder Engine
NG	Natural Gas
NGVs	Natural Gas Vehicles
OHC	Overhead Camshaft

PFI	Port Fuel Injection
PFP	Peak Firing Pressure
PMAX1	Pick Firing Pressure of Engine Cylinder
PL	Part Load
PLIF	Planar Laser-Induced Fluorescence
PMEP	Pumping Mean Effective Pressure
RON	Research Octane Number
SCE	Single-Cylinder Engine
SCTE	Single-Cylinder Transparent Engine
SNR	Signal-to-noise ratio
SOI	Start Of Injection
SSE	Sum of Squares of Error
SSR	Sum of Squares of Regression
SST	Sum of Squares of Total
TDC	Top Dead Center
TE	Transparent Engine
TEA	Triethylamine
TMA	Trimethylamine
TPA	Three Pressure Analysis
UV	Ultra Violet
VR	Vibrational Relaxation
VVA	Variable Valve Actuation

Chapter 1

Introduction

1.1 Background e Motivation

For a long time, fossil fuels, such as gasoline and diesel, have been the main source of energy for automobiles. As an unsustainable energy source, fossil fuels also bring many drawbacks, especially environmental pollution. Carbon dioxide (CO_2) emissions of vehicle are a major source of greenhouse gases (GHGs).

In Europe, the transport sector contributes nearly a quarter of greenhouse gas emissions, which is the main cause of urban air pollution. Compared with other sectors, the transport sector emissions have not continued to decline, and the gap is gradually increasing. Emissions only began to decrease in 2007, but it is still higher than 1990. (Figure 1.1)

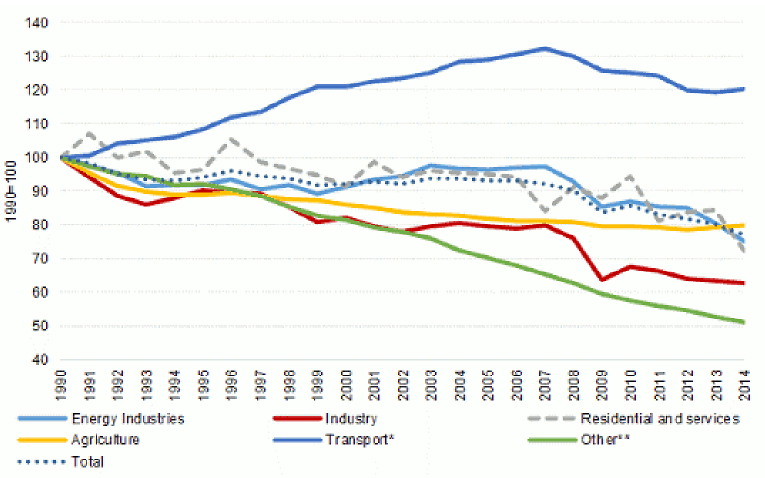

Figure 1.1: Transport Energy Demand

With the global shift to a low-carbon emission, in order to ensure Europe remains competitive and able to responde to the increasing mobility. In the Paris Agreement on climate change wihich adopted in July 2016, a low carbon emission strategy became the focus of future car development [1].

Main elements of the strategy:

- Increasing the efficiency of the transport system and further encouraging the shift to lower emission transport modes.
- Speeding up the deployment of low-emission alternative energy for transport, such as biofuels, electricity, hydrogen and renewable synthetic fuels.
- Moving towards zeros-emission vehciles.

To achieve these goals, the three-term plans need to be realized and implemented. In the short term (2020), the 2020 package sets three key targets: 20% reduction in greenhouse gas (1990 levels), 20% of the energy from renewable sources, and 20% improvement in energy efficiency. In the medium term (2030), at least 40% reduction of greenhouse gas emissions (from 1990 levels), at least 27% of renewable energy, and at least 27% improvement in energy efficiency. In the long term (2050), the EU should reduce greenhouse gas emissions to 80% below 1990 levels and gradually realize low-carbon economy [1].

In order to realize sustainable mobility in Euope, natural gas has received more attention as the most promising alternative fuel. In the term of safety, natural gas has a limited flammability and is lighter than air. Natural gas has perfect intrinsic properties, including high detonation resistance and low carbon content, which properities can reduce emissions while achieving high efficiency through technologies. In this context, GasOn project aims to develop advanced CNG only, mono-fuel engines able to comply with the "2020+" CO_2 emission targets, claiming the 20% CO_2 emission reduction with regard to current best in class CNG vehicle segment by segment, to fulfill the new homologation cycle and to guarantee a low fuel consumption even in real driving conditions [2].

1.2 Natural gas as the ICE fuel

1.2.1 Properties of Natural gas

Natural gas (NG), which is mainly composed of methane (CH_4), is an alternative fuel to effectively limit CO_2 emissions. Because NG has little or no heavy hydrocarbons, olefins and alkynes, therefore, it contains less carbon than fossil fuels, such as gasoline and diesel. Moreover, the NG does not contain aromatic compounds e higher H/C molecular ratio, therefore the precursors of particulate emissions from its combustion is almost non-existent.

Usually, the natural gas is compressed to less than 1% of the volume at the normal atomospheric pressure, and it is stored and distributed at a pressure around 200-248 bar in rigid containers usually cylindrical or spherical. After this process, natural gas is changed to Compressed Natural Gas (CNG). In table 1.1, it describes the main properties of the compressed natural gas compared to those of gasoline and diesel. CNG has a high flammability (4.3% to 15.2% volume in air), high auto-ignition temperature (540 °C), and its density is lower than air (molar mass of air: 28.96 g/mol). These properties guarantee high safety for natural gas applications.

CNG has a high knock resistance, since the estimated RON (Research Octane Number) index of methane is close to 130, the low knock sensitivity allows to increase the engine thermal efficiency through a higher compression ratio (from 13:1 to 14:1) and the knock risk can not be considered. The low heat value (L.H.V) of CNG is higher than gasoline and diesel, which can release more energy for the same kilogram.

Properties	CNG	Gasoline	Diesel
Octane number	120-130	85-95	45-55
Molar mass (g/mol)	17.3	109	204
Flammability limit in air (vol% in air)	4.3-15.2	1.4-7.6	1-6
Auto-ignition temp. (°C)	540	258	316
L.H.V (MJ/kg)	47.5	43.5	42.7
Stoichiometric (A/F)	17.2	14.7	14.6

Table 1.1: Physical & Chemistry properties of CNG vs. gasoline and diesel

1.2.2 Environmental and economic benefits

Because CNG contains lower carbon compared to other fossil fuels, such as gasoline and diesel, in theoretical CNG as energy resources of the internal combustion engine (ICE) has a 23% reduction in CO_2 emissions compared to gasoline in stoichiometric condition. NEDC cycle simulations using a DING engine powered Light Duty Vehicle (LDV) shown a 27% reduction of CO2 emissions compared to the same vehicle equipped with a Diesel engine, marking CNG engines credible alternatives for the European market [3]. From the point of view of the well-to-wheel emissions, natural gas reduces GHG emissions around 15 to 23% compared to diesel or gasoline. In addition, CNG has a lower combustion temperature, which can reduce around 50% of the emission of NO_X. Natural gas significantly reduces the formation of particulates, because CNG is composed mainly of methane which does not contain any aromatic compounds. For the noise pollution, the sound pressure level of CNG is lower than that of a diesel engine, causing 90 percent less noise [4]. That means noise pollution can be reduced significantly.

In the term of economic benefits, the price of natural gas is about half of that of oil in Europe, if from the point of view of kilometer costs, the costs of natural gas vehicles are about 45% of those of gasoline vehicles for the same kilometers ([5], [6]). Moreover, Gasoline or diesel engines have reduced lives, due to the carbon build-up. However, the natural gas engines do not have build-up of carbon and thanks to the clean-burning attributes of natural gas, therefore, the NGVs (Natural Gas Vehicles) usually have longer engine life than the most gasoline-powered vehicles [7]. Thus, the natural gas engine vehicles have a longer maintenance cycle, in other words, a lower maintenance costs than gasoline vehicles which further reduces the cost.

1.2.3 Drawbacks of CNG engine

Natural gas is a gaseous fuel in the environment. On the one hand, natural gas takes up a part of the combustion chamber volume, leading to a lower quantity of trapped air. On the other hand, gaseous fuel no longer has the evaporation process, the air temperature can not be reduced by subtracting the heat from the air, which means it is not possible to increase the trapped air by increasing the air density. Thus, the volumetric efficiency of the natural gas engine is lower than that of the gasoline engine. Because the natural gas density is lower than that of the air, the jet momentum of the natural gas is lower during injection, leading to the reduced penetration [8]. A direct influence is the degree of mixing between air and natural gas before ignition. Thus, the charge motion of trapped air is very important for mixing.

Lower volumetric efficiency and non-homogeneous mixing between air and natural gas, causes a limited flame propagation speed during the combustion. The low flame propagation speed of the natural gas decreases the thermal efficiency of the CNG engine, especially in part load operations in which the charge motion is very weak and the turbulence of the trapped air dissipates mainly before ignition. Consequently, comparison with the gasoline engines, the natural gas engine has 18-22% lower brake specific fuel consumption (BSFC) and 15-20% lower brake power [9].

1.3 Technologies using in CNG engines

The purpose of the technologies is to overcome the CNG engine drawbacks that have already been referred to in the previous section. Such as, lower trapped air volumetric efficiency, lower flame propagation speed and non-homogeneous mixing, specifically in part load operations.

1.3.1 Direct injection

Direct injection is a mature technology that already has been used in gasoline engines, in which, the fuels directly inject in the combustion chamber. The Figure 1.2 illustrates the schematic of mixture preparation of DI engine. Direct injection spark ingnition (DISI) engines offers a better power output and performance in full load operations and a good economic fuel in part load operations. Because fuels are not introduced from the intake port, DI has a high volumetric efficiency than port fuel injection (PFI). Furthermore, mature electronic control technology offers good fuel consumption management.

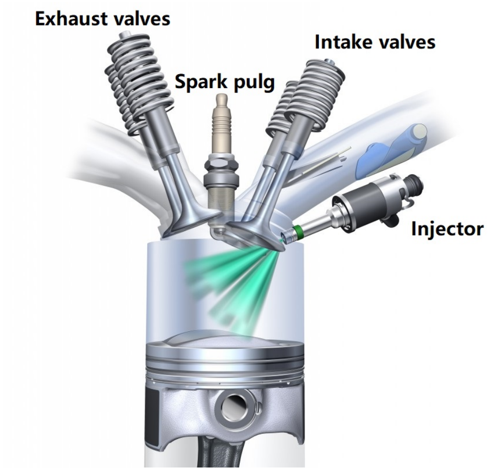

Figure 1.2: Direct injection mixture preparation system

The DI mixing formation is very flexible, there are two types of mixing formation for when Direct Injection: homogeneous mixture and stratified mixture ([10],[11]).

- he stratified mixture could be realizing a rich loacl mixture near the spark pulg by a late fuel injection strategy into the cylinder during compression stroke. At the idling and part load operations, the burn lean mixtrue gives a better fuel economy and reduce the knock limitation level due to lean mixture near the cylinder wall.

- he homogeneous mixture is achieved by an early fuel injection in the intake stroke, which provieds a sufficient time for the mixture formation and avoids the voulmetric efficiency loss.

However, in the stratified mixture mode, the mixture formation of the natural gas and air near the spark plug is different for each cycle, and which is very sensitive to various factors such as the intake air flow and pressure, and the injection timing ([12], [15]). Therefore, the DI homogeneous mixture mode can be believed to an approach to improve the NG engine combustion characteristic. Because, the natural gas is injected before the intake valve closing (IVC), which ensure a longer fuel-air mixing time and increase the in-cylinder turbulence by the natural gas jet introduced by injector.

1.3.2 High compressione ratio

CNG has a high knock resistance, since the estimated RON (Research Octane Number) index of methane is close to 130, the low knock sensitivity allows to increase the engine thermal efficiency through a higher compression ratio (from 13:1 to 14:1) and without the knocking risk.

From the point of view of the theory of spark ignition and compression ignition engine, which are Otto cycle and Diesel cycle, the Otto and Diesel cycle efficiencies are equal to:

$$\eta_{id_{Otto}} = 1 - \frac{1}{\varepsilon^k - 1}; \tag{1.1}$$

$$\eta_{id_{Diesel}} = 1 - \frac{1}{\varepsilon^k - 1} \cdot \frac{\tau^k - 1}{k(\tau - 1)}; \tag{1.2}$$

Where:
ε: the compression ratio
k: the heat capacity ratio (k=C_p/C_v)
τ: the cut-off ratio (ratio between the end and start volume for the combustion phase)

The Figure 1.3 shows the ideal cycles efficiencies vary with the compression ratio. Because the compression ratio of the Diesel cycle (15 ∼ 23) is higher than that of the Otto cycle (8 ∼ 12), therefore, the ideal efficiency of the Diesel cycle is higher than that of the Otto cycle. Furthermore, by increasing the compression ratio, the ideal cycle efficiency increases.

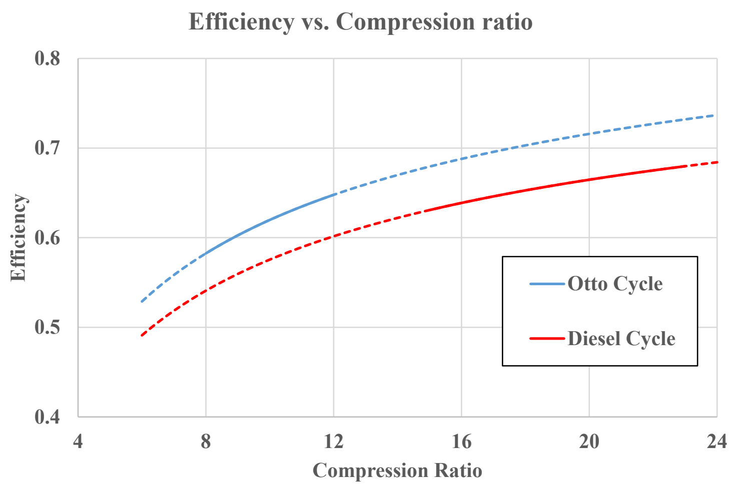

Figure 1.3: The thermal efficiency of Otto and Diesel cycle

The Figure 1.4 shows the LogP-LogV diagram of the spark ignition engine in different compression ratio. Increasing the compression ratio from 9 to 11, the power loop and pumping loop increase simultaneously, but the power loop increase is dominated. Thus, the increase of compression ratio increases the work of the cycle, in other words, it increases the engine thermal efficiency.

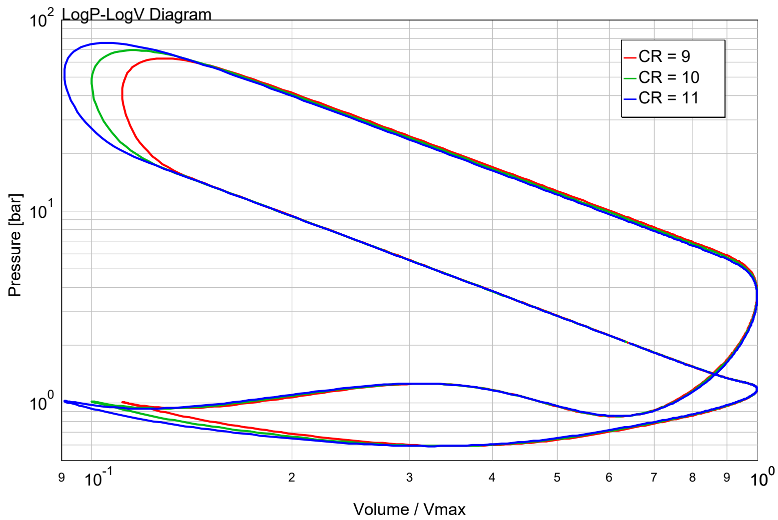

Figure 1.4: LogP-LofV diagram in different compression ratio

1.3.3 Early intake valve closing

For the conventional engines, engine load operations is controlled by the throttle. At the part load operations, the trapped air mass is limited by the partially opened throttle. However, this results in a significant increase in the pumping loss during intake/exhaust stroke and poor fuel economy.

The variable valve actuation (VVA) system is an intake valve throttled mode, which eliminates the throttle valve, and controls the trapped air mass inside the cylinder by changing the duration and height of the intake valve opening in the different engine load operations. Early intake valve closing (EIVC) is a strategy of VVA system, in which the intake valves close early. In part load engine operations, lower amount of charge is required, EIVC can effectively reduce the pumping loss during intake stroke. The Figure 1.5 is a direct comparison the pumping loss between EIVC system and conventional throttling at part load operation. The part load fuel consumption of unthrottled operations using the EIVC have a 7% fuel consumption improvement compared to that of conventional engine [13].

However, the EIVC system leads to a lower in-cylinder turbulence especially at low load operations, because the closed early of intake valves results in a lower trapped air mass and a lower kinetic energy of the intake air. The lower in-cylinder turbulence of intake air has a negative impact on the mixture formation, and the dissipation of the kinetic energy of intake air results in a lower flame propagation speed during combustion [14].

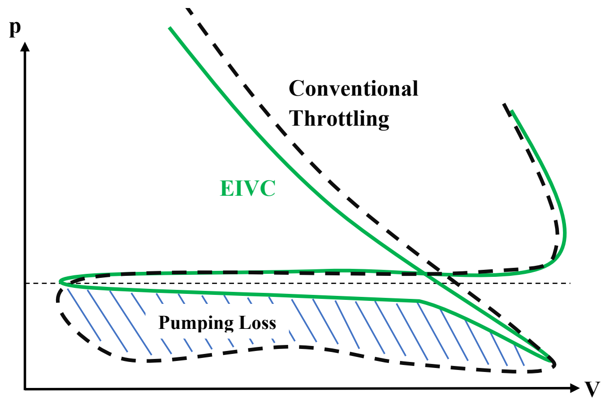

Figure 1.5: Pumping loss of EIVC system and conventional throttling at part load

1.3.4 Tumble formation

The turbulence dissipation caused by the EIVC system can be solved by intake port shape modifications. Tumble is a rotary motion on a plane passing through the cylinder axis, which begins to form during the intake stroke and is then amplified at the end of the compression phase (Figure 1.6).

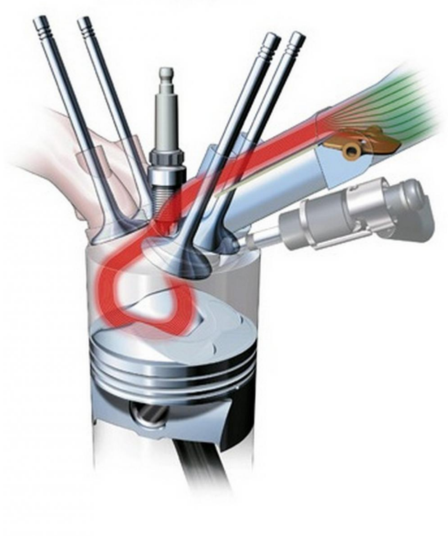

Figure 1.6: Tumble flow in engine cylinder

In order to intensify the tumble, the intake ports must draw directing the air flow to the area below the exhaust valve. A subsequent important action to support and amplify the tumble is the movement of the piston in the second part of the compression stroke. The Figure 1.7 shows the tumble flow in three different types of intake ports during the second part of intake stroke and the first part of the compression stroke. It is indicated that the straight intake ports with a suitable inclination angle with the cylinder axis can effectively form high tumble flow.
The main advantage of the tumble is the ability to generate turbulence towards the

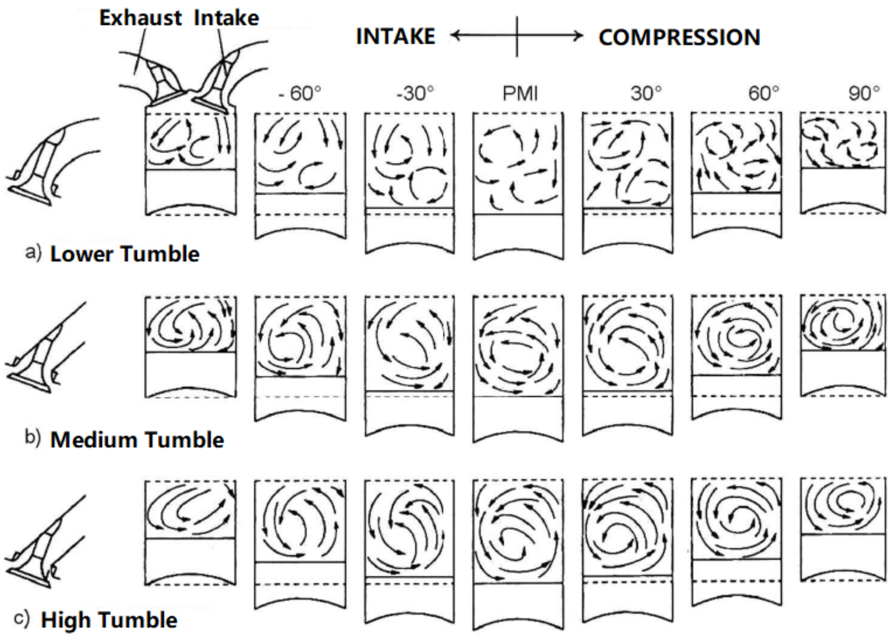

Figure 1.7: Tumble flows in three different types of intake ports

end of the compression stroke (the intensity up to 2-4 times that of the traditional intake ports), in order to accelerate and stabilize the combustion process.

1.3.5 Direct injection NG engines

Since the direct injection system brings a lot of potential to the CNG engines, the direct injection natural gas (DING) engine will be a basic engine for the future research and development of the CNG engines.

The direct injection not only solves the low volumetric coefficient caused by gaseous of natural gas in environmental conditions, but also increases the mixing between natural gas and air thanks to the high pressure of the injected natural gas. Furthermore, the introduction of a high compression ratio effectively increases engine thermal efficiency. For the problems of lower engine thermal efficiency and limited flame propagation speed in part load operations, the technologies of EIVC and high tumble intake ports not only reduces pumping loss during intake and exhaust strokes, but also high-tumble intake air flow enhance effectively flame propagation speed during combustion and increases engine thermal efficiency.

All of these technologies using in the regenerated CNG engines, not only overcome the drawbacks of the CNG as the fuel, but also the performance reaches the same level with the gasoline engines. More importantly, it is lower engine emissions than gasoline and diesel engines.

Chapter 2

Project executive summary

The activities are the investigation the mixing formation in the combustion chamber of an engine adopted high tumble intake port system and a steep injector mounting angle with the different injection strategies. The transparent engine (TE) provides the possibility to visualize the mixing process under close to real engine conditions. As for the first measurement campaign the mixture formation process itself was investigated with the help of LIF (Laser Induced Fluorescence) measurement method.

2.1 Design and procurement of transparent engine

The single-cylinder transparent engine (SCTE) is modified by by the 1.0L 3-cylinder engine. Because the mixing formation investigation is in the cylinder, therefore, intake/exhaust ports, valves, injector, and the combustion chamber geometry (bore and stroke) are kept the same as in the base engine. The main modification is the glass liner cylinder for the optical access from the side. The Figure 2.1 is illustrated the SCTE cylinder heads shown in comparison from the combustion chamber side.

The SCTE engine head based on the 1.0L 3-cylinder engine is characterized by the high tumble intake port. In part load conditions, EIVC (early intake valve closing) reduces the pumping loop dissipation, but also reduces the charge motion of the fresh air. Strong tumble formed by the intake port can compensate for this reduction by EIVC. This air turbulence will also increase the mixture formation between natural gas and air when the piston rises to TDC (Top Dead Center). The 3-cylinder based engine configuration features a rather steep injector mounting angle. The Figure 2.2 shows the injector and intake port configurations.

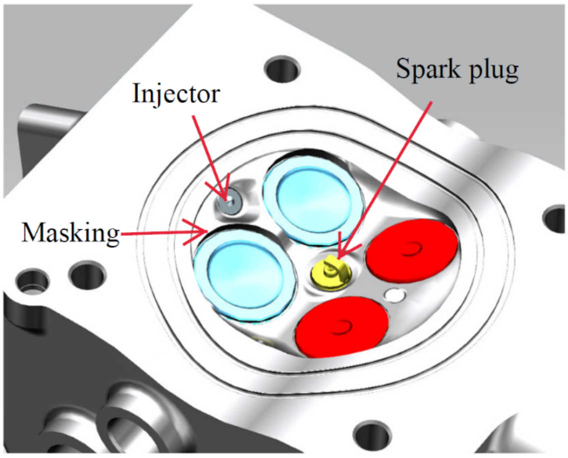

Figure 2.1: Transparent engine cylinder head (view from combustion chamber side)

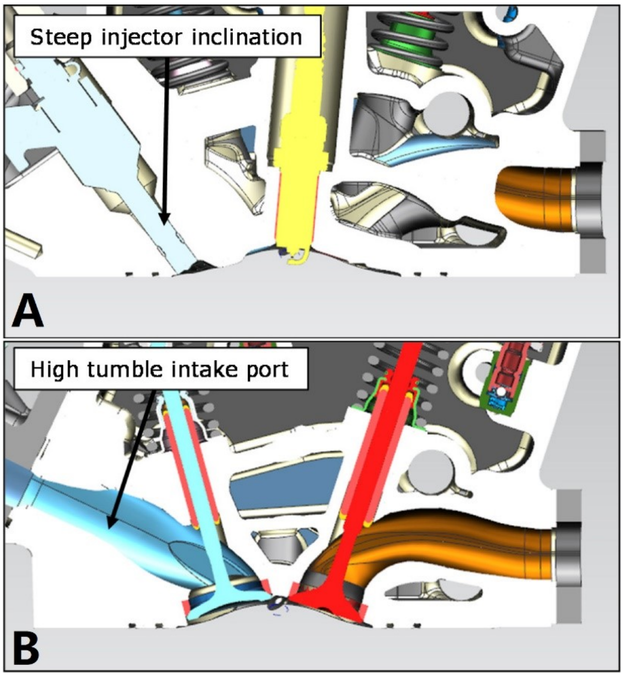

Figure 2.2: Cylinder head configuration (A: Injector; B: Intake port)

As regards the SCTE Valve train, the intake side must be redesigned to replace the MultiAir system present on the MCE by a traditional mechanical cam shaft. While, the exhaust side was carried over directly from the MCE. The Figure 2.3 shows the mechanically driven valve trains of the SCTE engine configuration. And the Figure 2.4 shows the TE intake/exhaust valve lift profiles for TE configurations.

Because the PLIF investigation is needed, the transparent engine piston is not the conventional one, it is divided into 2 parts. The upper part has no piston rings in order to avoid stain and/or damage the class liner. While the lower part it is like a normal piston, and allows the piston to be sealed and guided. As a consequence, the top-land volume is superior to that of a real engine, but this variation has a

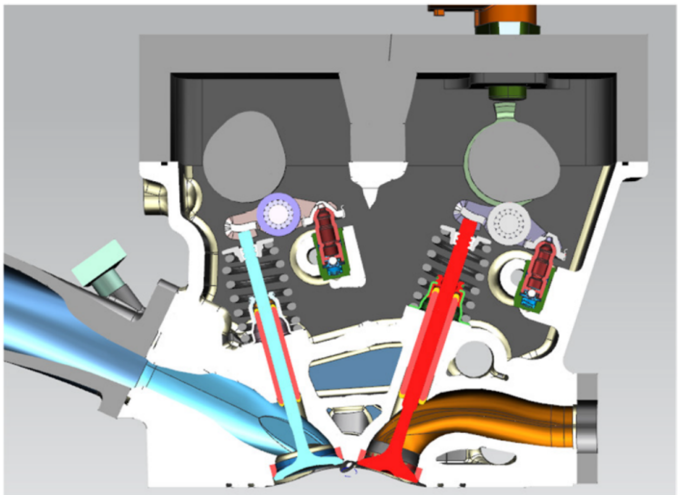

Figure 2.3: SCTE valve train layout

negligible impact on the mixture formation process. The increasing of top-land volume indirectly increases the dead volume, the SCTE compression ratio has been reduced about 2 units, from 13.0 to 11.0. It also reduces the engine peak firing pressure (PFP) and thus avoid engine damage [15]. Since in the transparent engine measurement, the camera view through just the side of cylinder, the piston has a flat upper surface and is pure metal. The Figure 2.5 shows the piston design for the SCTE.

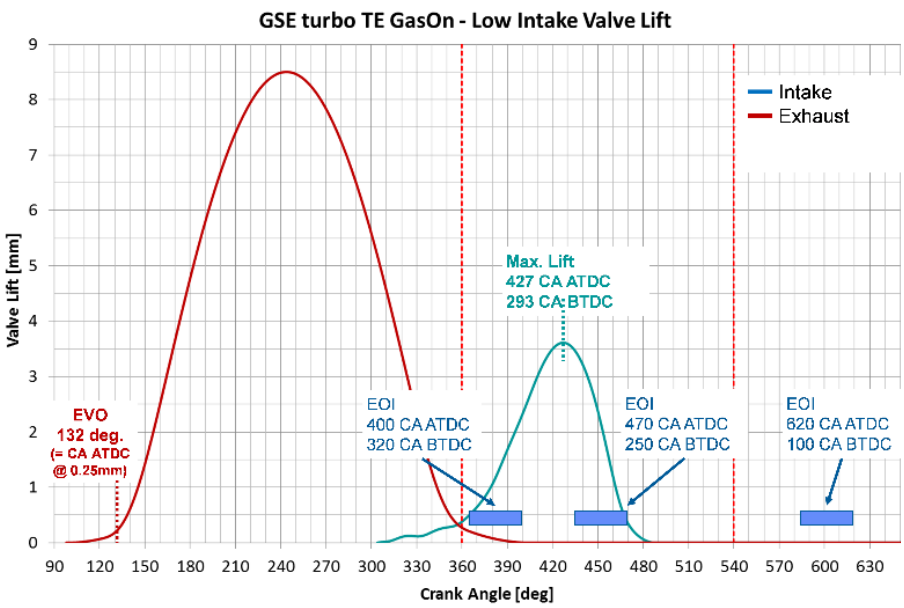

Figure 2.4: SCTE valve lift profile in part load operation

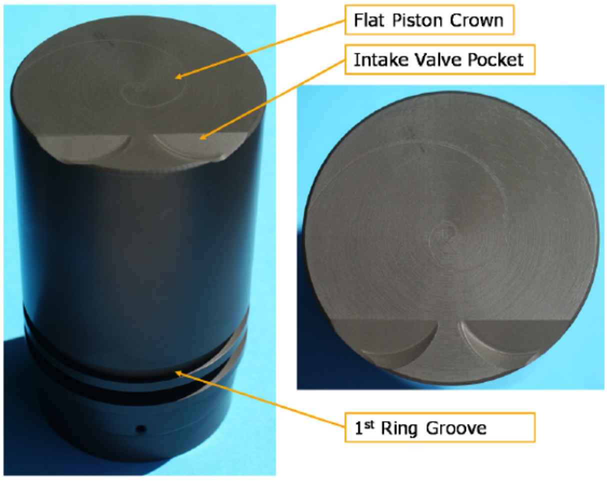

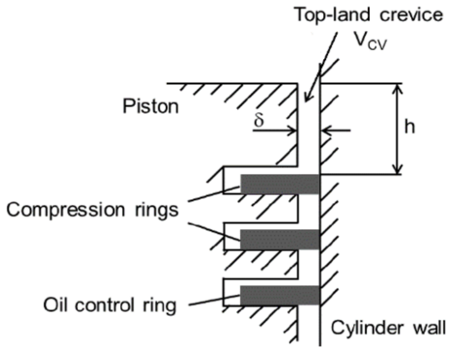

	Normal	SCTE
h [mm]	5 - 8	63

Figure 2.5: Piston for TE investigations

In the end, the Table 2.1 shows the parameters of the SCTE and the 3-cylinder base engine, and the Figure 2.6 shows an installed transparent engine on the test bed. The redesigned engine head for TE and cylinder glass liner for PLIF measurement can be seen from the Figure 2.6.

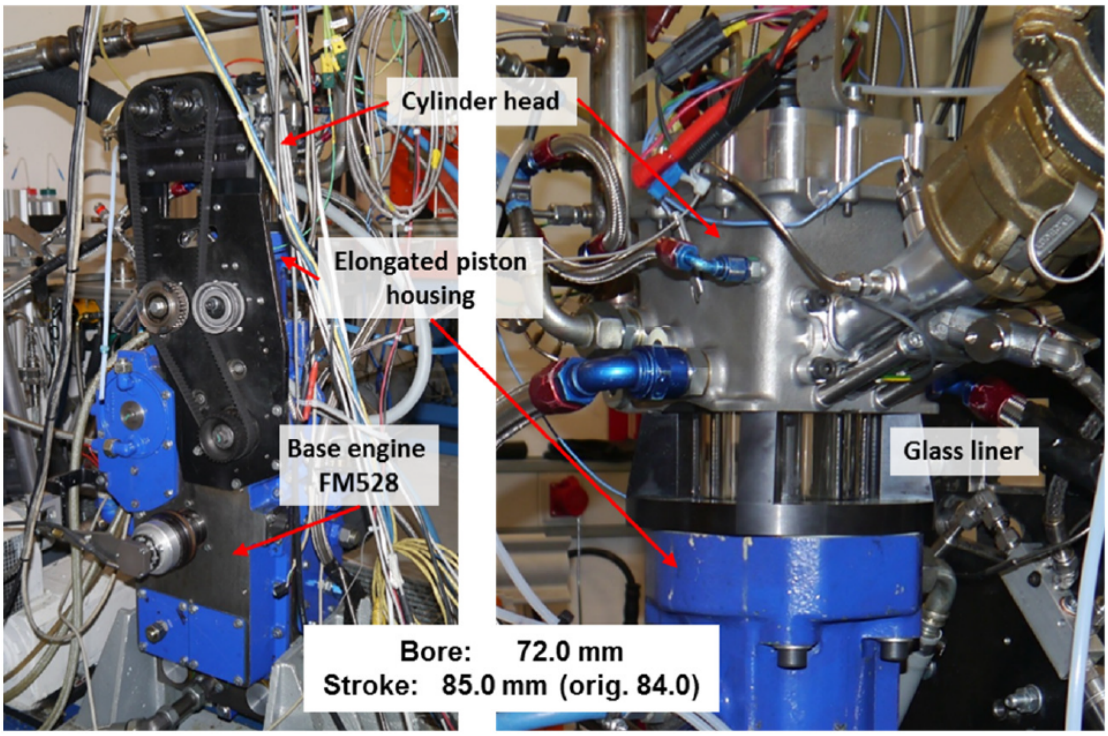

Figure 2.6: Transparent engine setup

Parameters	base engine	SCTE
Bore $[mm]$	72	72
Stroke $[mm]$	84	85
Conord Length $[mm]$	160	160
Top land heigjt $[mm]$	-	63
Displacement $[mm^3]$	342006.3	346077.8
Compression Ratio	13	11

Table 2.1: The parameters of the SCTE engine and SCE engine

2.2 Injection strategies in part load operation

In part load engine operation, the mixture formation is very weak due to low engine speed and intake system operation with EIVC. The piston speed is proportional directly to the engine speed, in part load operation, a low piston speed reduces the turbulence during compression. While, the EIVC operation significantly reduces the charge motion during intake stroke. The reduced charge motion and turbulence during intake and compression taken the negative effects for mixture formation and combustion speed.

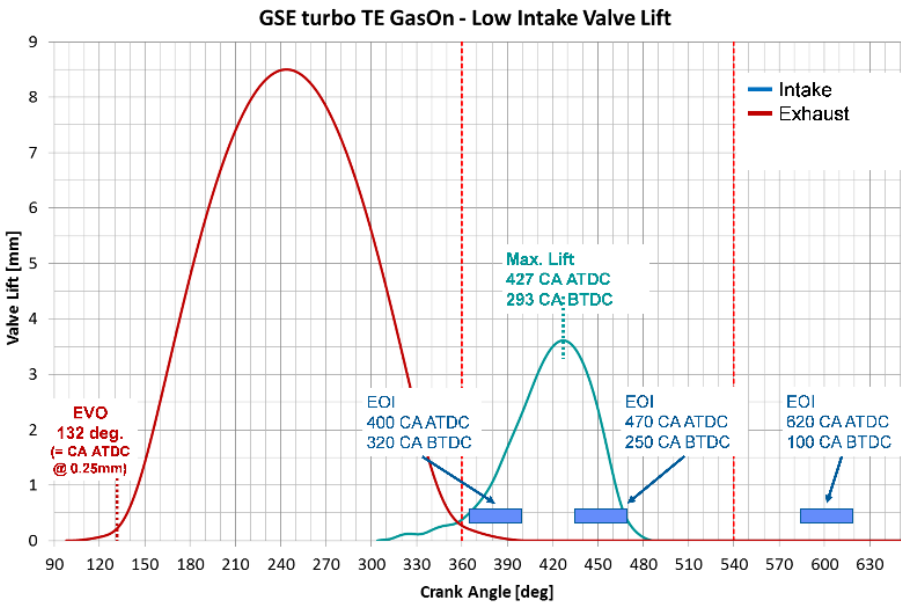

Figure 2.7: Valve lift profiles & Injection timing @ 2000 rpm/low part load

In the experimental process, in order to compare the effect of injection timing to the mixture formation, three different injection strategies are carried out in the part load operation. A schematic can be found in the Tigure 2.7 and each strategy can be described by its respective EOI-timing (End Of Injection), as follows:

- Case 004: EOI early in intake stroke (early EOI or EOI320)
  Injection is very early when the intake stroke beginning, the piston movement is very weak, and allows a longest time for the mixture.

- Case 005: EOI at the end of intake phase (EOI250)
  Injection ends around the IVC (Intake Valve Closing), the piston movement is very strong, and the mixing time is reduced compared to Case 004 (Early EOI).

- Case 006: EOI in compression stroke (EOI100)
  Injection appears very late into the compression stroke, the piston movement almost has no effect to the charge motion, and the mixing time is very late.

2.3 LIF Measurement of mixing process

For LIF (Laser Induced Fluorescence) measurement, AVL uses a double-sided laser plane, this configuration means that the laser is split into 2 beams and the lasers are directed towards the engine cylinder from two opposite sides, the Figures 2.8 shows the optical arrangement for 'double-sided' PLIF. The reason for this configuration is that the shadows of the piston can be reduced to a minimum, and guarantee a high quality and quantity of illumination of the pent-roof combustion chamber, especially for crank angles near the top dead center (TDC).

The laser source is Krypton fluoride (KrF) EXCIMER Laser (EXCERED diMER LASER gas) with a pulse length of 20ns and wavelength of 248nm. This laser is divided by the Beam splitter, and driven to the cylinder glass liner by means of lenses and mirrors.

The PLIF images are taken at defined crank angle positions, using an intensified CCD camera with an image-intensifier quantum efficiency of around 20% at 300 nm. The ICCD camera is fitted with a UV-compatible Micro Nikkor lens [7].

With regard to the tracer, the transparent engine was fuelled with a mixture of natural gas and 400 ppm in volume of trimethylamine (TMA, C_3H_9N), in order to allow the PLIF visullization. TMA is a more suitable trace in the LIF investigations of natural gas injection ([8],[9]). Since under environment conditions TMA is a gaseous tracer, and its the branched molecular structure gives rise to a large number of excitable energy states, for this reason, a broadband excitation can be realized under excimer laser at 248 nm of wavelength.

Because of CNG injection sensitivity, a cycle-resolved experimental analysis is carried out by AVL in order to reduce the cyclic variability of the jet. Therefore, 36

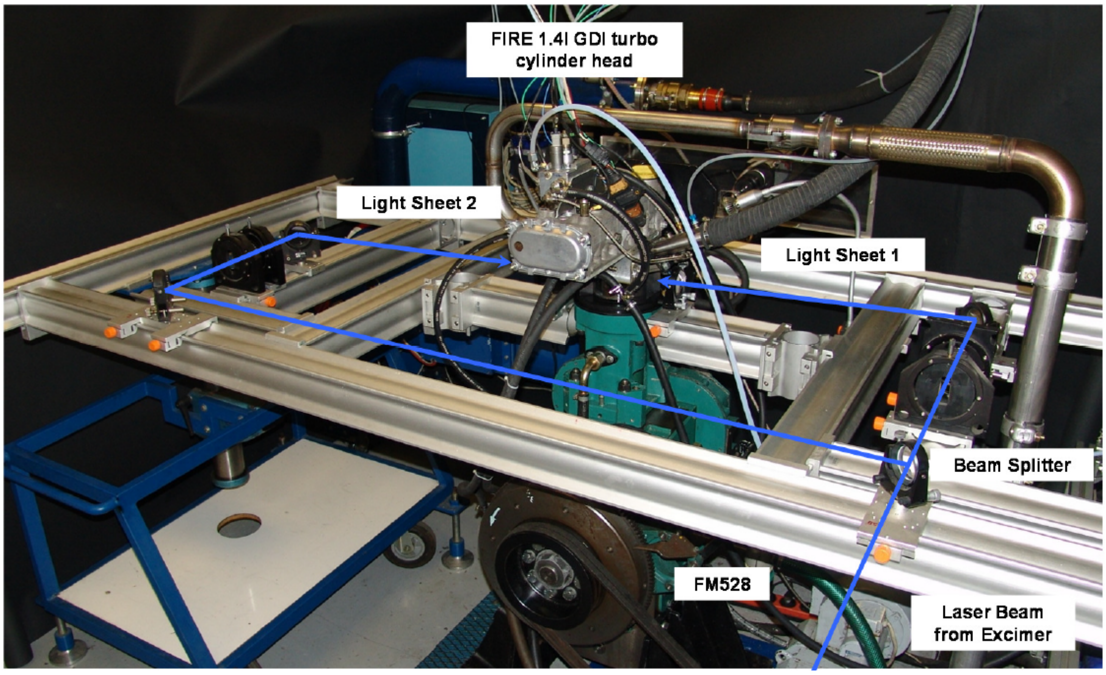

Figure 2.8: Laser beam routing for double sided PLIF measurement

single images were acquired for each crank angle position for each case both mtored and fired condition. The intensity of the PLIF image that is taken by the ICCD camera represents the local fuel density in the engine cylinder. Furthermore, reference images with homogeneous mixture and background images with same crank angle positions from an empty cylinder are already taken. This can eliminate the reflections effect by the glass liner and other disturbing noise in the PLIF images processing and calibration. All of images are saved in the AVL VisioScope software for later viewing and post processing

In the motored condition, reference intensity with the known equivalence ratio can be obtained from the process of reference images subtracting of the background images for same CA position. These density references will be used to calibrate the equivalence ratios in the fired conditon.

2.4 Aim and Overview of the Thesis

Main aim is to investigate the leading mechanisms of either mixing process and evaluate the interactions between base charge motion and turbulence introduction via the high velocity fuel gas jet by identifying the influence of three diffrerent injection strategies for the mixing formation process between direct injected natural gas and air in the combustion chamber for an engine worked at the part load points.

The PLIF measurement is an indispensable experimental process. In the engine conditions, the parameters influencing fluorescence are very complex. Such as, cylinder temperature, pressure and gas composition. The cylinder pressure can be measured directly from the sensor during experiment. Because engine temperature is an unknown value, therefore, the work of the thesis is composed of two parts: Numerical simulation of engine temperature and PLIF images processing.

The first part of the work is numerical simulation of engine temperature. The simulation process uses the TPA approach of the GT-Power sofeware. Firstly, the experimental data (cylinder pressure, intake/exhaust pressure and temperatures, air flow rate, fuel temperature...) are processed from AVL IndiView as the input data of the TPA model simulation, while the TPA model is based on DING single cylinder engine. Then, the TPA model can be corrected and validated by calibrating the air flow rate (or volumetric efficiency), until the simulated data (air flow rate, LHV, IMEP, compressione slop ...) correspond to the experimental data. Because this single cylinder engine is not a conventional engine, therefore, the calibration process is very important to obtain the correct temperature. In the end, the temperatures in motored and fired condition are obtained from the TPA Model. These temperatures are the input data for analyzing in the PLIF images cabiration.

The second part of the work is PLIF images processing and calibrating the equivalence ratio. Firstly, in the motored condition, the equivalence ratio can not be measured by the lambda sensor, the equvalence ratio in motored condition can be obtained from ppm_HC which is measured by the sensor installed on the exhaust pipe Then, the PLIF intensity is obtained from the PLIF images by subtracting backgroud images at the same CA position. Using the motored PLIF intensity and the equivalence ratio, a relationship can be established, the variation of pressure and temperature can be considered. In the end, the equivalence ratio map of the fired PLIF imges can be calibrated from this relationship.

Finally, in order to obtain a high accuracy of equivalence ratio results, the influence of reflection by the glass liner and the influence of variations in engine cylinder pressure and temperature must be corrected. Therefore, the methodologies of the corrections of these influences are important to have a high accuracy of the equivalence ratio results, especially at the moment before ignition.

Chapter 3

Numerical Simulation of Engine Cylinder Temperature

The numerical simulation of cylinder temperatures uses the Three Pressure Analysis (TPA) approach of the GT-Power software. The first step is the processing of the experimental data to obtain the data input (Pressures, temperatures and air flow rates) of the TPA model, the second is the establishment of the Single-Cylinder Engine (SCE) TPA model, and the last step is calibration of the SCE model to match the data experimental data and obtain cylinder temperatures in motored and fired conditions.

3.1 TPA approach introduction

GT-POWER is the software applied to analyze the simulation of the engine work process. The solution is based on one-dimensional fluid dynamics, which represents the flow and heat transfer in the pipes and other components of the flow of a motor system [18]. Three Pressure Analysis (TPA) is an approach available to determine the quantities that are difficult or impossible to measure directly, such as, apparent burn rate, residual fraction trapping ratio and valve mass flow profiles.

Data input required for TPA are three measured pressures: intake, exhaust and cylinder, therefore, an engine model including valves and ports at a minimum can be run the TPA approach. The simulation is run for multiple cycles, until the model has converged. As a result, the trapping ratio and residual fraction will be calculated from the model, which is why they are not needed as inputs [18].

The simulation methodology is a convergence process, as following:

1. A dummy burn is used in the first cycle, and pressure analysis is not performed.

2. From the second cycle, for each cycle, the first step is the reverse run simulation calculating the apparent burn rate through the measured cylinder

pressure profile. then, the second step is the forward run simulation impose the apparent burn rate calculated in the first step.

3. The TPA run is finished when steady state convergence is reached.

The advantage of this methodology is that all of the cylinder trapped quantities (the trapping ratio, the residual fraction and cylinder temperature) are predicted by the simulation. The downsides of this approach are that more measured data is required.

Required Data for TPA:

- Intake/Exhaust Port Pressure
- Cylinder Pressure
- Intake/Exhaust Port Temperature
- EGR fraction
- Fuel injection data
- Spark Timing

3.2 Experimental data elaboration

3.2.1 Experimental data introduction

All of the experimental data is saved in the AVL IndiView software, the experimental data are composed of two parts: Fired condition and motored condition. The Table 3.1 shows all cases operation, in the fired condition (3 cases), the engine is under the normal engine operation. While in the motored condition (7 cases), the engine is under 'closed loop' (or 'calibration loop') operation. The purpose of closed loop operation is to offer a series of calibration PLIF images to calibrate the equivalence ratio in fired condition.
In the fired condition, for each case, there are 15 tests and all 15 tests are working in the same engine condition. The difference is the CA position for PLIF images. The Table 3.2 shows all experimental tests in fired condition. The name of each test is composed of 4 parts: case number, engine operation, injection timing and PLIF images CA position.

For example, 005_PL_EOI250_-0600:

- Case: 005;
- Engine operation: Part Load (PL);
- End of Injection (EOI): -250;

- PLIF image CA position: -600

Fired Condition	Motored Condition
004_PL_PFI	007_PL_PFI
005_PL_EOI250	008_PL_PFI
006_PL_EOI100	009_PL_PFI
	010_PL_PFI
	011_PL_PFI
	012_PL_PFI
	013_PL_PFI

Table 3.1: All experimental cases

Case 004_PL_PFI	Case 005_PL_EOI250	Case 006_PL_EOI100
004_PL_PFI_-0400	005_PL_EOI250_-0400	006_PL_EOI100_-0400
004_PL_PFI_-0600	005_PL_EOI250_-0600	006_PL_EOI100_-0500
004_PL_PFI_-1000	005_PL_EOI250_-1000	006_PL_EOI100_-0600
004_PL_PFI_-1500	005_PL_EOI250_-1250	006_PL_EOI100_-0700
004_PL_PFI_-2000	005_PL_EOI250_-1500	006_PL_EOI100_-0800
004_PL_PFI_-2250	005_PL_EOI250_-1750	006_PL_EOI100_-0900
004_PL_PFI_-2500	005_PL_EOI250_-2000	006_PL_EOI100_-0950
004_PL_PFI_-2600	005_PL_EOI250_-2200	006_PL_EOI100_-1000
004_PL_PFI_-2700	005_PL_EOI250_-2300	006_PL_EOI100_-1050
004_PL_PFI_-2800	005_PL_EOI250_-2400	006_PL_EOI100_-1100
004_PL_PFI_-2900	005_PL_EOI250_-2500	006_PL_EOI100_-1150
004_PL_PFI_-3000	005_PL_EOI250_-2600	006_PL_EOI100_-1200
004_PL_PFI_-3100	005_PL_EOI250_-2700	006_PL_EOI100_-1250
004_PL_PFI_-3200	005_PL_EOI250_-2750	006_PL_EOI100_-1300
004_PL_PFI_-3300	005_PL_EOI250_-2800	006_PL_EOI100_-1320

Table 3.2: Experimental tests in fired condition

Experimental data of each test is mainly based on three basic parameters: Crank Angle, Cycle and Time. The Table 3.3 lists all the useful experimental data in the GT-Power simulation, and the experimental data is mainly composed of 3 categories: Pressure, Temperature and Flow rate.

Engine speed are the same for all three fired cases, and is 2000 rpm. Injection natural gas pressure (PGAS) is 8 bar for each test. All experimental data must be extracted, and need statistical analysis considering the problem of accuracy.

Based	Parameter	Description	Unit of measure
Crank Angle	P_ZYL1	Cylinder pressure profile	[bar]
	PSAUG	Intake pressure profile	[bar]
	PAUSP	Exhaust pressure profile	[bar]
Cycle	FlowSnoixAVG	Air flow rate	[kg/h]
	LambdaAVG	Lambda	[-]
	PMAX1	Maximum cylinder pressure	[bar]
	SPEED	Engine speed	[rpm]
Time	T_Exhaust	Exhaust gas temperature	[°C]
	T_Fuel	Fuel temperature	[°C]
	T_Intake	Intake air temperature	[°C]

Table 3.3: Useful experimental data for each test in AVL IndiView

3.2.2 Verification of the validity of experimental data

In the experimental process, for each test, the sensors have acquired the signals of 250 engine cycles, including intake/exhaust pressure and temperatures, cylinder pressure, lambda, etc.

Because in the first few cycles of the test, the engine is cold, it needs some time for preheating. In this time, the lambda of injection is high, little fuels are injected in the combustion chamber. Thus, the signals are not useful in this time. After the engine temperature is stable, the engine arrives the indicated operation by increasing the quantity of injected fuels. In addition, the natural gas pressure requires a time to adjust the indicated pressure (8 bar).

Therefore, in the experimental data, the sensors acquired 150 engine cycles signal, but the valid signals must be found for next steps. Lambda (LambdaAVG) and natural gas pressure (P_GAS) are the signals to determine the valid cycles, moreover the maximum cylinder pressure (PMAX1) can also decide the valid cycles.

For an example for Case 004_PL_PFI_-0400: The Figures 3.1 show the LambdaAVG, PMAX1 and P_GAS signals, at the first cycles, Lambda and G_GAS is very high, and PMAX1 is very low at a constant value about 11-12 bar. At a certain time or cycle, the fuel injection is increased, the engine operates under the condition of the case 004_PL_PFI. Because P_GAS is the injection pressure for each case, which is 8 bar, it takes a while to adjust the pressure. Therefore, for the case 004_PL_PFI_-0400 the cycles are validated at 150 to 245.

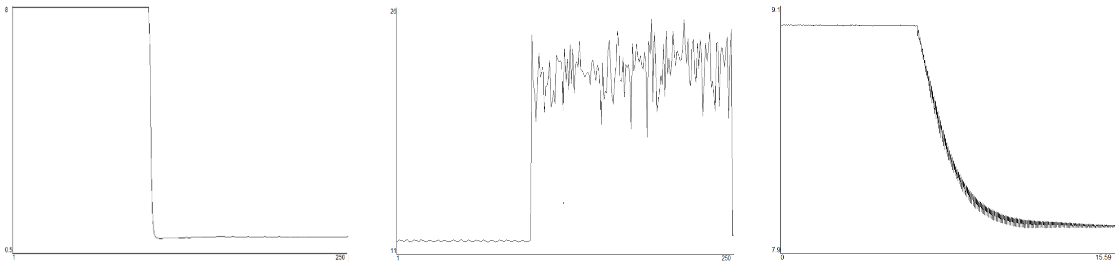

LambdaAVG - cycles **PMAX1 - cycles** **P_GAS - time**

Figure 3.1: The parameters for cycle and time validation

004_PL_PFI:

- LambdaAVG [cycle]: 107 to 250
- PMAX1 [cycle]: 101 to 248
- P_GAS [s]: 9 to 15.6

Cycle and time validation in case 004_PL_PFI:

- Cycle: 150 to 245
- Time [s]: 9.3 to 15

For each case, the valid cycles are different, therefore, we have to find the cycles valid for each case at the beginning of processing the experimental data. For the extraction of experimental data, case 004_PL_PFI is an example, the results of other cases are listed in the Appendix A.

3.2.3 Pressures

The pressure signals are the signals of crank angle-based, that is, the pressure trends vary along the crank angle position. There are three pressures to be sampled: intake/exhaust port and cylinder pressures.

3.2.3.1 Intake/Exhaust Pressure

In the intake/exhaust pressure measurement process, there are two types of pressure sensors to measure intake/exhaust pressure signals.

- Low response pressure sensor: The signal is almost static, the average of the measured pressure is equal to that of the actual pressure, but the pressure variation along the crank angle can not be described.
  - PSAUG1: static intake pressure signal
  - PAUSP1: static exhaust pressure signal
- High response pressure sensor: The signal is dynamic, the pressure variations along the crank angle can be described, but the average of the measured pressure has an offset with that of the actual pressure.
  - PSAUG_fast: dynamic intake pressure signal
  - PAUSP_fast: dynamic exhaust pressure signal

The Figure 3.2 shows the intake port pressures of case 004_PL_PFI_-0400, where the blue line (PSAUG_fast) is the dynamic intake pressure signal, while the red line (PSAUG1) is the static pressure intake signal. The black line is the intake port pressure that is obtained by moving the blue line, in which makes the average of blue line equal to the average of red line.

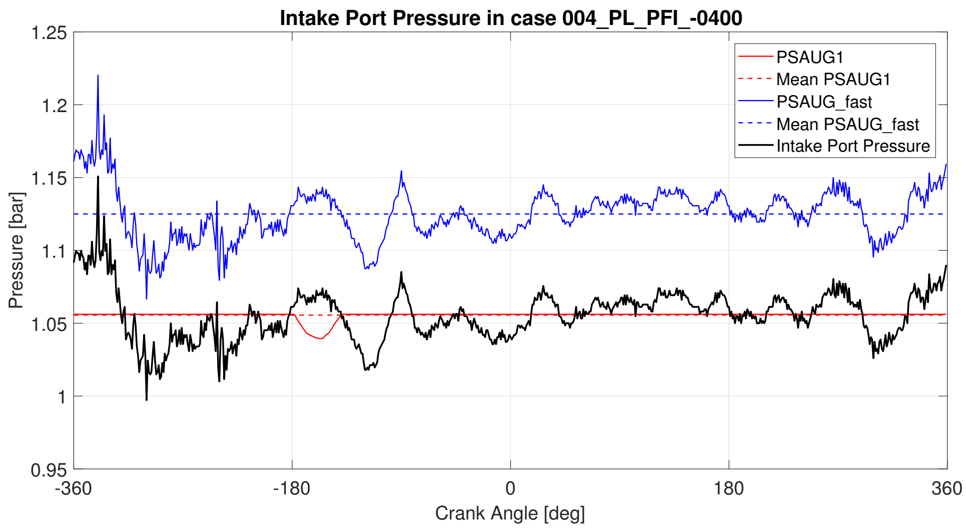

Figure 3.2: Intake port pressure in case 004_PL_PFI_0400

Therefore, the offset must be considered between these two pressure signals that are measured by the high/low response sensors.

$$
\begin{aligned}
OFFSET\_Int &= mean\left(PSAUG\_fast\right) - mean\left(PSAUG1\right) \\
&= \frac{\sum\left(PSAUG\_fast\right)}{720} - \frac{\sum\left(PSAUG1\right)}{720};
\end{aligned}
\tag{3.1}
$$

The relationship of the intake port pressure is as follows:

$$
P\_Int = PSAUG\_fast - OFFSET\_Int; \tag{3.2}
$$

With the same methodology, the exhaust pressure signals can be calculated, the Figure 3.3 shows the exhaust port pressures signals: PAUSP1, PAUSP_fast and Exhaust Port Pressure. The exhaust port pressure coincides with PAUSP_fast due to the average pressure signal of PAUSP1 is equal to the average pressure signal of PASUP_fast.

$$
P\_Exh = PAUSP\_fast - OFFSET\_Exh; \tag{3.3}
$$

Where the OFFSET_Exh is the gap between the mean value of PAUSP_fast and the mean value of PAUSP1, the relationship as follows:

$$
\begin{aligned}
OFFSET\_Exh &= mean\left(PASUP\_fast\right) - mean\left(PAUSP1\right) \\
&= \frac{\sum\left(PASUP\_fast\right)}{720} - \frac{\sum\left(PAUSP1\right)}{720};
\end{aligned}
\tag{3.4}
$$

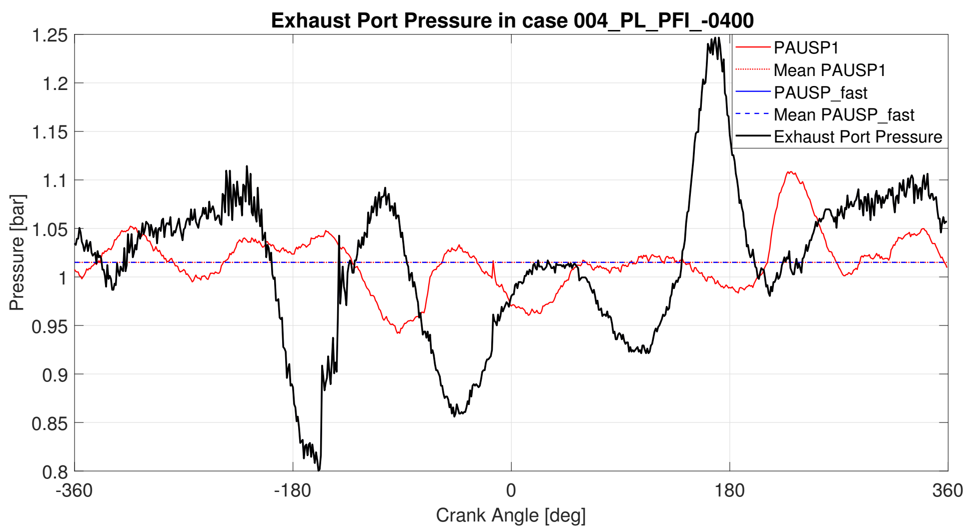

Figure 3.3: Exhaust port pressure in case 004_PL_PFI_0400

The 5 cycles of pressure signals are sampled for each test from the experimental data, in other words, in total there are 75 cycles (5×15) of pressure signals for each case.

The Figures 3.4 and 3.5 show the intake/exhaust presses signals in case 004_PL_PFI, in which the green lines are the average of intake/exhaust pressures, and they are the input data of the GT-Power simulation. In the figures, the lines of the pressures are concentrated, which means a small dispersion. The intake/exhaust port pressures in cases 005_PL_EOI250 and 006_PL_EOI100 can be found in the Appendix A. 1 (Intake/Exhaust Port Pressures).

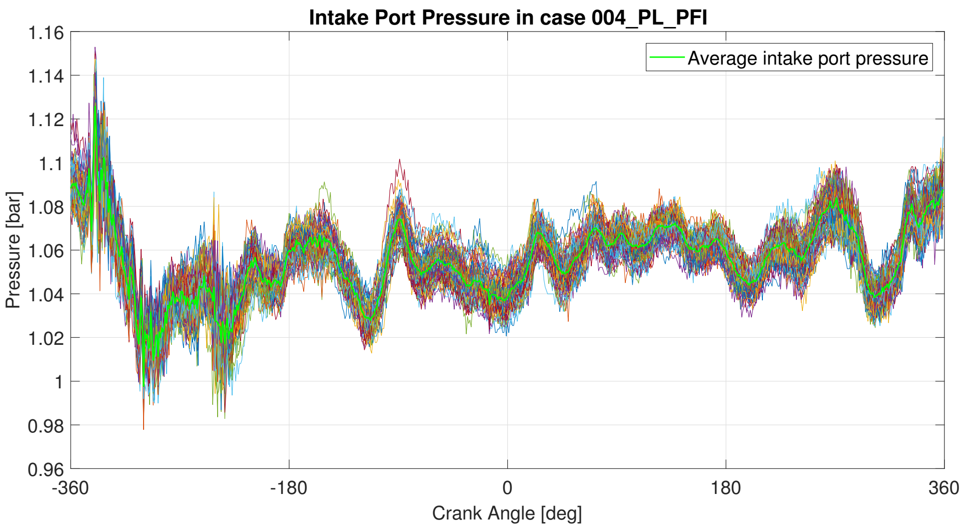

Figure 3.4: Intake port pressures in case 004_PL_PFI

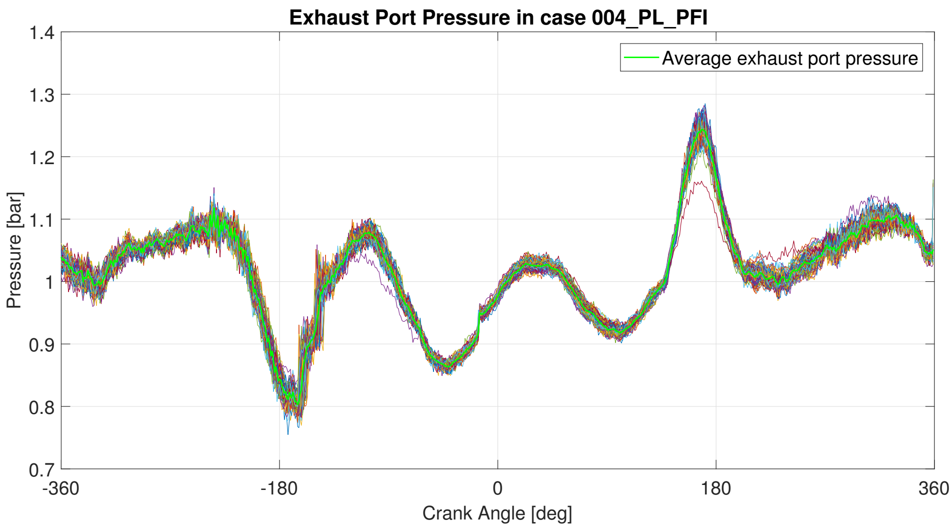

Figure 3.5: Exhaust port pressures in case 004_PL_PFI

3.2.3.2 Cylinder Pressure

The cylinder pressures are the main parameters in the GT-Power simulation with the TPA approach. Experimental data of the cylinder pressure are the crank angle-based signals, which are saved in the P_ZYL1. Because the sensitivity of the gaseous injection, the maximum cylinder pressure (PMAX1) varies between 26 bar and 18 bar, as shown in the Figure 3.6. The distribution of the maximum cylinder pressures has a high dispersion. Therefore, 10 cycles of cylinder pressure signals must be sampled for each test, which means 150 cycles (10×15 tests) of cylinder pressure signals for each case. The average pressure of these 150 cycles cylinder pressure signals is the input date of the GT-Power model. The Figure 3.7 shows the cylinder pressure trends in case 004_PL_PFI, the green line is the average cylinder pressure. The cylinder pressure trends in cases 005_PL_EOI250 and 006_PL_EOI100 are shown in the Appendix A.2 (Cylinder Pressures).

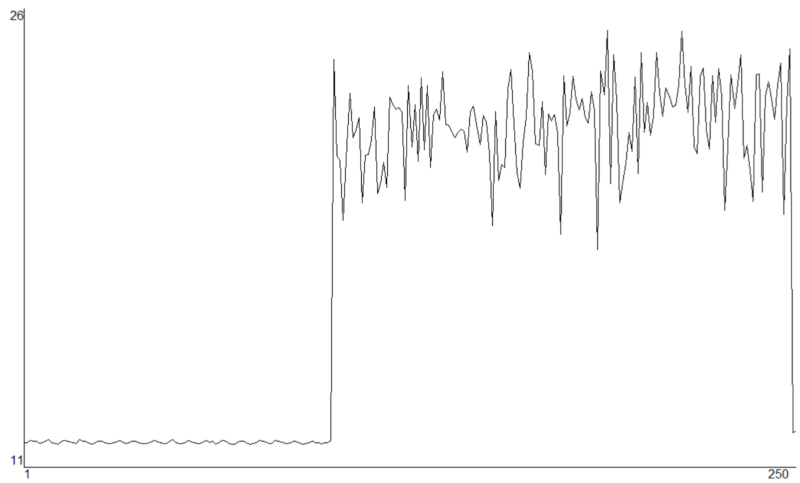

Figure 3.6: PMAX1 in case 004_PL_PFI_-0400

In addition, the Figure 3.8 shows the LogP-LogV diagram in the case 004_PL_PFI, calculating from the cylinder pressure and rank angle position. Because the top-land volume is larger due to the redesign of the piston, a part of the mixture is compressed into the top-land volume during the compression phase. This region has a high surface-to-volume ratio that prevents flame propagation. At the expansion phase, the mixture flows back from the top-land volume into the cylinder, and burns immediately. This causes a slow decline of cylinder pressure during the compression phase.

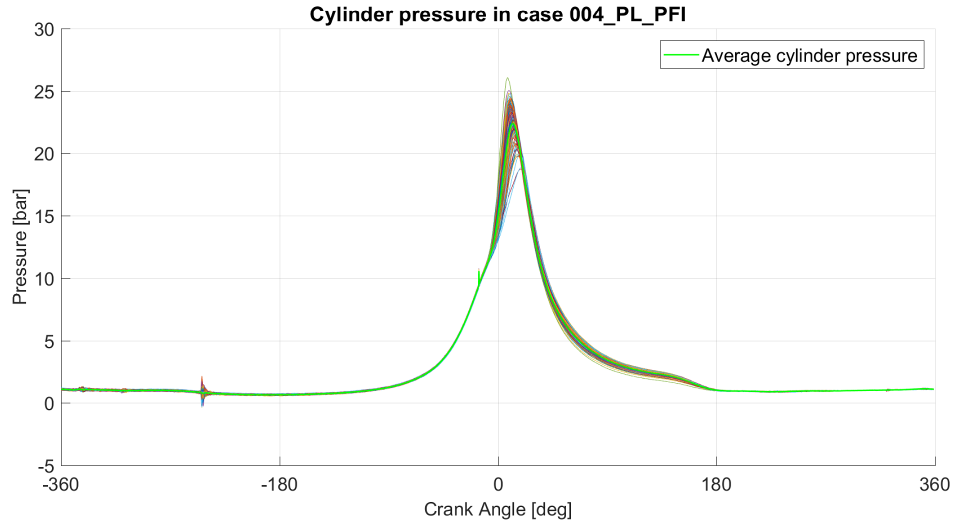

Figure 3.7: Cylinder pressure in case 004_PL_PFI

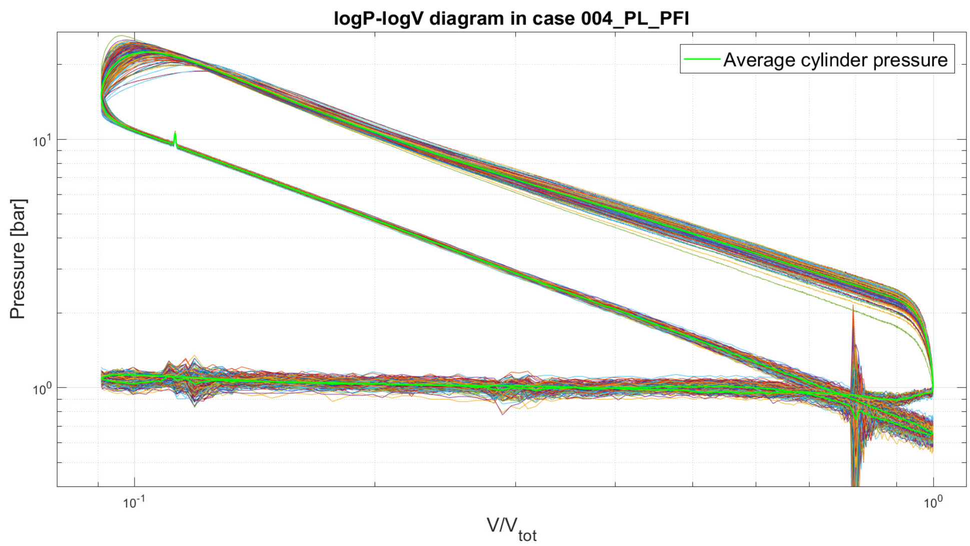

Figure 3.8: LogP-LogV diagram in case 004_PL_PFI

Because the Figure 3.6 shows a high dispersion of maximum cylinder pressure due to the sensitivity of the gaseous injection. Statistical analysis of the sample must be must be proceeded and compared with the population (total cylinder pressures) statistical data to determine the goodness of the sampling. The Tables 3.4 and 3.5 list the statistical results of maximum cylinder pressure and IMEP between sample and population. The statistical data (Standard deviation, mean and CoV) between sample and population are more or less equal, therefore, the sampling is valid.

Maximum Cylinder Pressure	Sample	Population
Standard Deviation [bar]	1.250717	1.371342
Mean [bar]	22.68612	22.56219
CoV	5.513%	6.078%

Table 3.4: The statistical data of P_MAX

IMEP	Sample	Population
Standard Deviation [kPa]	14.8546	15.8578
Mean [bar]	3.2205	3.2466
COV	4.613%	4.8996%

Table 3.5: The statistical data of P_MAX

3.2.4 Temperatures

The temperature signals are time-based signals, that means, the temperature trends vary with time. There are three temperatures to be sampled: Intake/Exhaust Port and Fuel temperatures. By case 004_PL_PFI, the valid time interval for temperatures (time-based signal) is between 9.3 s and 15 s.

With regard to the intake port temperature, the intake port temperature sensor was installed on the SCTE main intake port, 5 samples were randomly extracted from each test, in other words 75 (5×15) samples in total for each case. The average intake port temperature is 37.39 °C (310.54 K). All the temperatures extracted are shown in the Figure 3.9.
However, the methodology for obtaining intake port temperature is not suitable for exhaust port temperatures. Since the engine is cold at the beginning of the experimentation and the engine cylinder has no cooling system due to PLIF measurement, the exhaust port temperature increases continuously during experimentation, as the Figure 3.10. Therefore, the sampling methodology is not valid for the exhaust port temperatures. In the last laps of the experimentation, the engine tends to a stable state, therefore, the exhaust port temperature can be decided at 308.67 °C (581.82 K) per case 004_PL_PFI.

The fuel temperature is the natural gas temperature that is injecting into the combustion chamber. As the method of intake port temperature, 5 samples are extracted for each test of fuel temperatures. The average fuel temperature is 44.00 °C (317.15K). The Figure 3.11 shows all the fuel temperatures extracted from the experimental data and the average fuel temperature.

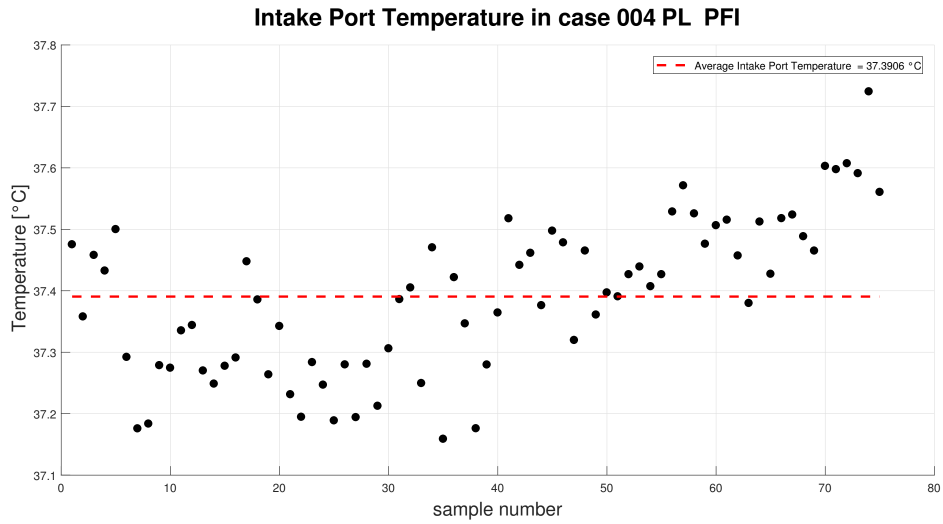

Figure 3.9: Intake port temperature in case 004_PL_PFI

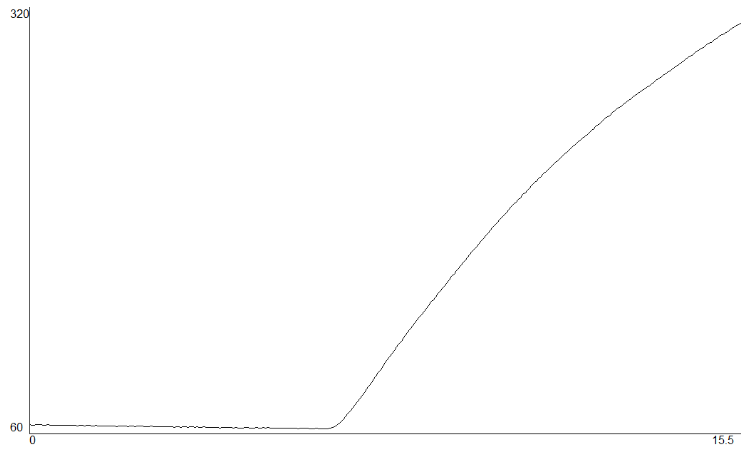

Figure 3.10: The trend of the exhaust port temperature in case 004_PL_PFI_-0400

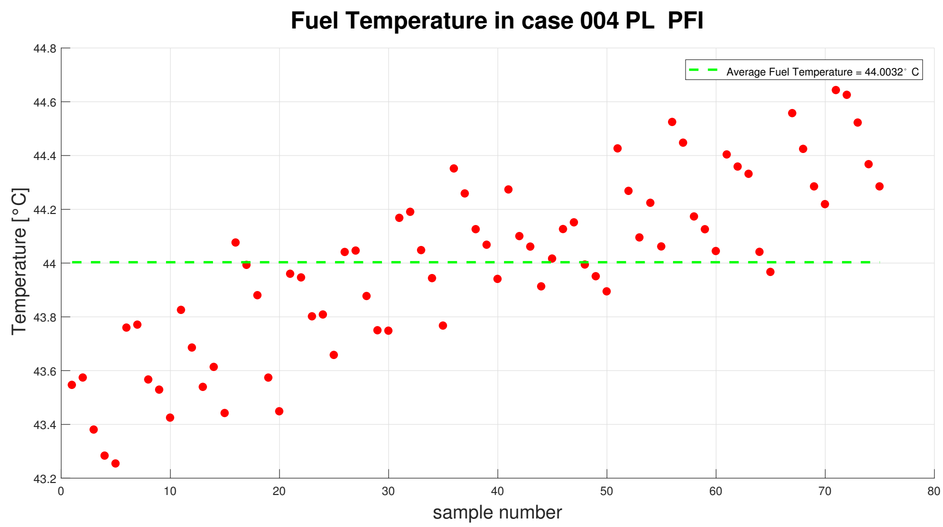

Figure 3.11: Fuel temperature in case 004_PL_PFI

The temperatures in cases 005_PL_EOI250 and 006_PL_EOI100 can be obtained by the same methodology, all the temperatures are listed in the Table 3.6.

Temperatures [°C]	004_PL_PFI	005_PL_EOI250	006_PL_EOI100
Intake Port Temp.	37.390	35.007	35.671
Exhaust Port Temp.	308.670	341.267	312.747
Fuel Temp.	44.003	40.327	44.003

Table 3.6: The temperatures in the three fired cases

3.2.5 Air flow rate

Air flow rates are the cycle-based signals, therefore, the air flow rate is not the instantaneous value that passed from the intake port, instead it is the average value on a cycle. The Figure 3.12 shows the air flow rate in case 004_PL_PFI_-0400 in the range of 250 cycles, the air flow rates range from 2 to 7 kg/h, with a high dispersion.

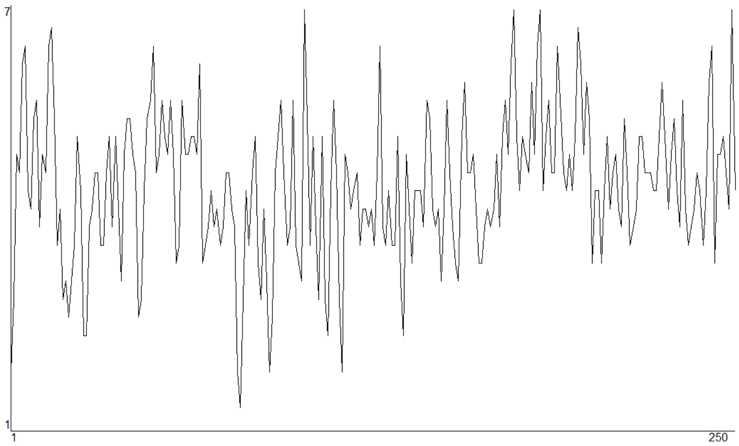

Figure 3.12: Air flow rate in case 004_PL_PFI_-0400

Because a high dispersion of air flow rate, 10 samples of air flow rate for each test are sampled, a total of 150 (10×15) air flow rates for each case. The Figure 3.13 shows all the air flow rates that are extracted from the experimental data. The average value of the air flow rate is 4.70 *kg/h* (= 1.31 *g/s* = 78.405 *mg/cycle*).

However, in cases 005_PL_EOI250 and 006_PL_EOI100, the measured values of the air flow rate are very small, the Figure 3.14 shows the air flow rate in case 005_PL_EOI250_-0600, the values do not change any more, this can decide the air flow sensor failure. Moreover, in case 004_PL_PFI, 4.70 *kg/h* of the air flow rate is a lower value by calculating the engine volumetric efficiency and indicated efficiency using this air flow rate.

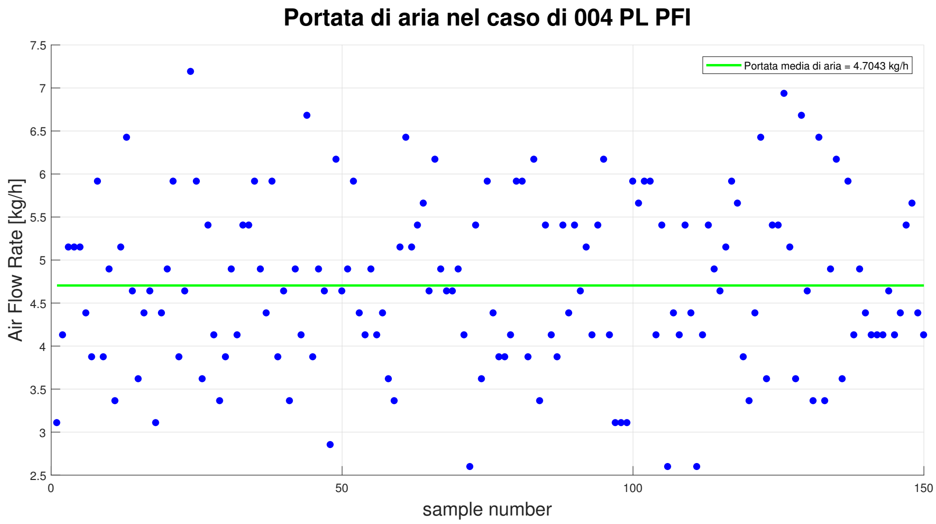

Figure 3.13: Air flow rate in case 004_PL_PFI

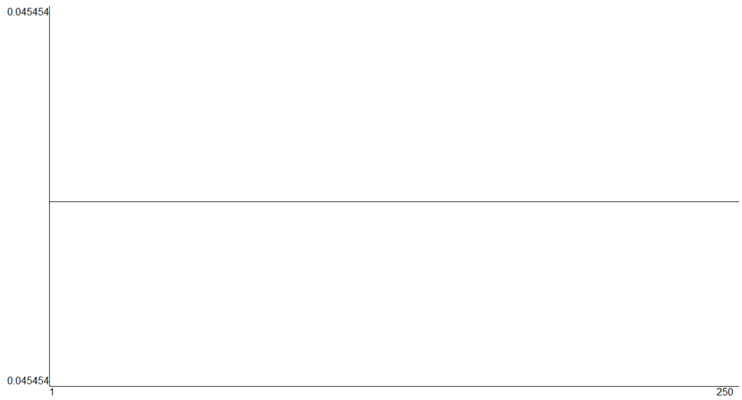

Figure 3.14: Air flow rate in case 005_PL_EOI_-0600

The engine displacement is:

$$V = \pi \cdot \frac{Bore^2}{4} \cdot Stroke = 346077.8mm^3; \tag{3.5}$$

From the intake port pressure (P_a=1.0556 bar) and temperature (T_a=310.54 K) in case 004_PL_PFI, the air density can be calculated as following:

$$\rho_a = \frac{P_a}{R \cdot T} = 1.184 \frac{kg}{mm^3} \tag{3.6}$$

Therefore, the engine volumetric efficiency and indicated efficiency can be calculated using the air flow rate m_a=4.70 kg/h in case 004_PL_PFI:

$$\lambda_V = \frac{\dot{m}_a}{\rho \cdot i \cdot V \cdot \frac{n}{m}} = 19.11\%; \tag{3.7}$$

$$\eta_u = \frac{IMEP \cdot \alpha}{\lambda_V \cdot \rho_a \cdot H_i} = 49.39\%; \tag{3.8}$$

From the point of view a conventional engine, 19.11% of the volumetric efficiency is a very low value in part load engine operation, moreover about 50% of the indicated efficiency for a natural gas engine is a high value, specifically in part load operation. In 2007, the Mercedes' Formula 1 engine breaks the 50% thermal efficiency barrier for the first time, which was realized under the condition in optimal engine working point and, on the dyno (dynamometer).

Therefore, the air flow rate must be obtained from the other method. In the experimental database, there is the duration of natural gas injection for each case. The air flow rate can be calculated from the injection duration.

	Pulse Width [us]					
Injected Quantity [mg] at	700	1000	2000	2500	5000	7000
Delphi DI-CNG 6 bar	1.3	2.2	4.8	6.2	12.6	17.6
Delphi DI-CNG 16 bar	4.0	6.8	13.9	17.7	35.1	48.7

Table 3.7: Injected quantity in 6 and 16 bar

The Table 3.7 lists the fuel mass injected in cycle with pulse width of Delphi DING injector, this injector is the same one with experimentation. In the table there are the quantities of natural gas injection at 6 bar and 16 bar with a series of duration of injection. Because the injection quantity is linear with both the duration of injection and the injection pressure, the quantity of natural gas injected at a certain duration of injection in 8 bar can be calculated using the interpolation. The Figure 3.15 shows the process of obtaining air flow rate from injection duration and Delphi injection data. In fired condition, lambda (λ) is equal to 1, that means, air-fuel ratio is 17.2. The air flow rates can be calculated by fuel flow.

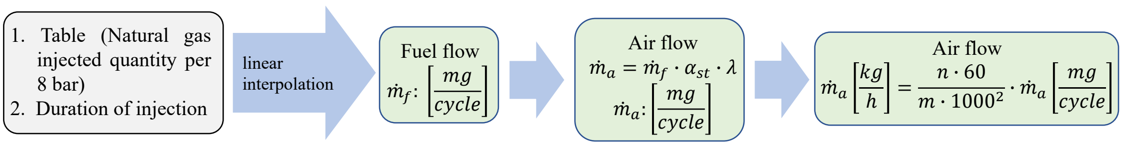

Figure 3.15: the process from duration of injection and Delphi injection data to the air flow

The Figure 3.16 shows the quantities of injection in three cases in different duration of injection by calculating in interpolation. The difference between the three cases is the injection strategy. In the case 004_PL_PFI, the injection is early at the beginning of intake stroke, natural gas takes up a part of the combustion chamber volume, results in a lower quantity of trapped air. Thus, the case 004_PL_PFI has the lowest injected quantity of natural gas in these three cases. Instead, in the case 006_PL_EOI100, the late injection offers higher quantity of trapped air in the combustion chamber, thus, higher injected quantity of gas natural.

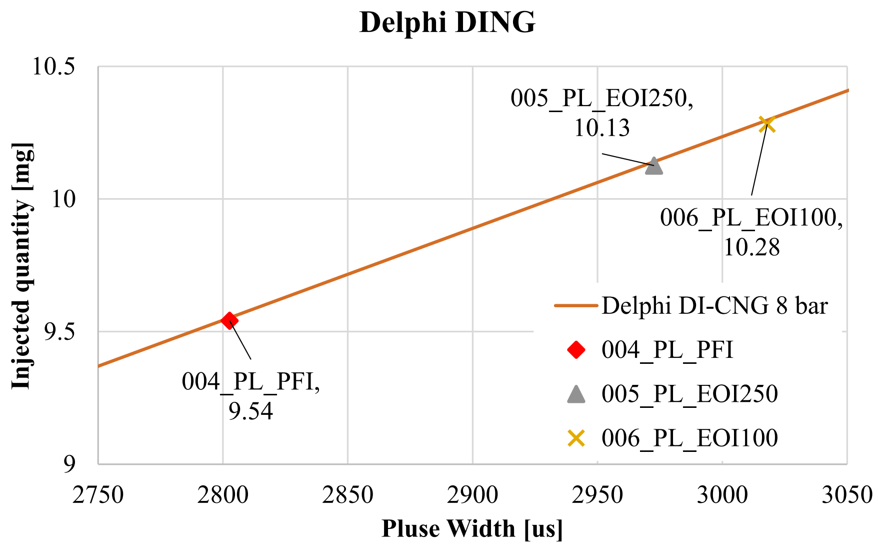

Figure 3.16: Injected quantity in the fired cases 004_PL_PFI, 005_PL_EOI250 and 006_PL_EOI100

Finally, air flow rate can be calculated by this method, the Table 3.8 lists the results of air flow rate in three different cases.

Case	DOI		$\dot{m}_f$	$\dot{m}_a$	
	[ms]	[us]	[mg/cycle]	[mg/cycle]	[kg/h]
004_PL_PFI	2.80	2803	9.54	164.11	9.846
005_PL_EOI250	2.97	2973	10.13	174.17	10.450
006_PL_EOI100	3.02	3018	10.28	176.85	10.611

Table 3.8: The results of air flow rate

In addition, air flow rates must be verified to determine if they are reasonable by comparing the volumetric efficiency and indicated efficiency with those of a conventional engine. The Table 3.9 lists the results of volumetric efficiency and indicated efficiency by calculating from the experimental data and air flow rates. 40% of the volumetric efficiency and 24% of indicated efficiency are the regional values for an engine in part load operation.

Case	T_Int [K]	P_Int [bar]	$\dot{m}_a$ [kg/h]	Density [kg/m^3]	IMEP [bar]	Volumetric efficiency	Indicated efficiency
004_PL_PFI	310.54	1.0556	9.85	1.18	3.25	40.32%	23.57%
005_PL_EOI250	308.16	1.0554	10.45	1.19	3.58	42.47%	24.49%
006_PL_EOI100	308.82	1.0551	10.61	1.18	3.50	43.44%	23.55%

Table 3.9: The results of engine volumetric efficiency and indicated efficiency

3.2.6 Input experimental data

After sample extraction from experimental data, all useful data for GT-Power simulation are obtained. The input data contain intake/exhaust port pressures and temperatures, cylinder pressures, fuel temperatures and air flow rates for 3 cases in fired condition and 7 cases in motored condition (because there are no duration of injection and spark ignition in motored condition, there are no fuel temperatures and air flow rates for input data).

The Figures 3.17, 3.18 and 3.19 show the intake/exhaust port and cylinder pressure profiles in cases 004_PL_PFI, 005_PL_EOI250 and 006_PL_EOI100. And the Table 3.10 lists the other input data, such as, intake/exhaust port temperatures, air flow rate, spark timing and IMEP in three cases. In the Appendix A.3 is shown the input data in motored condition, such as, intake/exhaust port and cylinder pressures, intake/exhaust port temperatures, and lambda (lambda are the unknown data, which are described in the Section 4.2: Equivalence ratio in motored condition).

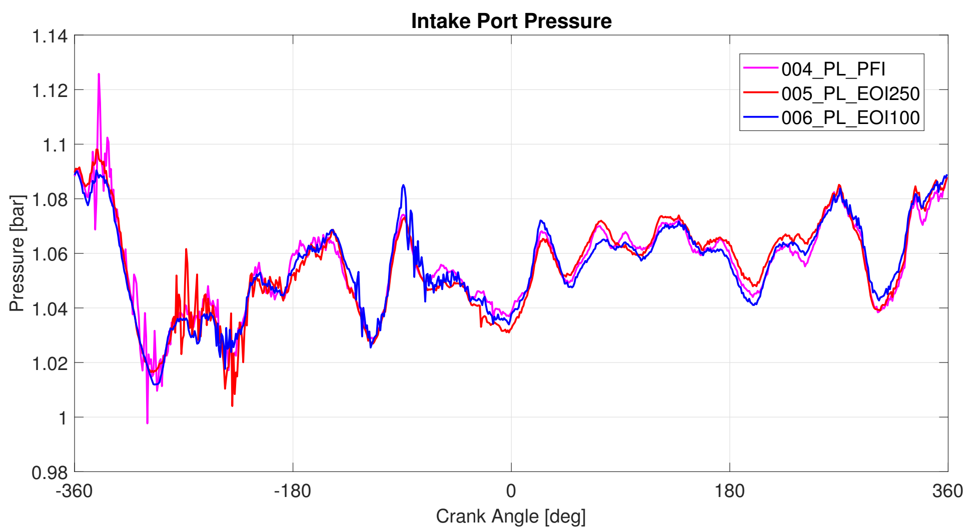

Figure 3.17: Intake port pressure profiles in fired condition

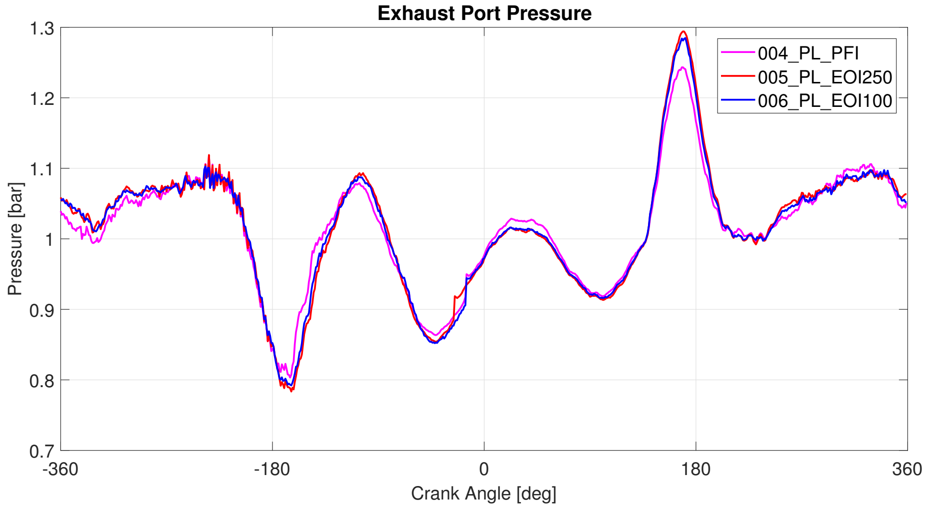

Figure 3.18: Exhaust port pressure profiles in fired condition

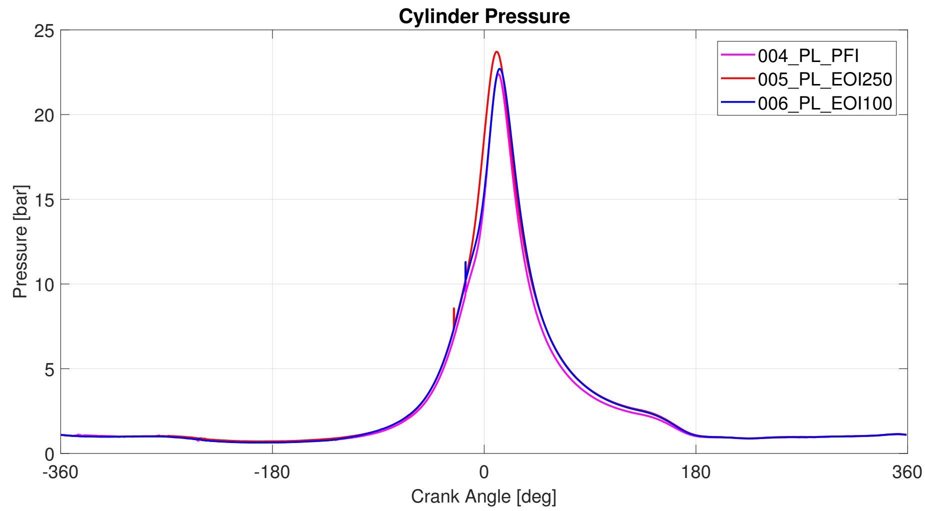

Figure 3.19: Cylinder pressure profiles in fired condition

Parameter\Cases	004_PL_PFI	005_PL_EOI250	006_PL_EOI100
Intake Port Temp. [°C]	37.390	35.007	35.671
Exhaust Port Temp. [°C]	308.670	341.267	312.747
Fuel Temp. [°C]	44.003	40.327	44.003
Air Floe Rate [kg/h]	9.846	10.450	10.611
Spark Timing [CA BTDC]	16	26	16
IMEP [bar]	3.249	3.583	3.499

Table 3.10: Temperatures, air flow rate, spark timing and IMEP in fired condition

3.2.7 Problem of exhaust port and cylinder pressures

There is a problem for exhaust and cylinder pressures for each case. The Figure 3.20 shows this problem in the case 004_PL_PFI, that the exhaust pressure is higher than the cylinder pressure in the exhaust stroke (CA = 180 $\sim$ 360 deg). It is not possible to guarantee the expulsion of exhaust gases from the cylinder during the exhaust stroke, due to the cylinder pressure being lower than the exhaust pressure.

However, it can not determine this is caused by an underestimation of the cylinder pressure or an overestimation of the exhaust pressure measured by the sensors. In the next steps, the input data for these two pressures are still experimental pressures.

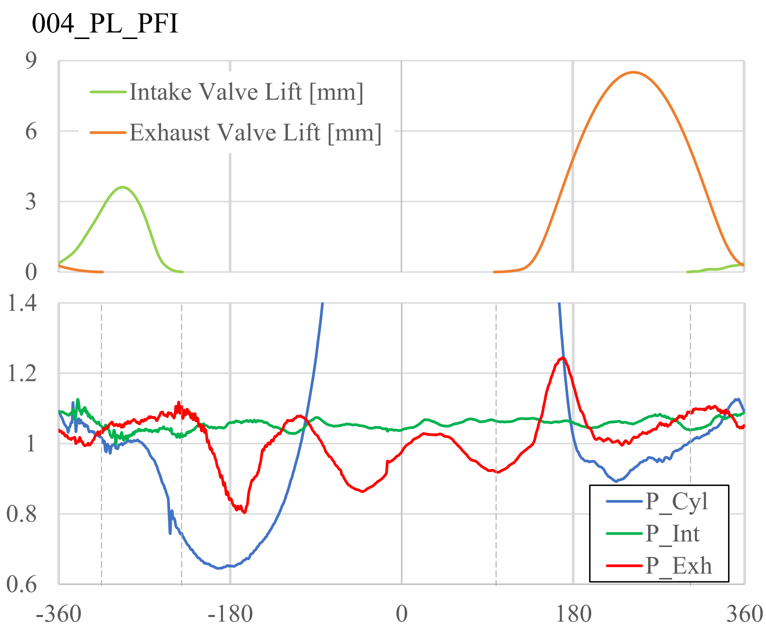

Figure 3.20: Problem of exhaust and cylinder pressure in case 004_PL_PFI

3.3 SCE Model setup for TPA

The starting point of the single-cylinder engine (SCE) model is an already existing engine model, which is the Three-cylinder engine (base engine of the project) model and the figure shows in the Appendix B.1. The purpose is to get a single-cylinder direct injection engine from the multi-cylinder engine (3-cylinder engine) model. In the Table 1.2, the main changes of the single-cylinder engine are compression ratio and stroke. The compression ratio of 3-cylinder base engine is 13, instead that of SCE is 11. The stroke of the SCE is 85 mm.

3.3.1 Intake/Exhaust port layout

The main change of the single-cylinder engine is intake/exhaust layout. The SCE is a prototype specifically dedicated to CNG, Therefore, intake/exhaust layout is not complex compared to the base engine, there are no turbocharger and throttle systems. The Figure 3.21 shows the intake/exhaust layout of the single-cylinder engine CAD model, the left side is the intake port, while the right side is the exhaust port. The small holes on the main intake port are the points for installing temperature and pressure sensors. The four holes that are on the branch ports and at the top of the cylinder are the points for installing and guiding the intake/exhaust valves.

The geometrical parameters of intake/exhaust ports are in the Appendix B.2 and B.3. The intake port is longer and slightly curved, intake port is divided into four parts. The first part is the main port from the entry to bifurcation points, the second and third parts are branch ports, and the last part is the pipe to which the air entering the cylinder. While, for the exhaust port, two parts are sufficient.

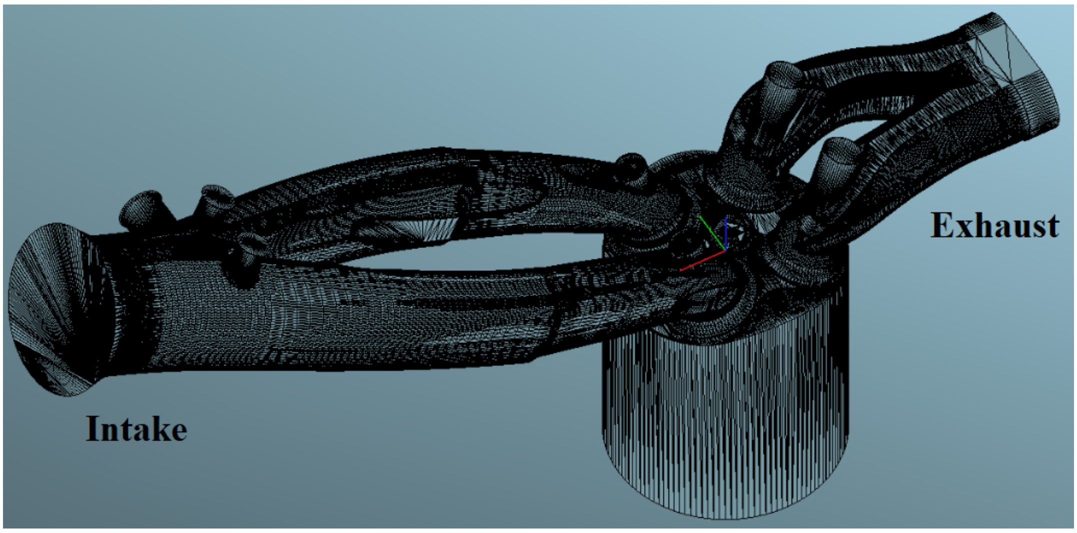

Figure 3.21: Intake/exhaust layout of single-cylinder engine CAD model

3.3.2 Injector

In the fired condition, the engine always operates in the stochiometric condition, the relative air/fuel ratio is 1. Because engine temperatures and intake/exhaust port temperatures are unknow values, therefore, if the fuel flow as input data there is a difficulty in calibrating unknow temperatures.

By inserting a controller, it can detect the simulated air flow rate during GT-Power simulation, the simulated fuel flow can be obtained from the air/fuel ratio. Because the simulated air flow varies with intake port and engine temperatures and other engine parameters, therefore, the amount of natural gas injected is a value that varies with the temperatures to be calibrated. The Figure 3.22 shows the injector system layout. The advantage of this methodology is that the experimental air flow rate (input data) is a reference value to calibrate the temperatures and other engine parameters by comparing the experimental air flow rate with the simulated air flow rate.

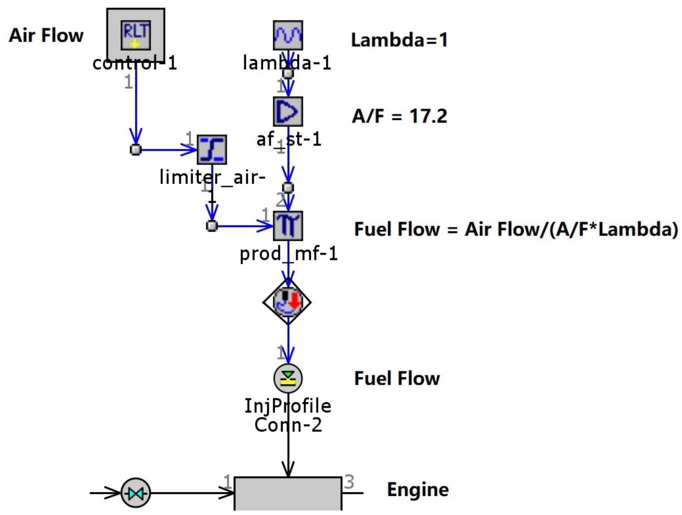

Figure 3.22: The injector system layout

3.3.3 SCE model

The Figure 3.23 is the SCE model for TPA simulation. In addition to the intake/exhaust layout, the injector system, the cylinder and engine crank train, the most important part for TPA model is the intake/exhaust boundary conditions. The purpose of the template 'EndEnvironmentTPA' is imposing the measured port pressure and temperature as the boundary conditions. The template 'Intake-01' in the Figure 3.23 is the intake boundary condition, while the template 'Exhaust-01' is exhaust boundary condition. The intake/exhaust port temperatures and pressures obtained in the Section 3.2 are imposed separately into the 'Intake-01' and 'Exhaust-01' templates.

Furthermore, the single-cylinder engine works in part load operations during experimentation. Thus, intake valve lift profile must be modified according to valve lift profile as described in the Section 2.1 in Figure 2.4, the Figure 3.24 shows the setting interface of the intake valve template, the intake valve lift profile is an array about the crank angle.

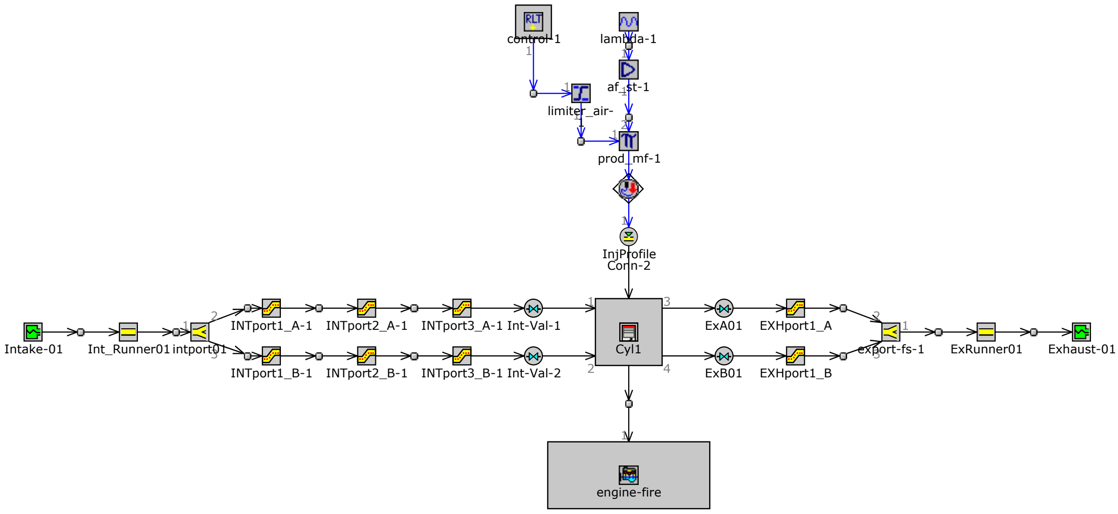

Figure 3.23: SCE model for TPA simulation

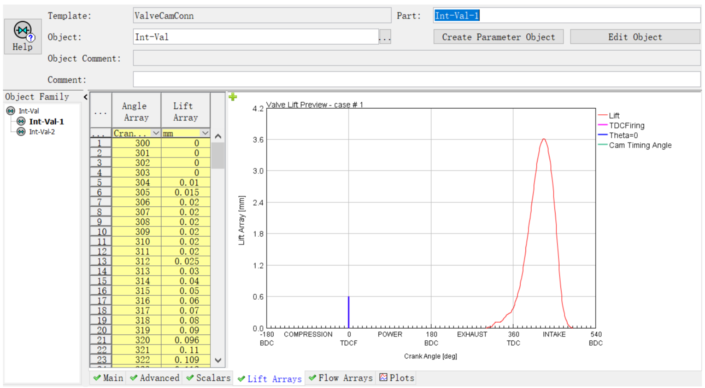

Figure 3.24: Intake valve template setting interface

3.4 SCE TPA model calibration

After completing the SCE model for TPA simulation, the next step is to run the model and compare the simulated results with the experimental o measured ones. Because some engine parameters are unknow, such as, intake/exhaust port heat transfers, engine cylinder wall temperatures and valve events etc. Therefore, the calibration is an indispensable step, the purpose of calibration is to match the simulated results with the experimental ones, for example, air flow rate, IMEP, engine cylinder pressure profile.

3.4.1 The simulation results with the default parameters

The Table 3.11 lists the default parameters of SCE model for TPA simulation, all these parameters consult from the Engine Performance Application Manual of GT-SUITE. Moreover, the valve events (timing and lash) has the influence at air flow rate, because it could have the problems of precision during the installation of the engine components, these two parameters are adjusted from 0.

Baseline		
EngCylTWall [K]		
T_Head	Head Temperature	350
T_Piston	Piston Temeprature	350
T_Cylinder	Cylinder Temperature	300
Intake Port Head Transfer		
HTM	Heat Transfer Multiplier	1.5
T_Wall_Int [K]	Imposed Wall Angle	440
Valve Events		
Timing_Val_Int [deg CA]	Cam Timing Angle	0
Lash_Val_Int [mm]	Intake Valvle Lash	0

Table 3.11: The default engine parameters

The GT-Post provide some input data consistency checks, the L.H.V multiplier provides an indication of the cumulative error of input data in the TPA simulation. The results of this cumulative error are the total of the fuel supply. The purpose of calibration is that the L.H.V multiplier varies lower than 5% (varies between 0.95 and 1.05) and the simulated cylinder pressure match the experimental one, specifically during compression stroke.

The calibration is performed by the 004_PL_PFI case, if the parameters are suitable for the 004_PL_PFI case, it can be suitable for other cases. After setting the parameters in the SCE model and run the results. The Figure 3.25 shows the simulation table results for the first run. In the tables there are simulated IMEP, maximum cylinder pressure, air flow rate, fuel flow rate and L.H.V.

In the table Comparison to Test Data, "Consistency Check" is E21.22, which means that the error in the air flow rate and fuel flow rate. The simulated air flow rate is 177.38 mg/cycle (10.65 kg/h), while the experimental one is 164.11 mg/cycle (9.85 kg/h). The difference between the simulated air flow rate and the experimental one is about 8%, which is higher than the requirement indicated in the Engine Performance Application Manual of GT-SUITE: If the two values differ by more than 5%, it is flagged as an error [18]. In the table Energy Fuel and Adjustment, the

Comparison to Test Data

	Cyl1
Object Name	Cyl1
Consistency Check	E,21,22
Air Flow [mg/cycle]	177.38
Air Flow - Test Data [mg/cycle]	164.11
Fuel Flow [mg/cycle]	10.313
Fuel Flow - Test Data [mg/cycle]	9.541
Fuel/Air Ratio	0.0581
Fuel/Air Ratio - Test Data	0.0581
Combustion Efficiency	0.998
Combustion Efficiency - Test Data	1.000
Burned Fuel Fraction	0.998
Burned Fuel Fraction - Test Data	1.000

Fuel Energy and Adjustments

	Cyl1
Object Name	Cyl1
Consistency Check	E,12
Fuel Energy (LHV) Mult. (1)	0.734
Energy Balance Ratio (2)	0.725
Fuel Energy Entering Cylinder [J]	515.64
Fuel Power Entering Cylinder [kW]	8.59
Indicated Cylinder Power [kW]	1.858
Apparent Indicated Efficiency [%]	21.62
Heat Transfer During Analysis [%]	14.93
Fraction of Fuel Injected Late (3)	0.0000

Engine Performance Predictions (SI)

	Performance
Brake Power [kW]	2.1
Brake Power [HP]	2.8
Brake Torque [N-m]	10.0
IMEP [bar]	4.62
FMEP [bar]	0.97
PMEP [bar]	-0.20
Air Flow Rate [kg/h]	10.6
BSAC [g/kW-h]	5064
Fuel Flow Rate [kg/h]	0.6
BSFC [g/kW-h]	294.4
Volumetric Efficiency [%]	43.4
Volumetric Efficiency (M) [%]	43.4
Trapping Ratio	0.999
A/F Ratio	17.20
Brake Efficiency [%]	24.5

Figure 3.25: The simulation table results with the default parameters

fuel energy (L.H.V) multiplier is 0.734, which is very lower, due to the simulated fuel flow is greater than the experimental one, the L.H.V multiplier is lower than 1 in order to match the experimental cylinder pressure profile in the combustion stroke. This can be explained in the Figure 3.26, during the first part of compression stroke, the simulated pressure can match the experimental one. But at first of ignition, the simulated pressure can not match the experimental one, the simulated pressure has a higher slope than the experimental one.

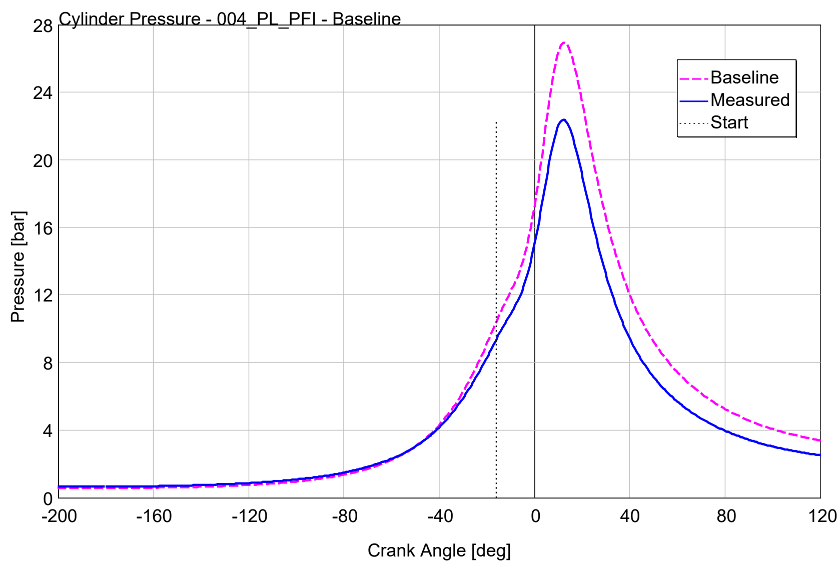

Figure 3.26: The simulated pressures with the default parameters

There are two points to cause these problems: one is the higher air flow rate, another is the lower engine thermal heat transfer.

3.4.2 Calibrating the air flow rate

The air flow rate, and thus the volumetric efficiency, is the most important parameter that influences engine performance when the air fuel ratio is fixed. Influence performance is engine output, such as, IMEP, cylinder pressure profile and brake torque. From the previous results, the simulated air flow rate is high than the experimental one, and the two values differ by about 8%. The purpose of calibrating the air flow rate is to decrease the simulated air flow rate with the difference less than 5%.

The main factors influencing the air flow rate are the intake and exhaust valves, the intake ports and intake wall temperatures and heat transfer in the intake ports. Because Intake ports wall temperature is 440K, that is a high default value. Therefore, there are two important factors to analyze the air flow rate influences, one is heat transfer in intake ports, and the other is valve events, which is the intake valve lash, because intake/exhaust valve timing is the known condition, which is described in the Section 2.1.

The heating of air by intake ports which is entering the cylinder has a significant effect on air flow rate. The density of the heated air will be reduced and lower amounts of trapped air mass during the intake stroke. The effect of heat transfer multiplier (HTM) is that increases the additional turbulence in the intake ports, more heat transfers from intake ports to the air, especially at lower engine speed. The Table 3.12 is a test of the effect of heat transfer multiplier on the air flow rate in the SCE model. The HTM varies between 1 and 2.5, the air flow rate reduces as the heat transfer multiplier increases. This is a test to know the degree of reduction of the air flow rate when increasing the HTM, because the HTM greater than 2 is not a conventional value.

Cases	Case 1	Case 2/Baseline	Case 3	Case 4
HTM	1	1.5	2	2.5
Air Flow [kg/h]	11.006	10.645	10.395	10.224
Difference	11.78%	8.11%	5.88%	3.84%

Table 3.12: The effect of heat transfer multiplier on the air flow rate

In terms of valve events, the valve timing is a known condition that is described in the Section 2.1, therefore, the valve lash is a parameter to be calibrated.

Valve lash is the mechanical clearance or gap between the valve stem tip and the tip of the rocker arm (o the cam). The Figure 3.27-a shows the valve lash in overhead camshaft (OHC) valvetrain direct-acting system. If valve lash is zero in the cold state of the engine, after the engine is running, the thermal expansion of the valve and other parts of the valvetrain will result in incomplete closing of the intake/exhaust valves (valve lash ¡ 0), which lead to the mixture escape from the cylinder during compression and combustion strokes. Therefore, usually the valve lash is greater than 0. But if there is too much valve lash it will decrease the duration of lift, lead to excessive wear on valvetrain, and cause noise in the engine. Consequently, typical valve lash is in the range of 0.0 to 0.9 mm for the mechanical valvetrain.

In the experimentation, the SCE engine does not equip the direct-acting valvetrain system, instead it is the end pivot rocker valvetrain system, as the Figure 3.27-b. The lash adjuster has the function to eliminate the valve lash caused by the thermal expansion for any engine conditions which is realized by the oil pressure in the lash adjuster. Actually, oil does leak when the lash adjuster valve is open, and the oil is not incompressible. For these reasons, the lash adjuster is assumed to have 0.2 mm of effective lash [19].

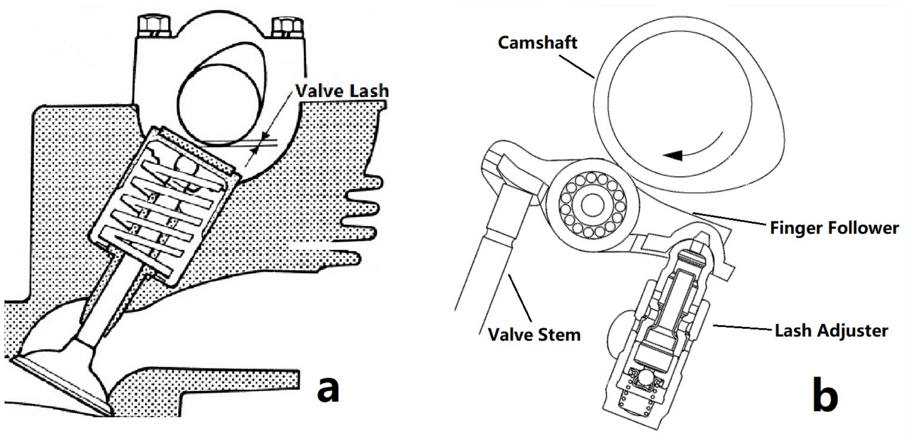

Figure 3.27: Overhead camshaft valvetrain configuration (a: direct-acting; b: end pivot rocker)

According to the description of the principle and function of the valve lash, the Table 3.13 is a test of the effect of the intake valve lash on the air flow rate in the SCE model. The intake valve lash varies between 0 and 2.4 mm, because the principle of lash adjuster is hydraulic control.

The experimental results agree with the theoretical analyzes, as the valve lash increases, the air flow rate decreases. Because the intake valve lash eliminates the more ”gentle” sections (two extremes of the valve lift profile) of the intake valve lift, and lowers the intake valve lift, which causes a lower amount of air flow through the intake valves.

By combining the effects of the heat transfer multiplier of intake port and the intake

Cases	Case 1/Baseline	Case 2	Case 3	Case 4
Lash_Val_Int [mm]	0	0.08	0.16	0.24
Air Flow [kg/h]	10.645	10.550	10.348	10.125
Difference	8.11%	7.15%	5.09%	2.83%

Table 3.13: The effect of intake valve lash on the air flow rate

valve lash, in the Modified case, the heat transfer multiplier is 1.8 (1.5 in the Baseline case), and the intake valve lash is 0.2 mm (0 in the Baseline case). The Table 3.14 lists the engine parameters in the Baseline, Modified and Modifired_1 case, the Modified_1 case will be analyzed in the next subsection to calibrate the cylinder pressure. The results of these three cases (Baseline, Modified and Modified_1) are shown in the Appendix B.4. The simulated air flow rate in the Modified case is 10.076 kg/h, has a difference of 2.34% with the experimental one. This air flow rate is an acceptable value. Therefore, the engine parameters in Modified case are valid and reasonable to calibrate the air flow rate.

3.4.3 Calibrating the cylinder pressure

After calibrating the engine parameters for air flow rate, in the Engine Performance Prediction (SI) table of the Modified case results, the simulated engine IMEP is equal to 4.35 bar, which is a greater value than the experimental one (experimental engine IMEP = 3.25 bar). Moreover, from the point of view of the engine cylinder pressure trace, the simulated cylinder pressure of the Modified case is higher than the experimental one in the combustion o power stroke. Therefore, the engine heat transfer in the cylinder is lower for SCE model.

The heat transfer in the cylinder is most significant during the power stroke, and has a greater effect on the predicted (or simulated) IMEP. A greater heat transfer can lower the cylinder pressure trace during the power (combustion) stroke, and lower the predicted engine IMEP. The convection multiplier is a parameter to calibrate heat transfer in the cylinder. For the conventional engine, the value of convection multiplier is in the range of 0.85-1.6.

However, the SCE is not a conventional engine, where the cylinder is made of glass, the piston has been designed by PLIF measurement, which is not a conventional piston. In the cylinder pressure calibration process, the value of convection multiplier varies between 1 and 4. When the convection multiplier is equal to 3.4, the predicted engine IMEP is 3.35 bar, and have an 3.1% difference with the experimental one, this is an acceptable value. The Table 3.14 lists the parameters during air flow rate and cylinder pressure calibration, and the results of tables and cylinder pressure plots are shown in the Appendix B.4.

Parameter\Cases	Baseline	Modified	Modified_1
EngCylTWall [K]			
T_Head	350	350	350
T_Piston	350	350	350
T_Cylinder	300	300	300
Intake Port Head Transfer			
HTM	1.5	1.8	1.8
T_Wall_Int [K]	440	440	440
Valve Events	0	0	
Timing_Val_Int [deg CA]	0	0	0
Lash_Val_Int [mm]	0	0.2	0.2
Convection Multiplier	1	1	3.4

Table 3.14: The engine parameters during calibration

In the results of tables, the "Consistency Check" is OK in the Modified_1 case for both air/fuel flow rate and L.H.V multiplier. In addition, the IMEP of Modified_1 case is close to the experimental value. For the engine cylinder pressure profile and LogP-LogV diagram, the simulated cylinder pressure of Modified_1 case matches the experimental one very well, specifically during the combustion stroke.

Because the piston and cylinder are designed for PLIF measurement, the volume between cylinder glass liner and piston is greater than the real engine. This compromise has a negligible impact on the mixture formation process, but it has a significant influence for the power stroke. The Figure 3.28 shows the burn rate and burn fuel fraction in case 004_PL_PFI, the combustion process of the mixture is composed of two sections. The first section is between the start of combustion (CA -16 deg) and the crank angle at about 25 deg, this section of combustion process is similar to the Wiebe function, which is the combustion of the mixture in the combustion chamber. The second section is between the CA 25 deg and CA 120 deg, which is a slow combustion process, due to the mixture flows back from the volume between piston and cylinder. This part of the mixture is compressed in the volume between the piston and cylinder during the compression stroke due to the increase of the cylinder pressure, when the cylinder pressure drops during expansion (o power) stroke, this part of mixture flows back from the volume into the cylinder and burn with a slow speed due to lower temperature and pressure.

This phenomenon explained the engine cylinder temperature has a section of the constant temperature in the power stroke after the maximum temperature in fired condition.

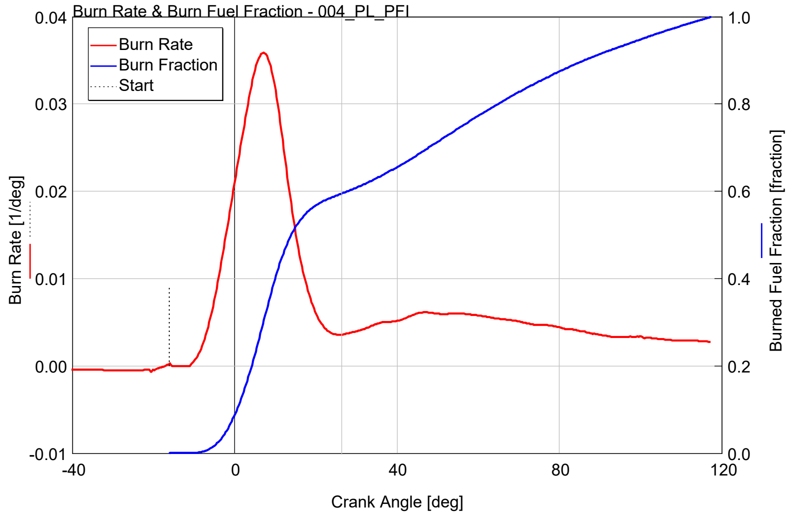

Figure 3.28: Burn Rate and Burn Fuel Fraction in case 004_PL_PFI

For some reason:

- The SCTE is not a conventional engine, including cylinder (glass liner) and piston;
- The compression ratio is an approximate value (CR $\sim$ 11);
- There are problems between cylinder pressure and exhaust pressure.

The parameters of Modified_1 case are the final calibrated engine parameters, although there are still small differences between the experimental and simulated results, but the differences are acceptable.

3.5 TPA Results for SCTE model

After determining the engine parameters, the next step is to check the validity of the engine parameters of Modified_1 case for the other two cases, 005_PL_EOI250 and 006_PL_EOI100.

The numerical or tables results shown in the Appendix B.5, and the results of the cylinder pressure profiles shown in the Appendix B.6. The "Consistency Check" is OK for both air flow rate and L.H.V multiplier, in addition, the simulated cylinder pressures of Modified_1 case match the experimental ones very well for all three cases. Since the engine parameters of Modified_1 can satisfy the three cases in fired condition at the same time, the engine parameters of Modified_1 are the engine parameters during experimentation.

The Table 3.15 has listed the differences between the simulated results and experimental ones in the three cases, these results are the air flow rate, engine IMEP and L.H.V multiplier. The differences in the air flow rate and IMEP of case 004_PL_PFI is the greatest and L.H.V multiplier is 0.966. Therefore, the case 004_PL_PFI is the worst case in these three cases.

Difference	004_PL_PFI	005_PL_EOI250	006_PL_EOI100
Air Flow Rate	2.29%	1.26%	0.40%
IMEP	3.08%	-2.23%	2.57%
L.H.V Multiplier	0.966	0.993	0.984

Table 3.15: The differences between simulated and experimental results

The purpose of numerical simulation of SCE is to obtain the engine cylinder pressures and temperatures in the fired and motored conditions. The Figure 3.28 shows the engine cylinder temperatures and burn fuel fraction in case 004_PL_PFI, 005_PL_EOI250 and 006_PL_EOI100. The Subsection 3.4.3 explained the burn fuel fraction and engine cylinder temperature during the power stroke.

Since the mixture formation is in the last part of intake stroke and all part of compression stroke, therefore, the engine cylinder pressures and temperatures in this section are the most interesting for PLIF calibration analysis. The Figures 3.30 and 3.31 show the engine cylinder pressures and temperatures in the section of intake and compression strokes in the fired and motored conditions. The cylinder pressures of fired condition and those of motored condition have the difference about 0.4 bar due to the type of injection is port fuel injection (PFI) in motored condition, a part of natural gas occupies the intake air volume, which causes a decrease of the intake port pressure. In addition, the engine temperature is lower than that in the motored condition, the cylinder temperature is lower than those in fired condition during intake and compression strokes.

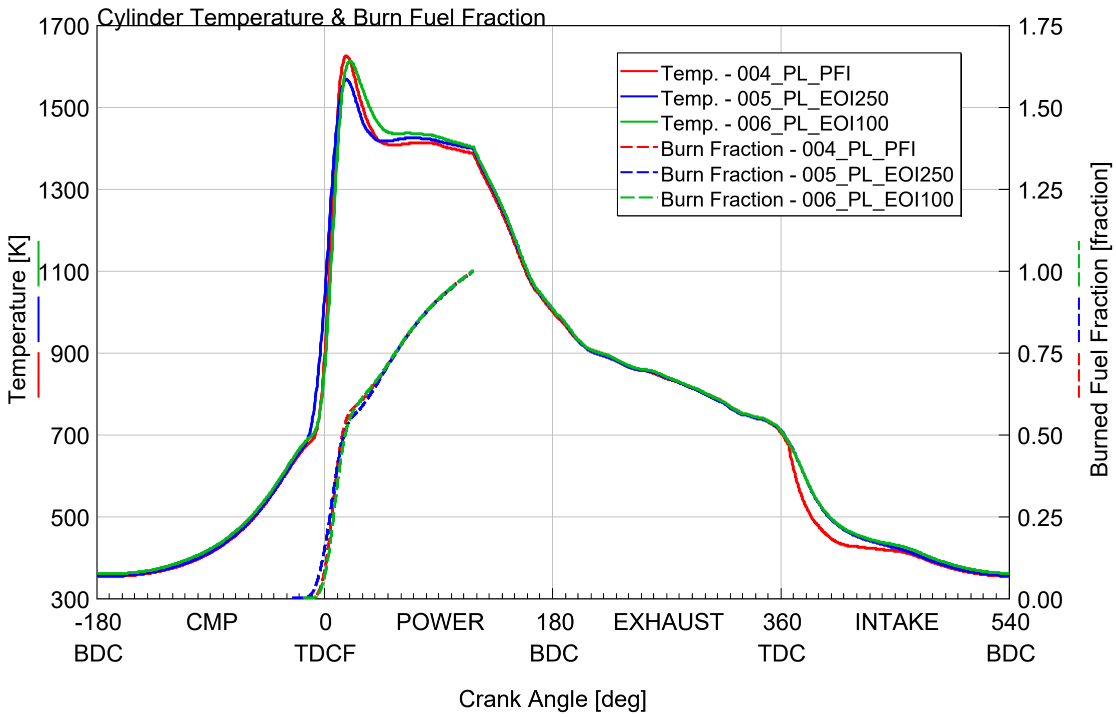

Figure 3.29: Engine cylinder temperature and burn fuel fraction

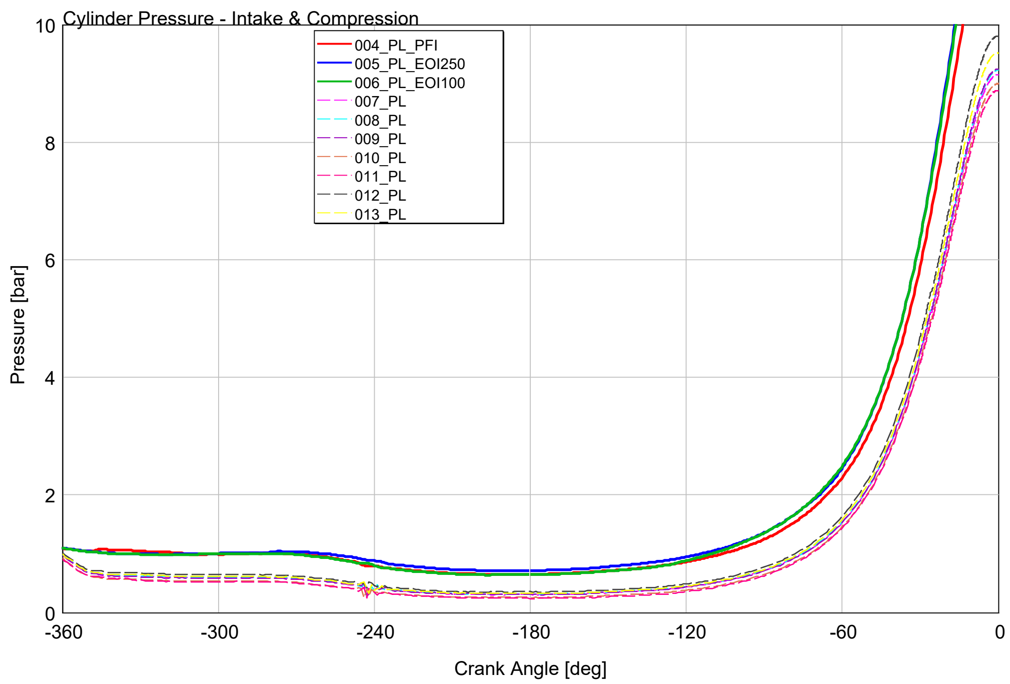

Figure 3.30: Engine cylinder pressures during intake and compression strokes

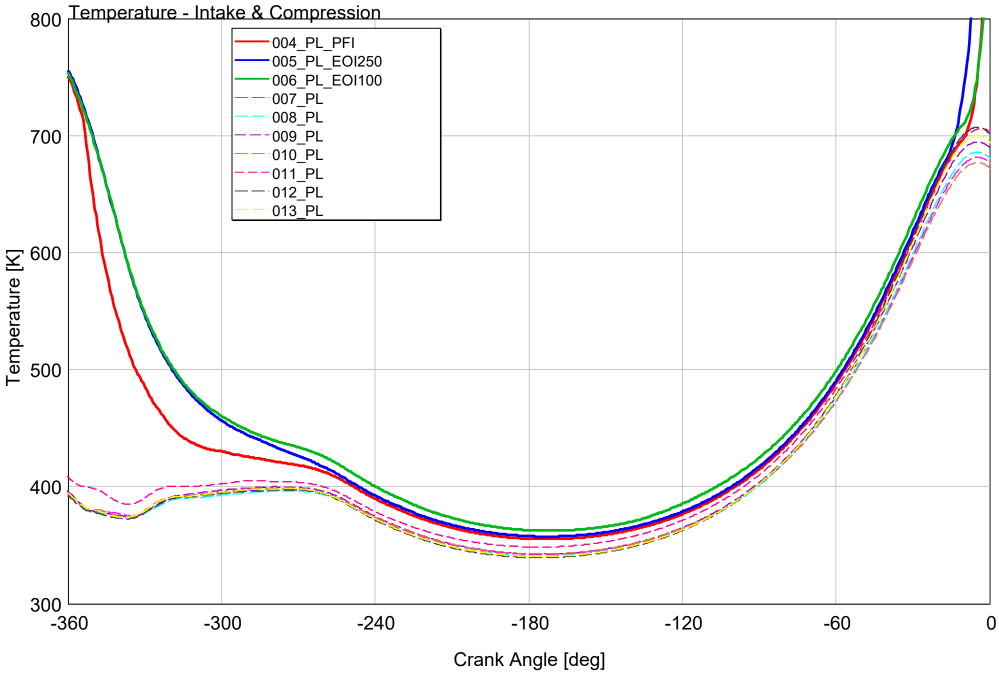

Figure 3.31: Engine cylinder temperatures during intake and compression strokes

Chapter 4

PLIF Investigation and Equivalence Ratio Calibration

The PLIF images were taken during the experimental process and the engine cylinder pressures and temperatures obtained from the numerical simulation in GT-Power. The first step is to obtain the equivalence ratio in motored condition from the ppm_HC measured by the lambda sensors installed on the exhaust ports. The second step is processing the PLIF images in motored and fired conditions to obtain the PLIF intensities in corresponding crank angle positions. The last step is to calibrate the equivalence ratio in fired condition through the PLIF intensities in motored condition and equivalence ratio at the same crank angle, in which it could consider and compensate the temperatures and pressures influence for intensities in motored condition.

4.1 Introduction to Planar Laser-Induced Fluorescence

4.1.1 Base of Laser Induced Fluorescence

The fluorescence is the emission property of some substances, by absorbing photons in the ultraviolet or visible spectral range, in which the emission wavelength is greater than the absorbed one.

In quantum mechanics, the atomic or molecular electrons tend to take the positions with the lowest energy, this energy level is called the ground state of atoms or molecules ($\boldsymbol{S_0}$). When the photons are absorbed, the electrons can be excited at high energy level ($\boldsymbol{S_1}$ or $\boldsymbol{S_2}$) according to $S_0 + hv_{EX} \rightarrow S_1$ or $S_0 + hv_{EX} \rightarrow S_2$. Because the excited state system is unstable, the electrons tend to the positions or levels with low energy by releasing energy with various modes [20]. Moreover, because the electromagnetic wavelength is inverse to electromagnetic energy, the energy of the emissions (fluorescence) is lower than that of incident photons. Therefore, there is a part of the energy released with non-radiative processes, such as rotation, vibration and collisional quenching.

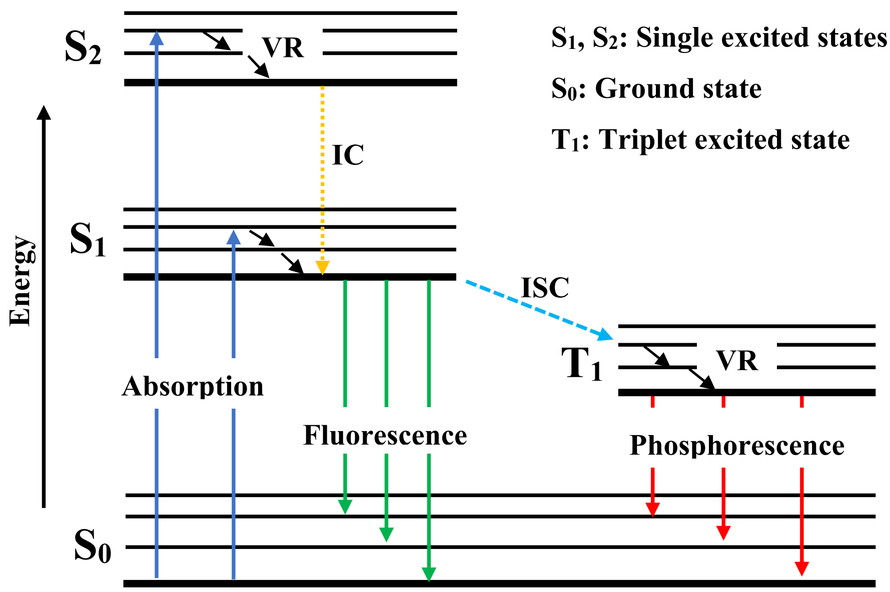

Figure 4.1: Jablonski diagram showing the relaxation mechanisms for excited state molecules

The Figure 4.1 shows the relaxation mechanisms for excited state molecules, there are two main type of process for releasing energy from the excited state, they are radiative process and non-radiative process.

- Radiative process: this part of excited energy is released from the excited state (S_1 and T_1) to the ground state (S_0) by emitting lights, for example fluorescence and phosphorescence.
  - Fluorescence: the spontaneous emissions are from the single excited state (S_1) to the ground state (S_0) according to $S_1 \rightarrow S_0 + hv_{fl}$ with the lift time of fluorescence about 1-100 ns.
  - Phosphorescence: the emissions are from the triplet excited state (T_1) to the ground state (S_0), because the spin multiplicity between these two states are different. Therefore, the lift time of the phosphorescence about millisecond to seconds.
- Non-radiative process: The other part of excited energy can be relaxed by vibrational and rotational energy transfer.
  - Internal conversion (IC): the radiationless transition between two states with the same spin multiplicity, for example from the single excited state S_2 to the single excited state S_1. Internal conversion is temperature dependent, which complicates the use of fluorescence to investigate the temperature dependent processes

  - Intersystem crossing (ISC): the radiationless transition between two states with the different spin multiplicity, for example from the single excited state S_1 to the triplet excited state T_1. When the triplet state returns to the ground state, the radiative phenomenon is phosphorescence.
  - Vibrational relaxation (VR): the molecule can transfer the excess vibrational energy to the surrounding environment in the form of heat and will jump from the high vibrational level of the excited state to the lowest vibratory level of the same excited state [21].

- Collisional quenching: quenching refers to any process which decreases the fluorescence intensity of a given substance. In quenching, solute molecules remove the extra energy from the excited state. There are two main factors that cause collisional quenching.
  - Electronic energy transfer: the emission of a photon by the excited molecules are absorbed by the ground state collider.
  - Quenching by molecular oxygen: The ground state of molecular oxygen is a triplet state, which enhance the transition into triplet states of the fluorescence molecules. The oxygen quenching plays an important role in the fuel concentration measurement.

The fluorescence emissions are influenced by many external factors, in addition, the fluorescence characteristics are different for the different types of substances, and the variation of the fluorescence intensity with the variations of pressure, temperature, concentration of oxygen and Laser wavelength, etc., specifically under engine conditions.

For high precision investigation of the parameters in the engine cylinder, such as temperatures, fuel concentration and combustion characteristics, these are a difficulty for PLIF in the engine applications.

4.1.2 Fluorescence quantum yield

Because there are non-radiative processes, not all excited molecules actually emit fluorescence. The fluorescence quantum yield (ϕ_{fl}) is a ratio between the number of photons emitted and the number of photons absorbed or the ratio between the number of molecules that emit photons and the number of molecules that absorb the photons [22].

$$\phi_{Int} = \frac{photons_{em}}{photons_{abs}} = \frac{N_{mel_{em}}}{N_{mel_{abs}}} \tag{4.1}$$

The fluorescence quantum yield can also be described as the ratio between the fluorescence process relative rate (k_{fl}) and the sum of relative rate of all processes

(k_{tot}), in which including fluorescence process relative rate and non-radiative processes relative rate (k_{nr}) ([21],[23]).

$$\phi_{fl} = \frac{k_{fl}}{k_{tot}} = \frac{\tau_{eff}}{\tau_{rad}} = \frac{k_{fl}}{k_{fl} + \sum k_{nr}} = \frac{k_{fl}}{k_{fl} + k_{isc} + k_{ic}} \tag{4.2}$$

Where, $\sum k_{nr}$ describes the sum of the rate for the non-radiative processes, these processes include intersystem crossing (ISC) and internal conversion (IC).

For low energy of excitation, the fluorescence signal is given by:

$$S_{fl} = \frac{E}{h\nu} V n_{fl} \sigma_{abs} \phi_{fl} \eta \frac{\Omega}{4\pi} \tag{4.3}$$

Where:
$\frac{E}{h\nu}$: photon flux;
n_{fl}: the number density of the fluorescence tracer in the collection volume V
σ_{abs}: the absorption cross-section
ϕ_{fl}: the fluorescence quantum yield
η: the efficiency of the detection system
$\frac{\Omega}{4\pi}$: the observed solid angle

The Equation 4.3 indicated that in the condition of low intensity of incident Lasers, the intensity of fluorescence signal is linearly proportional to the number of the fluorescence tracer under the premise that the absorption cross-section is constant, which is the basis of the LIF applications for concentration measurements.

The important factor influencing the fluorescence quantum yield is the collisional quenching, specifically under the engine conditions. Therefore, the denominator of the fluorescence quantum yield relationship should add a term of the quenching rate, which is the product of number density of the quencher n_q and rate coefficient of the quencher $\tilde{k}_q$. The fluorescence quantum yield relationship is as follows:

$$\phi_{fl} = \frac{k_{fl}}{k_{tot} + \tilde{k}_q n_q} \tag{4.4}$$

Usually, the tracer, such as 3-pentanone, toluene and acetone are dependence on temperature, pressure and oxygen number density. The collisional quenching process increasing due to the increase in oxygen density, results in a decrease of the fluorescence quantum yield. The fluorescence quantum yield decreases with increasing temperature, and the Degree of decline is different to the different tracers and different excitation wavelength ([24],[25],[26]). Moreover, at a certain pressure range, usually below 8 bar, the fluorescence quantum yield increases with the increasing pressure ([27],[28]).

4.1.3 Fuel-Air Ratio LIF

The strong quenching of some tracers by oxygen provides a possibility to measure directly the fuel/air equivalence ratio [29]. The Fuel/Air Ratio LIF (FARLIF) is a concept that directly measures fuel/air ratio using the dominant deactivation process by oxygen-quenching during the compression stroke in the internal combustion engines. For the certain experimental devices and tracers for visualization of PLIF

measurements, the fluorescence signal is proportional to the absorption cross-section and the fluorescence quantum yield. The fluorescence signal S_fl under the condition of oxygen quenching can be described by

$$S_{fl} \sim n_{fl} \cdot \sigma_{abs} \cdot \phi_{abs} \sim \sigma_{abs} \cdot \frac{k_{fl} \cdot n_{fl}}{k_{tot} + \tilde{k}_q n_q} \sim \frac{k_{fl} \cdot n_{fl}}{k_{tot} + \tilde{k}_q n_q} \tag{4.5}$$

The absorption cross-section is a probability of an absorption process for a certain substance at the different wavelength. The absorption cross-section at 248 nm has a negligible variable with temperature, this term can be negligible [30]. Moreover, the oxygen quenching is dominant in the non-radiative processes, i.e. $k_{tot} \ll ktildek_q n_q$ Thus, the signal fluorescence is proportional to the ratio of $\frac{n_{fl}}{n_q}$. The ratio between the number density of the fluorescence tracer and the quencher (oxygen) is proportional to the ratio of fuel and air (ϕ).

$$S_{fl} \sim \frac{k_{fl} \cdot n_{fl}}{\tilde{k}_q n_q} \sim \frac{k_{fl}}{\tilde{k}_q} \cdot \phi \tag{4.6}$$

The proportionality between Fuel/Air equivalence ratio and the fluorescence signal is valid in the limited condition. Because the internal conversion (IC), intersystem crossing (ISC) and vibrational relaxation (VR) are variable at different pressure and temperature. At the high temperature, the higher k_tot contributes a part of deactivation process that can not be negligible. Furthermore, the proportion of oxygen-quenching in the deactivation processes depends on the number density of oxygen (O_2). As a consequence, the fluorescence signal decreases with the increasing crank angle (the piston form B.D.C to T.D.C) in the internal combustion engine condition for 248 nm of excitation wavelength.

Therefore, in the engine conditions, the fluorescence signal can be described as follows:

$$S_{fl} \sim S_{fl}(T, p, n_{oxy}) \sim \frac{k_{fl}(T, P) \cdot n_{fl}}{k_{tot}(T, p) + \tilde{k}_q n_{oxy}} \tag{4.7}$$

4.1.4 Tracer

The first tracer for using FARLIF is the toluene by Reboux J and Puechberty D, due to the linear proportionality between equivalence ratio and fluorescence signal at room temperature for pressure less than 3 bar [29]. In the engine conditions, the temperature varies with crank angle in the range around 350-550 K. The fluorescence quantum yield has a strong temperature-dependence at high temperature at recent studies.

In the Section 2.3 (LIF Measurement of Mixing Process) it was reported that the tracer for the experiment is trimethylamine (TMA, C_3H_9N). The information about pressure and temperature dependence of TMA did not find from the references. Another amine, triethylamine (TEA, C_6H_15N), is matured in the applications of PLIF measurement. The fluorescence signal of tracer TEA-benzene shows a decrease of 23% for 100K increase, and at the pressure lower than 3 bar, the fluorescence single increases (18%/bar) when pressure increases [31].

The gaseous TMA under ambient conditions has confirmed that it is a tracer suitable in the hydrogen engine for PLIF measurements, moreover, the TMA molecule is smaller than the TEA molecule [32].

4.2 Equivalence ratio in motored condition

The sensor installed on the exhaust port cannot directly measure the lambda values, the measured values are the HC concentrations in volume (ppm Vol). The aim is to establish the relationship between ppm_HC measured by the sensor and the equivalence ratio of each case in motored condition. The Table 4.1 lists ppm_HC of each case in motored condition with the order from the maximum ppm_HC to the minimum one.

Case	ppm_Gasoline
	ppm_Vol
011_PL_PFI	2780
010_PL_PFI	2380
007_PL_PFI	2020
008_PL_PFI	1614
009_PL_PFI	1280
013_PL_PFI	906
012_PL_PFI	430

Table 4.1: ppm_HC measured in motored condition

The methodology for establishing the relationship between the ppm_HC and the equivalence ratio values is composed of two steps, the first step is the relationship from the ppm_HC (or ppm_Gasoline) to the ppm_Methane with the name Correlation I, and the second step is the relationship from the ppm_Methane to the equivalence ratio values with the name Correlation II. The relationship as follows:

$$\boldsymbol{ppm\_HC(ppm\_Gasoline)} \xrightarrow{\boldsymbol{CorrelationI}} \boldsymbol{ppm\_Methane} \xrightarrow{\boldsymbol{CorrelationII}} \boldsymbol{\phi}$$

The two relationships (Correlation I and II) are established by the curve fitting of the experimental data A and B. Considering the range of experimental data (A and B) for curve fitting, the range of ppm_HC and the coefficient of determination of curve fitting, the different methods and different fitting order must be comparisons to choose the best one.

4.2.1 Statistics fundamentals

The curve fitting uses the software Matlab and the function "lsqcurvefit", this function performs the fitting data through the least-squares method, obtaining as results the regressor coefficients.

The linear regression model in matrix form is:

$$\boldsymbol{Y} = \boldsymbol{X\beta} + \boldsymbol{\epsilon} \tag{4.8}$$

Where:

$$\boldsymbol{Y} = \begin{bmatrix} y_1 \\ y_2 \\ \vdots \\ y_n \end{bmatrix}, \quad \boldsymbol{X} = \begin{bmatrix} 1 & x_{11} & \cdots & x_{1k} \\ 1 & x_{21} & \cdots & x_{2k} \\ 1 & \vdots & \cdots & \vdots \\ 1 & x_{n1} & \cdots & x_{nk} \end{bmatrix}, \quad \boldsymbol{\beta} = \begin{bmatrix} \beta_0 \\ \beta_1 \\ \vdots \\ \beta_k \end{bmatrix}, \quad \boldsymbol{\epsilon} = \begin{bmatrix} \epsilon_1 \\ \epsilon_2 \\ \vdots \\ \epsilon_n \end{bmatrix}$$

$\boldsymbol{Y}$ is a vector of dependent variable (or observed values);
$\boldsymbol{X}$ is a matrix of independent variables;
$\boldsymbol{\beta}$ is the vector of regression coefficients;
$\boldsymbol{\epsilon}$ is the vector of error.

The result of regression coefficients ($\boldsymbol{\beta}$) must be that minimizes the sum of squares of the distances between observed and predicted data. The least-squares function is:

$$\boldsymbol{S} = \|\epsilon\|^2 = \|\boldsymbol{Y} - \boldsymbol{X\beta}\|^2 \tag{4.9}$$

The fitted regression model can be then written as:

$$\widehat{\boldsymbol{Y}} = \boldsymbol{X\beta} \tag{4.10}$$

Where, $\widehat{\boldsymbol{Y}}$ is the vector of fitting values.

After determining the regression coefficients ($\boldsymbol{\beta}$) using the least squares method, the coefficient of determination (R^2) is a parameter to determine the goodness of the fitting.

$$R^2 = \frac{SSR}{SST} = 1 - \frac{SSE}{SST} \tag{4.11}$$

Where:

- SSE: Sum of Squares of Error

$$SSE = \sum_{i=1}^{n}(y_i - \widehat{y}_i) \tag{4.12}$$

- SSR: Sum of Squares of Regression

$$SSR = \sum_{i=1}^{n}(\widehat{y}_i - \overline{y}) \tag{4.13}$$

- SST: Sum of Squares for Total

$$SSR = \sum_{i=1}^{n}(y_i - \overline{y}) = SSE + SSR \tag{4.14}$$

- $\overline{y}$: the average of dependent variables

$$\overline{y} = \frac{1}{n}\sum_{i=1}^{n} y_i \tag{4.15}$$

The coefficient of determination R^2 varies between 0 and 1, which gives the goodness of fitting or if the regression coefficients can predict the dependent variable.

- An R^2 of 0 means that the dependent variable cannot be predicted from the independent variable;
- An R^2 of 1 means the dependent variable can be predicted without error from the independent variable.

4.2.2 Correlation I: ppm_Gasoline - ppm_Methane

The experimental data A listed in the Table 4.2, from these experimental data, the relationship between ppm_HC and ppm_Methane (or Correlation I) can be established by the curve fitting.

ppm_Gasoline	ppm_Methane
ppm_Vol	ppm_Vol
440	12500
777	27000
900	33000
992	39000
1192	51000
1500	72800
1700	83400
1906	93200
2000	97891

Table 4.2: The experimental data A from ppm_Gasoline to ppm_Methane

The ppm_Gasoline values are the independent variables ($\boldsymbol{X}$), and the ppm_Methane values are the dependent variables ($\boldsymbol{Y}$), combining the experimental data A and the linear regression model (Equation 4.9). The curve fitting results can be calculated by the function "lsqcurvefit". The curve fitting in I order and III order are executed during the test for the Correlation I, in which the curve fitting in III order reverse dependent variables and independent variables in the fitting in III order, thus, the ppm_Gasoline values are the dependent variables ($\boldsymbol{Y}$), and the ppm_Methane values are the independent variables ($\boldsymbol{X}$).

The Figure 4.2 shows curve fitting in I and III order and experimental data A, and the Table 4.3 lists the results of regression coefficients and coefficient of determination R2 of these two types of curve fitting.

If only from the coefficient of determination (R2) and the fitting curves in I order and in III order, the curve fitting in III order has better predicted ppm_Methane from ppm_Gasoline (or ppm_HC) in motored condition. However, the coefficient of determination is not the only parameter for deciding the order choice of fitting. The rationality and range of experimental data must be considered.

Because the ppm_Gasoline range of experimental data A is [440, 2000], which is lower than ppm_HC in motored condition, [430, 2780]. Moreover, the ppm_Methanes predicted in III order has the high differences with those in I order at the two extremes of the interval, and the fitting in I order is more reasonable than fitting in III order considering the possibility of linear relationship between ppm_Gasoline

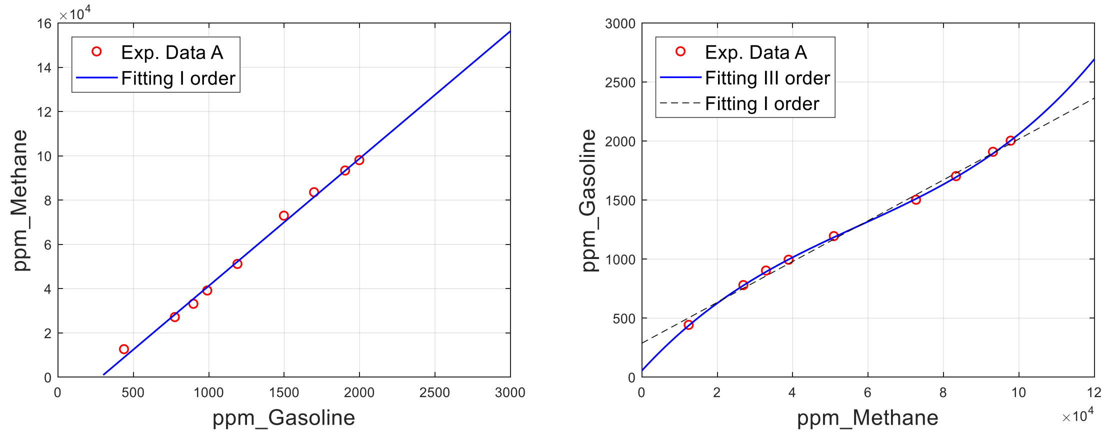

Figure 4.2: The experimental data and curve fitting in I order (left) and in III order (right)

	$y = a \cdot x + b$	$y = a \cdot x^3 + b \cdot x^2 + c \cdot x + d$
y	ppm_Methane	ppm_Gasoline
x	ppm_Gasoline	ppm_Methane
a	57.5454	2.04E-12
b	-16292.1	-3.51E-07
c	∼	0.0348
d	∼	55.5626
R^2	99.52%	99.98%

Table 4.3: The results of curve fitting in I order and in III order for the Correlation I

and ppm_Methane. Therefore, the Correlation I is the curve fitting in I order, the relationship to calculate ppm_Methane predicted by ppm_Gasoline in motored condition is as follows.

$$ppm\_Methane = 57.5454 \cdot ppm\_Gasoline - 16292.1 \tag{4.16}$$

From the Equation 4.16 of Correlation I the ppm_Methane values can be calculated from ppm_HC measured in motored condition. The Table 4.4 lists the results of the ppm_Methane in motored condition.

Exp. Data in motored condition		ppm_Methane
Case	ppm_Gasoline	Correlation I
011_PL_PFI	2780	143683.99
010_PL_PFI	2380	120665.85
007_PL_PFI	2020	99949.52
008_PL_PFI	1614	76586.11
009_PL_PFI	1280	57365.96
013_PL_PFI	906	35843.99
012_PL_PFI	430	8452.41

Table 4.4: The results of ppm_Methane in cases of motored condition

4.2.3 Correlation II: ppm_Methane-Equivalence Ratio

There are two methods for obtaining the Correlation II (the relationship between ppm_Methane and equivalence ratio).

The first method is the same method of the Correlation I, through curve fitting of experimental data B. The Table 4.5 lists the experimental data B, those are from ppm_Methane to equivalence ratio. The experimental data are at different engine speeds, but which has no influences for the relationship between ppm_Methane and equivalence ratio.

The ppm_Methane values are the independent variables ($\boldsymbol{X}$), and the values of equivalence ratio are the dependent variables ($\boldsymbol{Y}$), combining the experimental data B and the linear regression model (Equation 4.9). The curve fitting results can be calculated by the function "lsqcurvefit". The curve fitting in I order during the test for the Correlation II. The Table 4.6 lists the results of regression coefficients and coefficient of determination R2 of the curve fitting in I order. The coefficient of determination of curve fitting in I order is about 96%, which indicates a high linearity between the ppm_Methane and the equivalence ratio.

The second method is starting from the definition of ppm_Vol. Partes per million by volume (ppm_Vol) is a commonly used unit of concentration for small values, 1 ppm_Vol is one volume of solute (Methane) per one million volumes of solvent (Air and Methane). From the definition of ppm_Vol, the relationship between the ppm_Vol and the ratio of the methane and air mass can be found, and the relationship is as follows:

speed	ppm_Methane	Lambda	1/Lambda
rpm	ppm_Vol	Relative FAR	ϕ
2000	112436	0.82	1.220
2000	105103	0.86	1.163
2000	102659	0.9	1.111
2000	95326	1	1.000
2000	85549	1.2	0.833
2000	78216	1.33	0.752
2000	73328	1.35	0.741
1500	99725	0.878	1.139
1500	94544	0.943	1.060
1500	91415	1.015	0.985
1500	87064	1.096	0.912
1500	78020	1.259	0.794

Table 4.5: The experimental data B from ppm_Methane to Equivalence ratio

$$\begin{aligned} ppm_{CH_4} &= \frac{V_{CH_4}}{V_{CH_4}+V_{air}} \cdot 10^6 = \frac{1}{\left(\frac{V_{CH_4}+V_{air}}{V_{CH_4}}\right)} \cdot 10^6 = \frac{1}{\left(1+\frac{V_{air}}{V_{CH_4}}\right)} \cdot 10^6 \\ &= \frac{1}{\left(1+\frac{m_{air}}{m_{CH_4}} \cdot \frac{\rho_{CH_4}}{\rho_{air}}\right)} \cdot 10^6 \end{aligned} \tag{4.17}$$

The air/fuel ratio (AFR) is equal to:

$$AFR = \frac{m_{air}}{m_{CH_4}} = \frac{\rho_{air}}{\rho_{CH_4}} \cdot \left(\frac{1}{ppm_{CH_4}/10^6} - 1\right) \tag{4.18}$$

From the ideal gas law ($pv = nRT$), the ratio of the density between methane and air can be obtained.

$$\frac{\rho_{air}}{\rho_{CH_4}} = \frac{\frac{M_{CH_4}}{V} \cdot \frac{p}{RT}}{\frac{M_{CH_4}}{V} \cdot \frac{p}{RT}} = \frac{M_{CH_4} \cdot \frac{p}{RT}}{M_{CH_4} \cdot \frac{p}{RT}} = \frac{M_{CH_4}}{M_{air}} = \frac{16.04g/mol}{28.96g/mol} = 0.5539 \tag{4.19}$$

Combining the Equations 4.18, 4.19 and the definition of the equivalence ratio, the equivalence ratio is equal to:

$\phi = a \cdot ppm\_Methane + b$	
a	1.37E-05
b	-0.2847
R^2	95.898%

Table 4.6: The results of curve fitting in I order for the Correlation II

$$\begin{aligned}\phi &= \frac{AFR_{stoich}}{AFR} = \frac{AFR_{stoich}}{\frac{\rho_{air}}{\rho_{CH_4}} \cdot \left(\frac{1}{ppm_{CH_4}/10^6} - 1\right)} \\ &= \frac{AFR_{stoich}}{\frac{M_{air}}{M_{CH_4}} \cdot \left(\frac{1}{ppm_{CH_4}/10^6} - 1\right)} = \frac{AFR_{stoich}}{\left(\frac{1}{ppm_{CH_4}/10^6} - 1\right)} \cdot \frac{M_{CH_4}}{M_{air}}\end{aligned} \tag{4.20}$$

Finally, the theoretical relationship between the equivalence ratio and the ppm_Methane can be obtained.

$$\phi = \frac{17.2}{\left(\frac{1}{ppm_{CH_4}} \cdot 10^6 - 1\right)} \cdot 0.5539 \tag{4.21}$$

Since the values of ppm_Methane are much lower than 10^6, in the denominator of the Equation 4.21, it can be negligible compared to the ratio between 10^6 and ppm_Methane. Therefore, the relationship between the equivalence ratio and the ppm_Methane is linear, when the values of ppm_Methane are small.

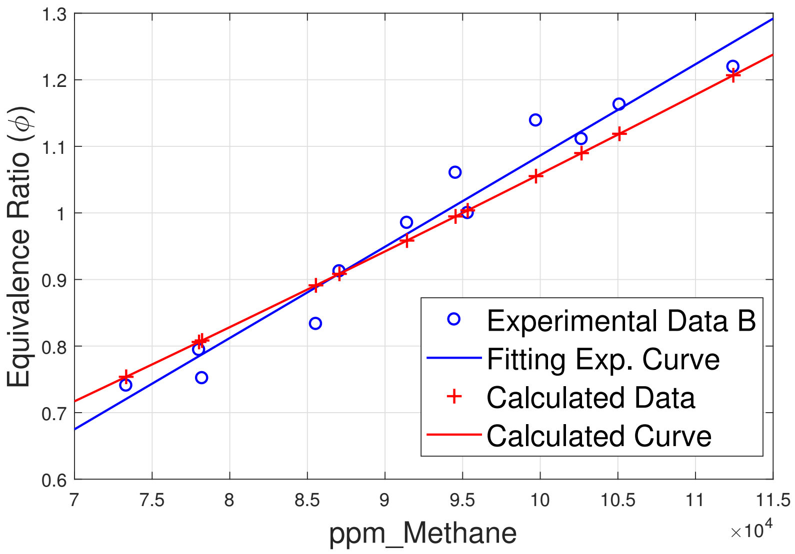

Figure 4.3: The experimental data B, curve fitting in I order and curve calculated for Correlation II

The Figure 4.3 shows the experimental data B, the curve fitting in I order and the calculated curve for the Correlation II, the slop of the curve fitting and that of the calculated curve are different. Moreover, the range of the experimental data B is about [78000, 112500], which is much lower than the range of the ppm_Methane in motored condition, about [8500, 144000].

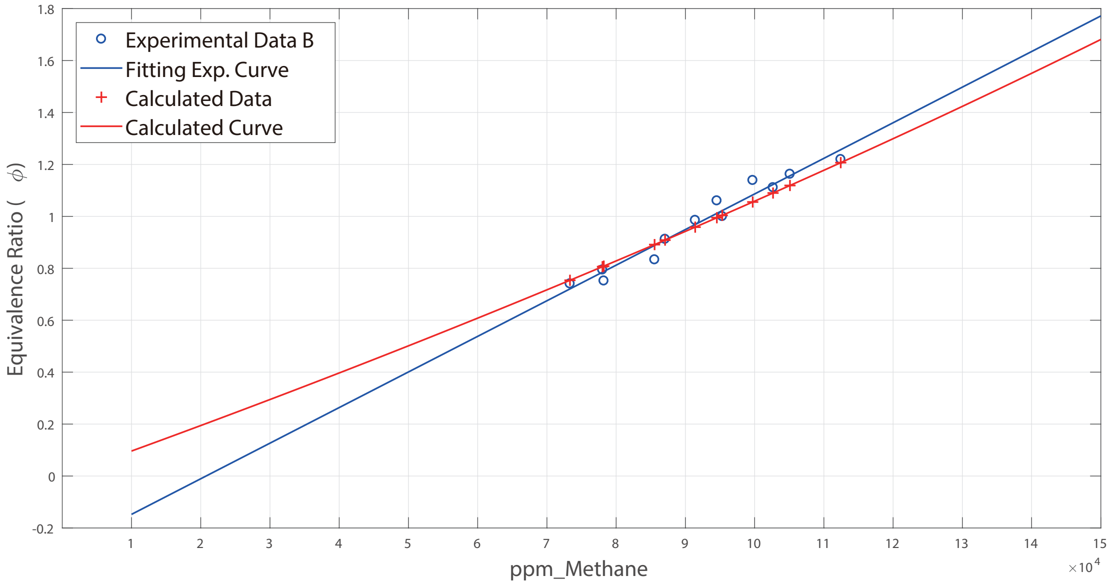

Figure 4.4: The results of curve fitting in I order and calculated curves in the range of ppm_Methane in motored condition

The Figure 4.4 shows the results of curve fitting in I order and calculated curves in the range of ppm_Methane in motored condition. The values of ppm_Methane in motored condition are outside the two extremes of the experimental data range B. Therefore, it cannot predict the vales of equivalence ratio in these intervals by curve fitting. Moreover, the Figure 4.4 indicates that the equivalence ratio is lower than 0 when ppm_Methane less than 20000.

In the end, the Equation 4.21 is the Correlation II to calculate the equivalence ratio from ppm_Methane. And the Table 4.7 shows the results of the equivalence ratios in motored condition that are obtained from the ppm_HC by the Correlations I and II.

Exp. Data in motored condition		ppm_Methane	Equivalence ratio
Case	ppm_Gasoline	Correlation I	Correlation II
011_PL_PFI	2780	143683.99	1.598
010_PL_PFI	2380	120665.85	1.307
007_PL_PFI	2020	99949.52	1.058
008_PL_PFI	1614	76586.11	0.790
009_PL_PFI	1280	57365.96	0.580
013_PL_PFI	906	35843.99	0.354
012_PL_PFI	430	8452.41	0.081

Table 4.7: The experimental data B from ppm_Methane to Equivalence ratio

4.3 PLIF Images Processing

4.3.1 Introduction to image processing

In the Subsection 3.2.1 introduced the naming of the tests of cases in fired condition, in which, the last part of the name is the crank angle position for PLIF images. The Table 4.8 lists all the crank-angle positions (BTDC) for PLIF images in both motored and fired conditions.

In motored condition, the mixture between natural gas and air is uniform, therefore, in theory the PLIF intensity is uniform throughout the cylinder area, there are 4 crank-angle positions to analyze the relationship between the PLIF intensity and equivalence ratio. Instead, the crank-angle positions in fired conditions are different for each case, the crank-angle positions cover the crank angles from the beginning of the injection to before the ignition. There are two factors that restrict the crank-angle positions in fired condition. The first factor is that the limited Laser accesses from the side of glass liner in the range of 30Â° CA before and after TDC, therefore, for case 004_PL_PFI the first crank angle position is the crank angle near the end of injection (EOI = -320 CA BTDC). Another factor is that the Laser itself may ignite the mixture when the piston is close to the TDC in the compression stroke, therefore, the last crank angle position is -040 CA BTDC for all fired condition cases.

Motored condition	Fired condition		
Case 007∼013	Case 004	Case 005	Case 006
-050	-040	-040	-040
-100	-060	-060	-050
-150	-100	-100	-060
-180	-150	-125	-070
	-200	-150	-080
	-225	-175	-090
	-250	-200	-095
	-260	-220	-100
	-270	-230	-105
	-280	-240	-110
	-290	-250	-115
	-300	-260	-120
	-310	-270	-125
	-320	-275	-130
	-330	-280	-132

Table 4.8: PLIF images crank angles (CA BTDC) positions

During the PLIF measurements experimentation, 36 PLIF images are taken for each crank angle position to reduce the causal error, and the resolution is 520X696 pixels. There are two types of images taken for each crank angle position in both motored and fired conditions, those are AR and AD.

- AR: PLIF images in which the tracer is solute in natural gas with a stratified mixture;
- AD: Reference images with the same crank-angle positions of images AR, which can eliminate reflections and other noise in the post-processing of images by subtraction of reference images

Before the post processing of the PLIF images, the images AR and AD can be extracted directly from the AVL VisioScope software, those images are in matrix type with the dimension 361920×3, where the first column is the positions of x, the second column is the positions of y and the third column is the PLIF intensities.

These matrixes can be converted to the other matrixes with the dimension 520×696, in which the elements are the PLIF intensities at the corresponding position x and y. All post-processing processes of PLIF images are established on the 520X696 matrix.

The Figure 4.5 shows the methodology for PLIF images processing to an example of PLIF image in motored condition. The Net image is obtained through the image AR subtracting the image AD (reference image) to eliminate reflections and other noise. Then, in order to eliminate the influence of the refraction and reflection of the lights in the glass liner, the Net image subtracting the Background image is the Corrected image, which is the final image to calibrate and analyze.

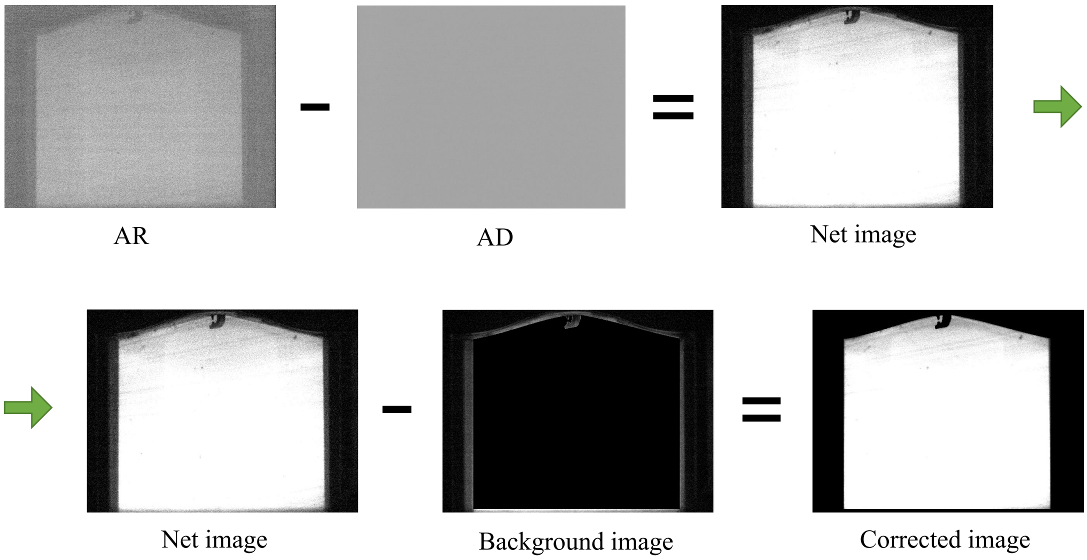

Figure 4.5: Methodology for the post processing of the PLIF images

In order to find the edge between the cylinder (PLIF intensity) and background zones, the edge detection operation must be performed. In the software Matlab there are two functions to detect the edge of the image, those are "bwperim" and "edge". The function "bwperim" is based on the gradient of image elements (pixels), and the function "edge" use the Sobel operator, which is based on the convolution of the image. The Figure 4.6 shows the results of the edge detection in the crank angle equal to -100, -150 and 180, the two function can detect edge of the PLIF image, where the function "bwperim" has a better result. The Edge image (bottom right) is the result from the lineality of the edge detected by the function "bwperim", and the edge image is the edge of the background image.

With the same methodology, the edge image in -50 CA BTDC can be detected, ss shown in the Figure 4.7. In the image (edge (Sobel): top right) there are two lower edges due to the shadow from the piston with low luminosity.

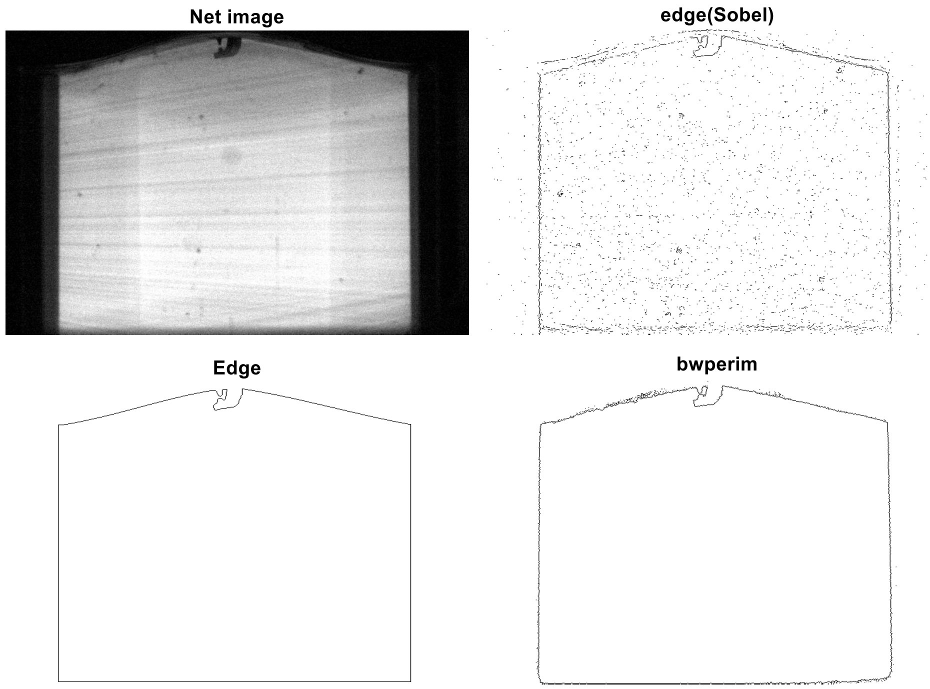

Figure 4.6: The results of edge detection in -100, -150 and -180 CA BTDC

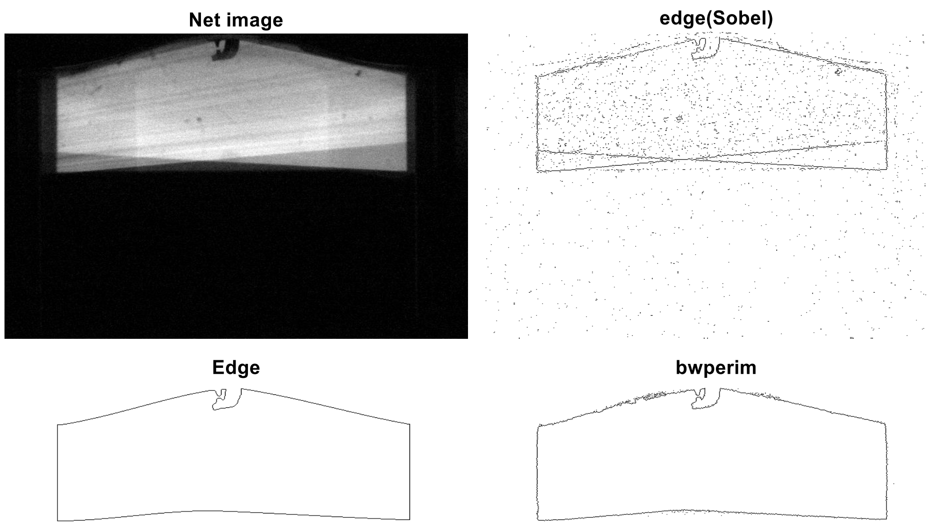

Figure 4.7: The results of edge detection in -050 CA BTDC

All the edge images can be detected using the edge detection, the background images can be obtained from the edge images before the PLIF images processing.

4.3.2 PLIF images in motored condition

After obtaining the background images of all the CA positions by the edge detection, the next step is to obtain the PLIF intensity images in motored condition. The Figure 4.8 shows the PLIF intensity images in case 007_PL_PFI, the statistical data of intensities and the histogram of intensities. The PLIF intensity images of the other cases are shown in the Appendix C.1.

Because of some factors, for example, the reflection of the glass liner and the machines on the glass liner, the PLIF intensities are not uniform. The reflection makes more luminosity concentrated in the central zone of the image PLIF, and in the central area there is a stain that makes a small area with low luminosity. Moreover, the statistic process of intensities can know uniformity of intensities and Signal-to-Noise Ratio (SNR) of the PLIF intensity image.

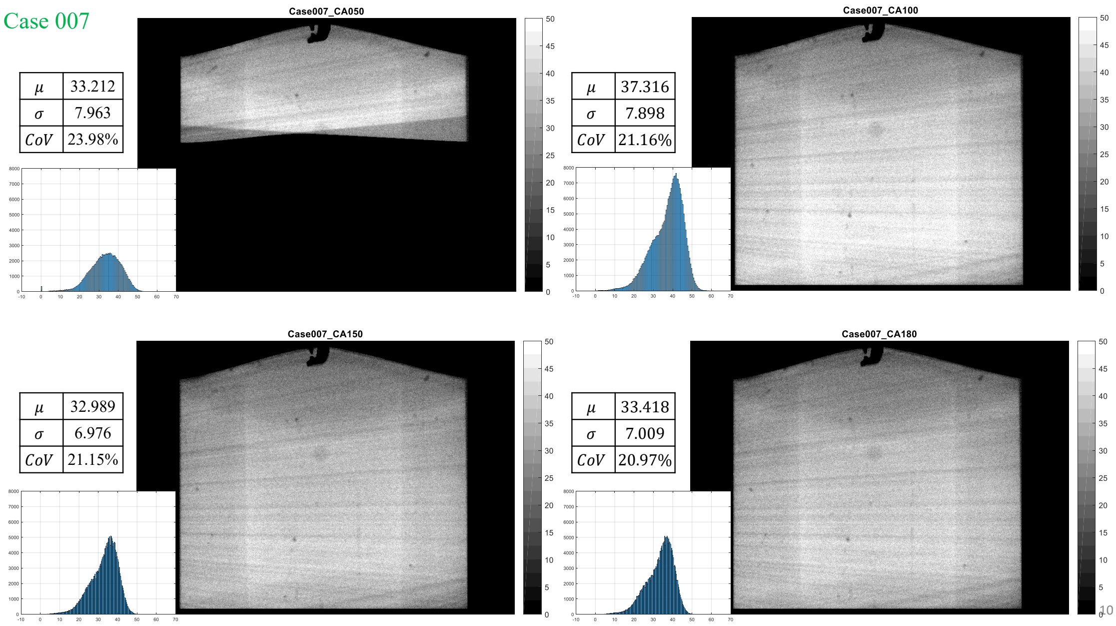

Figure 4.8: PLIF intensity images and statistical data in case 007_PL_PFI

The Table 4.9 lists all statistical data of cases in motored condition, including mean value, Standard deviation and coefficient of variation (CoV) of the PLIF intensities. When the equivalence ratio decreasing, decreasing the tracer concentration in the combustion chamber, the mean value of the PLIF intensities decreases, moreover, the coefficient of variation (CoV) increases. Specifically, in the 012_PL_PFI case, the coefficient of variation is about 75%. Therefore, in the step for calibration equivalence ratio in fired condition, the 012_PL_PFI and 013_PL_PFI cases are two particular cases due to high coefficient of variation.

		Case 007	Case 008	Case 009	Case 010	Case 011	Case 012	Case 013
	ϕ	1.058	0.790	0.580	1.307	1.598	0.081	0.354
CA050	μ	33.212	24.324	18.334	43.327	54.633	3.758	10.035
	σ	7.963	6.043	4.967	10.181	12.666	2.820	3.670
	CoV	23.98%	24.84%	27.09%	23.50%	23.18%	75.04%	36.57%
CA100	μ	37.316	26.450	18.501	48.879	62.946	3.938	11.079
	σ	7.898	5.792	4.564	10.069	12.702	2.806	3.483
	CoV	21.16%	21.90%	24.67%	20.60%	20.18%	71.24%	31.44%
CA150	μ	32.989	23.402	16.102	41.994	61.875	3.286	9.756
	σ	6.976	5.370	4.114	8.688	11.244	2.802	3.347
	CoV	21.15%	22.95%	25.55%	20.69%	18.17%	85.28%	34.31%
CA180	μ	33.418	22.899	15.937	42.850	54.997	3.151	9.316
	σ	7.009	5.210	4.066	8.720	10.985	2.795	3.228
	CoV	20.97%	22.75%	25.51%	20.35%	19.97%	88.70%	34.65%

Table 4.9: All of the statistical data of cases in motored condition.

4.3.3 PLIF images in fired condition

The methodology for the PLIF images processing of cases in fired condition is equal to that in fired condition. At first, the Net images are obtained from images AR by subtracting images AD at the same crank angle position, then, the Background images must be found by the edge detection processing. At the last, the Corrected images can be obtained through the net images by deleting the Background images. The Figure 4.9 shows the PLIF intensity images after the PLIF images processing. In the Appendix C.2, the PLIF intensity images in 005_PL_EOI250 and 006_PL_EOI100 cases are shown. The luminosities of PLIF images can indicate the mixture formation process, which can indicate just the relative concentration of natural gas, but cannot indicate the actual (absolute) concentration of natural gas. Therefore, the next step is to calibrate the equivalence ratio of cases in fired condition.

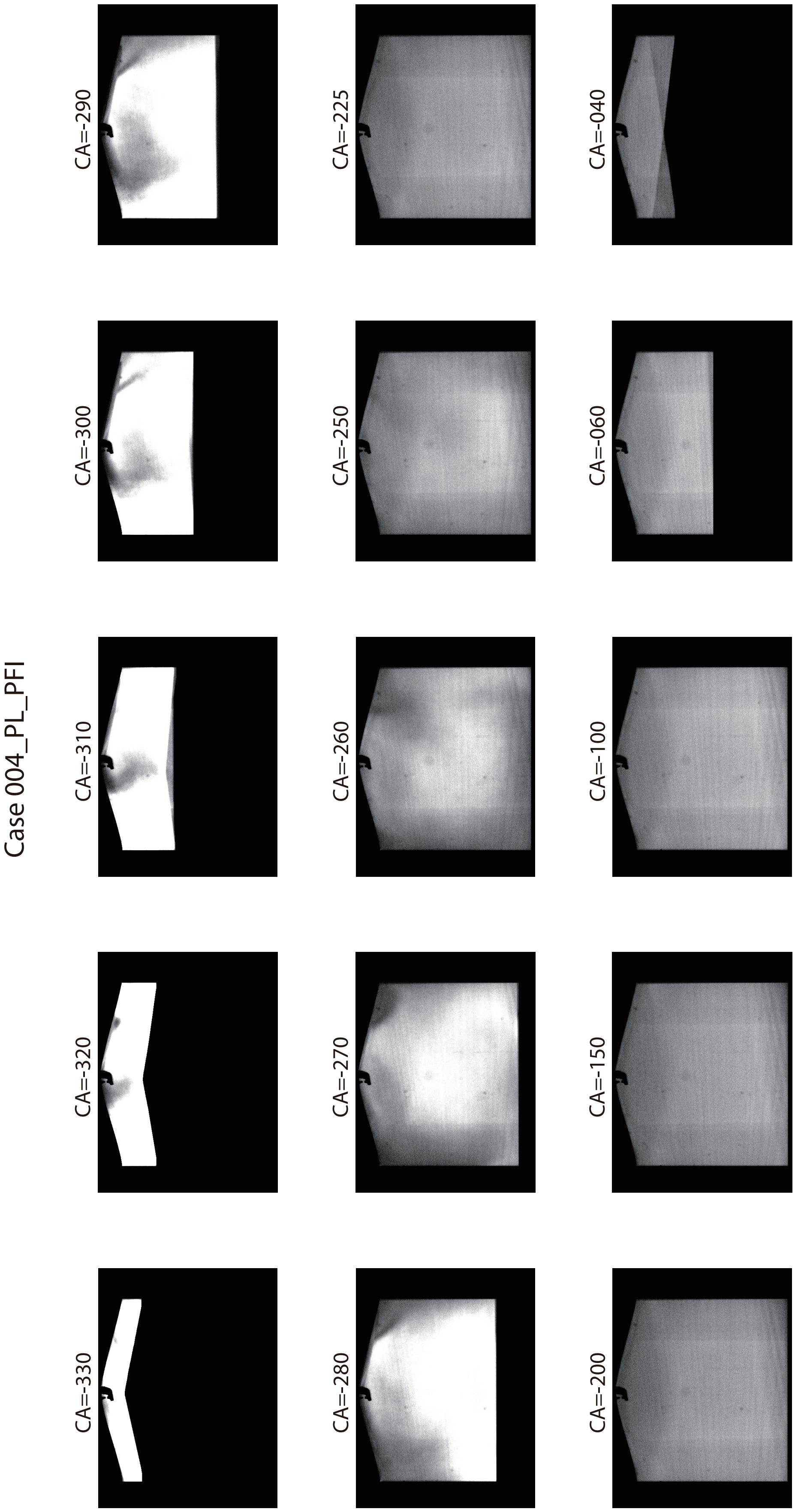

Figure 4.9: PLIF intensity images in case 004_PL_PFI

4.4 Equivalence ratio calibration

After obtaining the PLIF intensity and equivalence ratio in motored condition, the next step is to establish a relationship between them. Usually, the premise of the in-situ calibration is that to guarantee the same engine conditions between motored and fired engine operations ([33], [34]), the advantage of the in-situ calibration is that it avoids the semi-empirical model to determine the influence of pressure and temperature.

However, due to the port fuel injection (PFI) in motored operation, the intake port pressure has around 100 bar of decline compared to the fired operation (in direct injection), which causes the differences in the cylinder pressure and temperatures between motored and fired conditions. Moreover, the crank angle distribution for PLIF images are different between each case, as shown in the Figure 4.10. Therefore, an in-situ calibration is not feasible.

During the calibration, it is best to consider the pressure and temperature influences at PLIF intensity, if possibly. Thus, the equivalence ratio results at high temperatures and pressures (piston closed to TDC: before ignition) have a high precession by correcting the effects of temperature and pressure.

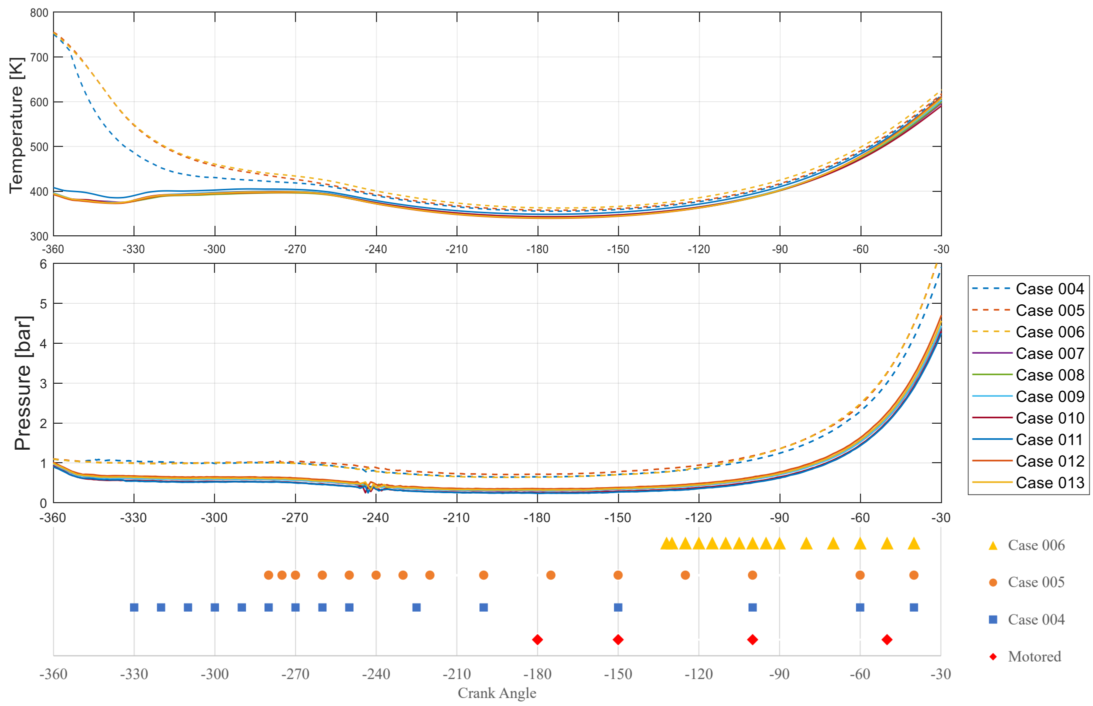

Figure 4.10: The CAs for PLIF images and the trends of the cylinder pressures and temperatures

4.4.1 The relationship between PLIF intensity and equivalence ratio

In the Table 4.9 of the Subsection 4.3.2 (PLIF images in motored condition), the mean values of the statistical data are the average PLIF intensities, in the Table 4.10 lists the average PLIF intensities with different equivalence ratios and cases in motored condition.

Case	ϕ	CA=-180	CA=-150	CA=-100	CA=-050
Case 011	1.5985	54.99739	61.87534	62.94598	54.63280
Case 010	1.3073	42.85039	41.99381	48.87935	43.32717
Case 007	1.0580	33.41849	32.98861	37.31627	33.21215
Case 008	0.7901	22.89861	23.40214	26.45010	24.32434
Case 009	0.5798	15.93737	16.10195	18.50124	18.33441
Case 013	0.3542	9.315832	9.756303	11.07870	10.03519
Case 012	0.0812	3.150908	3.285985	3.938226	3.758401

Table 4.10: Average PILF intensity of cases in motored condition

In order to observe the trends of the average PLIF intensities vary with the crank-angle positions (or cylinder pressure and temperature), the Figure 4.11 plots the average PLIF intensities, cylinder pressures and cylinder temperatures vary with the crank-angle positions.

Unfortunately, due to some factors:

- little samples to analyze could have a high random error;
- the shadow in PLIF images of CA050 lowers the average PLIF intensities;
- gaseous natural gas could decrease the dominate of quenching rate for high equivalence ratio cases.

The influences of temperature and pressure are non-significant on the PLIF intensity. Therefore, the first calibration method is that assuming the PLIF intensity is constant with the temperature and pressure, which means that it does not consider the effects of temperature and pressure. Moreover, the gaseous natural gas has a significant volume in the combustion chamber, which causes a reduction in oxygen concentration, especially in the area with a high concentration of natural gas (the jet core). Therefore, it is impossible to quantify the equivalence ratios in this area [32].

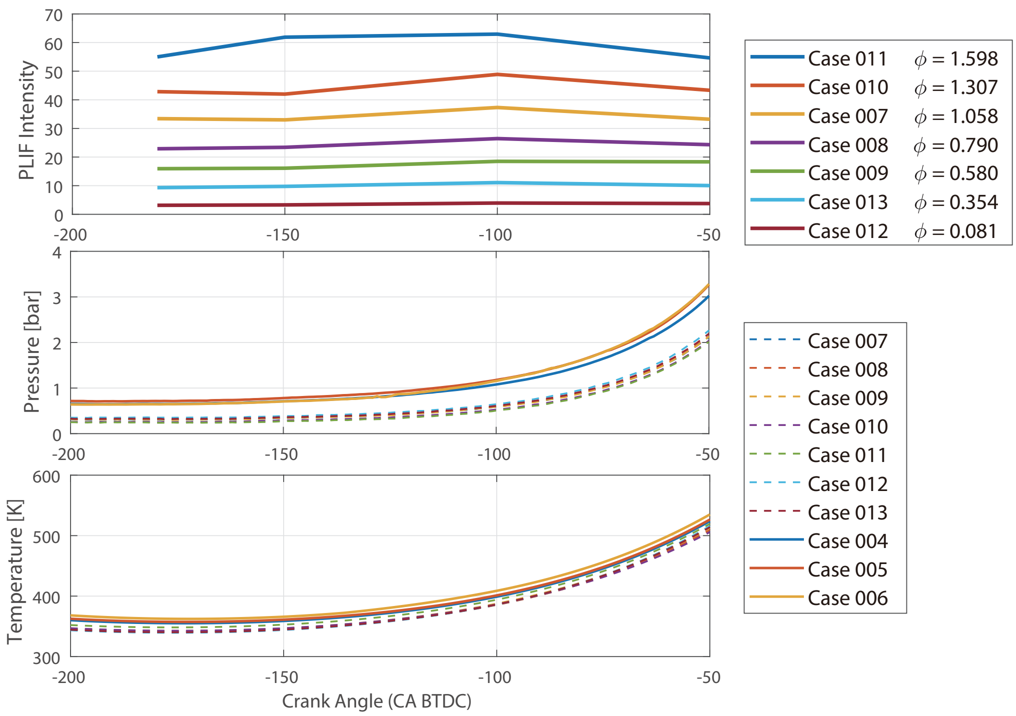

Figure 4.11: Average PLIF intensities, temperatures and pressures in motored condition

The relationship between the PLIF intensity and equivalence ratio is established by curve fitting of the data in the Table 4.10. In experimentation, the equivalence ratios in motored conditions are between 0.1 and 1.6, the interesting interval of the equivalence ratio is between 0 and 2. Therefore, the choice of the calibration curve relationship considers not only the goodness of fitting (coefficient of determination, R^2), but also the trend of the PLIF intensity in the equivalence ratio close to 2.

The Figure 4.12 shows the calibration curve fitting in I and II order, where the horizontal axis is the equivalence ratio, and the vertical axis is the average PLIF intensity values. The curve fitting in II order has a high coefficient of determination, but has a decline when PLIF intensity greater than 100, in which the maximum equivalence ratio is 1.9 for curve fitting in II order, the results of the curve fitting in II order is not reasonable.

Another type of curve fitting is shown in the Figure 4.13, where the horizontal axis is the values of average PLIF intensity, and the vertical axis is the equivalence ratio. The curve fitting in II order has a coefficient of determination 98.73%, which is greater than fitting in I order, moreover, for equivalence ratio less than 2, fitting in II order is suitable

Finally, the Equation (4.22) is the relationship of calibration curve under conditions of no influence of pressure and temperature.

$$Intensity = 8.8667 \cdot \phi^2 + 21.3166 \cdot \phi + 1.6837 \tag{4.22}$$

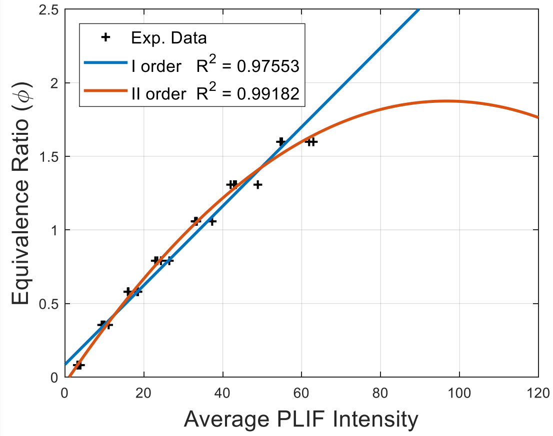

	$\phi = a \cdot I^2 + b \cdot I + c$	$\phi = a \cdot I + b$
a	-0.0002	0.0269
b	0.0397	0.0853
c	-0.0428	-
R^2	99.18%	97.55%

Figure 4.12: Calibration curve fitting in I and II order (x: PLIF intensity; y: Equivalence ratio)

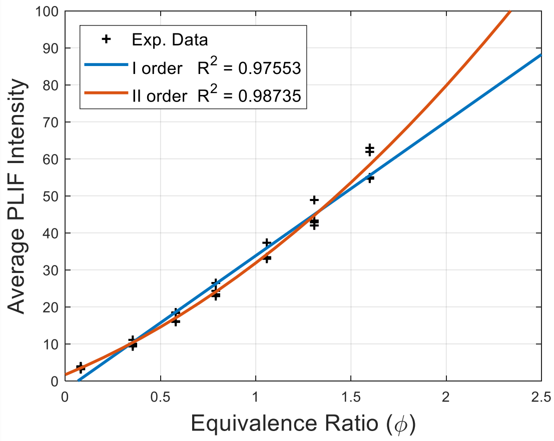

	$I = a \cdot \phi^2 + b \cdot \phi + c$	$I = a \cdot \phi + b$
a	8.8667	36.2475
b	21.3166	-2.4187
c	1.6837	-
R^2	98.73%	97.55%

Figure 4.13: Calibration curves fitting in I and II order (x: Equivalence ratio; y: PLIF intensity)

4.4.2 The equivalence ratio without correction

Using the Equation (4.22), the results of equivalence ratio in fired condition can be obtained in condition that does not consider the non-uniformity of the PLIF intensity in motored condition and the influences of pressure and temperature. All results of equivalence ratio maps are shown in the Appendix C.3. Combining the results of equivalence ratio and theoretical analysis, some errors can be found for calibration without correction.

The Cases 004_PL_PFI and 005_PL_EOI250 have early injection strategies, in theory, at the end of compression stroke, the distribution of the mixture tends to uniform. Because non-uniformity of the PLIF images in motored condition, high equivalence ratio (high fuel concentration) zone is located in the central zone, specifically when the piston is close to the TDC. This phenomenon can be seen in the Figures 4.14 and 4.15. In addition, the case 006_PL_EOI100 has a delay injection strategy, in the CA position is 090 before TDC, the reflected natural gas jet by the piston crown should rise to the cylinder head along the cylinder wall. However, in the Figure 4.16, the analyzed results are not consistent with the calibration results, the reflected natural gas jet stops at the central zone of the cylinder.

The equivalence ratio maps of calibration without correction have many errors, specifically for the uniformity of the mixture at the end of compression stroke and the movement of the injection jet. Therefore, the non-uniformity of the PLIF images that is caused by the reflection of the glass liner in the motored condition has a significant influence on the equivalence ratio results.

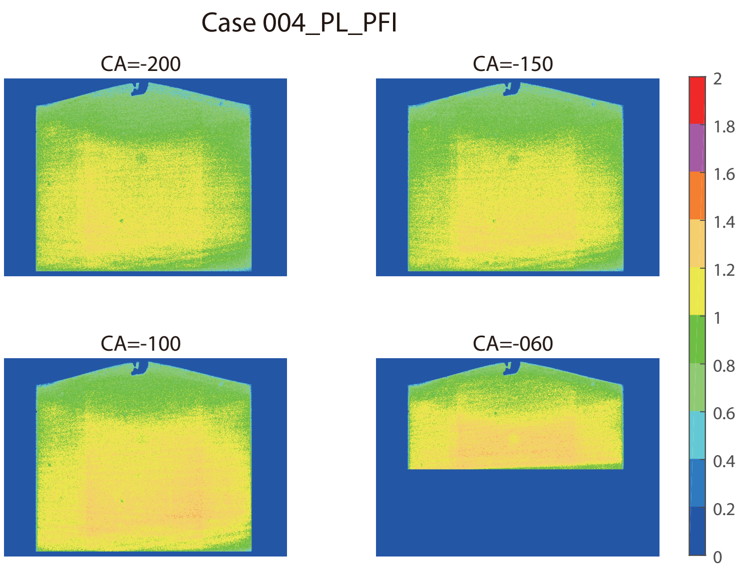

Figure 4.14: Equivalence ratio without correction in case 004_PL_PFI

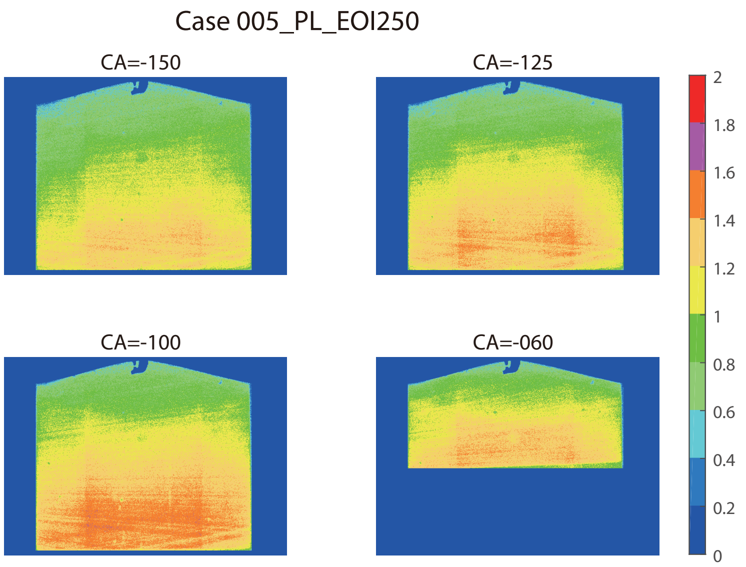

Figure 4.15: Equivalence ratio without correction in case 005_PL_EOI250

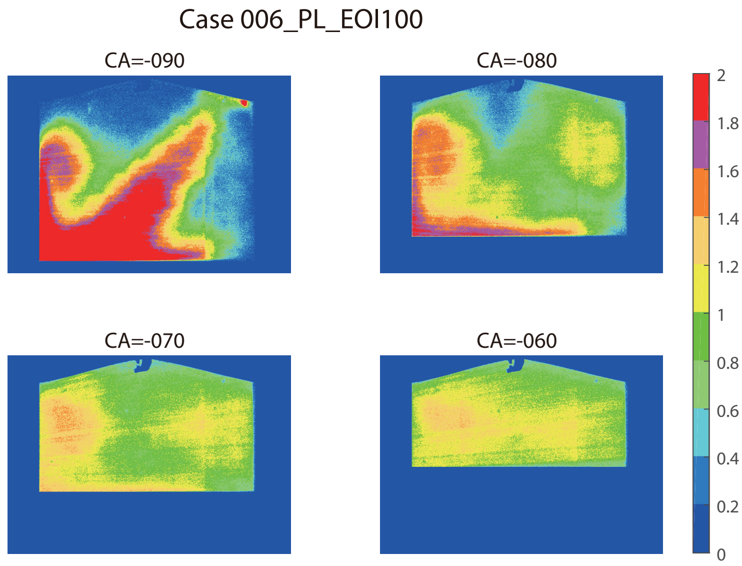

Figure 4.16: Equivalence ratio without correction in case 006_PL_EOI100

4.4.3 Reflection correction

In theory, the PLIF intensity in motored condition is uniform due to the uniform mixing between the natural gas and air. However, because of the reflection of the glass liner, more reflected light concentrates in the central zone, which results in a high fuel concentration in the central zone in fired condition after calibration.

In order to solve this problem, a scale factor matrix is established by dividing the PLIF intensity matrix by its average intensity. The scale factor matrix illustrates the relationship between PLIF intensity of each pixel and the average intensity.

$$factor_{scale_{pixel}} = \frac{Intensity_{Motored_{pixel}}}{Intensity_{Average}} \tag{4.23}$$

In order to reduce the influence of noise, the final scale factor matrix is the average of the matrices of a part of the cases in motored condition. The Table 4.11 shows the correlation between scale factor matrices of different cases. Because the cases 012_PL_PFI and 013_PL_PFI have high signal-to-noise ratio (SNR), leading to low correlations. In addition, the Table 4.12 shows the correlation between the scale factor matrices of different CAs positions, the cases 012_PL_PFI and 013_PL_PFI also have low correlation. Therefore, the scale factor matrices of the cases 012_PL_PFI and 013_PL_PFI do not participate in the scale factor matrix calculation. Furthermore, the PLIF image zone of CA050 are different to the other three CAs, the cases in CA050 also do not participate in this calculation.

$$factor_{scale} = mean\left(\sum_{CA}\sum_{Cases} factor_{Scalei}\right) \tag{4.24}$$

CA050	Case 007	Case 008	Case 009	Case 010	Case 011	Case 012	Case 013
Case 007	1	0.9863	0.9803	0.9916	0.9926	0.797	0.95
Case 008		1	0.9767	0.9881	0.989	0.7949	0.9465
Case 009			1	0.9821	0.9831	0.7892	0.9408
Case 010				1	0.9949	0.7986	0.9519
Case 011					1	0.7997	0.9530
Case 012						1	0.7638
Case 013							1

CA100	Case 007	Case 008	Case 009	Case 010	Case 011	Case 012	Case 013
Case 007	1	0.9753	0.96605	0.9859	0.9877	0.6728	0.9134
Case 008		1	0.9532	0.9783	0.9802	0.6680	0.9061
Case 009			1	0.9637	0.9656	0.6579	0.8927
Case 010				1	0.9912	0.6751	0.9164
Case 011					1	0.6765	0.9181
Case 012						1	0.6261
Case 013							1

CA150	Case 007	Case 008	Case 009	Case 010	Case 011	Case 012	Case 013
Case 007	1	0.9692	0.9494	0.9821	0.9851	0.6297	0.8927
Case 008		1	0.9405	0.9729	0.9759	0.6244	0.8841
Case 009			1	0.9533	0.9565	0.6107	0.8668
Case 010				1	0.9889	0.6321	0.8962
Case 011					1	0.6353	0.8990
Case 012						1	0.5752
Case 013							1

CA180	Case 007	Case 008	Case 009	Case 010	Case 011	Case 012	Case 013
Case 007	1	0.9687	0.9487	0.9826	0.9850	0.6157	0.8851
Case 008		1	0.9388	0.9723	0.9746	0.6093	0.8757
Case 009			1	0.9524	0.9546	0.5973	0.8582
Case 010				1	0.9888	0.6184	0.8885
Case 011					1	0.6195	0.8909
Case 012						1	0.5588
Case 013							1

Table 4.11: The correlation of scale factor matrix for cases

Where, CA = 100, 150 and 180, and $Cases$ = 007, 008, 009, 010 and 011.

Case 011	CA100	CA 150	CA 180
CA 100	1	0.9917	0.9914
CA 150		1	0.9915
CA 180			1

Case 010	CA100	CA 150	CA 180
CA 100	1	0.9868	0.9871
CA 150		1	0.9859
CA 180			1

Case 007	CA100	CA 150	CA 180
CA 100	1	0.9800	0.9803
CA 150		1	0.9786
CA 180			1

Case 008	CA100	CA 150	CA 180
CA 100	1	0.9635	0.9624
CA 150		1	0.9590
CA 180			1

Case 009	CA100	CA 150	CA 180
CA 100	1	0.9299	0.9284
CA 150		1	0.9203
CA 180			1

Case 013	CA100	CA 150	CA 180
CA 100	1	0.8315	0.8236
CA 150		1	0.8076
CA 180			1

Case 012	CA100	CA 150	CA 180
CA 100	1	0.4338	0.4259
CA 150		1	0.3988
CA 180			1

Table 4.12: The correlation of scale factor matrix for CA positions

During the calibration, for each pixel, the corrected intensity can be obtained by dividing the PLIF intensity by the scale factor with the same pixel position. Using the Equation (4.25), it can lower the intensity in the central zone, and increase the intensity in the periphery zone, where to eliminate the influence of reflection by the glass liner.

$$Intensity_{pixel_{corrected}} = \frac{Intensity_{pixel_{fired}}}{factor_{scale_{pixel}}} \tag{4.25}$$

After the reflection-correction of PLIF intensity, the next step is that to calibrate equivalence ratio using the Equation (4.22). Because this method ignored the influence of pressure and temperature, the Equation (4.22) is suitable for all CA positions in fired condition. The equivalence ratio maps in fired conditions calibrated by the indirect pixel by pixel calibration are shown in the Appendix C.3 (Equivalence ratio maps (Reflection-Correction)).

The Figures 4.17 and 4.18 are the comparisons of the equivalence ratio results calibrated without and with reflection correction in cases 004_PL_PFI and 005_PL_EOI250. The scale factor matrix can effectively eliminate the reflection influence of the glass liner by comparing the equivalence ratio results calibrated by the two different methodologies. Moreover, in the Figure 4.19, the calibration with reflection correction can effectively correct the movement of the injected natural gas jet, the high fuel concentration zone occurs in the zone near the head of the engine.

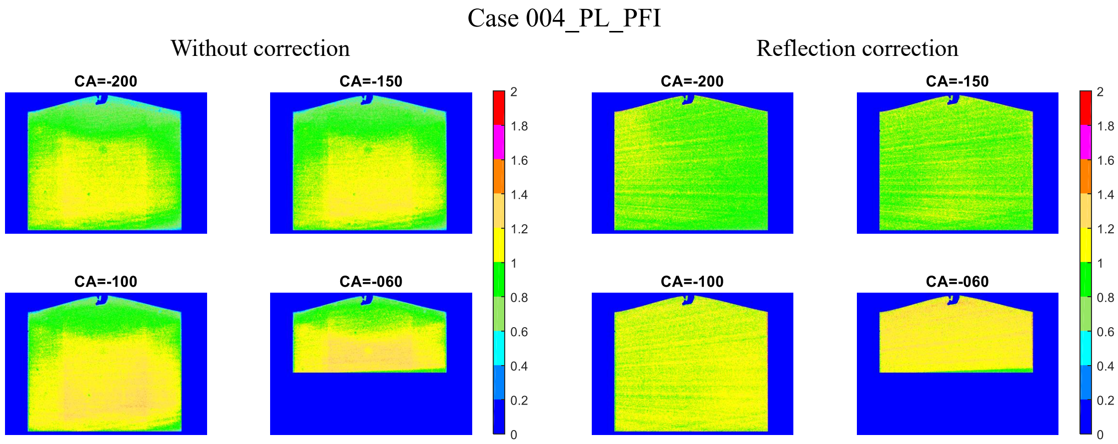

Figure 4.17: Equivalence ratio calibrated without & with reflection correction in case 004_PL_PFI

Although the calibration with reflection correction can effectively eliminate the influence of reflection of the glass liner, but equivalence ratio is greater than 1 at the end of compression stroke (with high pressure and temperature) due to not considering the influences of pressure and temperature. The Figure 4.20 shows the equivalence ratio results of 4 CA positions in the case 004_PL_PFI calibrated with reflection correction. At CA = -150, the equivalence ratio values are around 1, but when the CAs are less than 150 (CA = -100, -060, -040), the equivalence ratio values increase, this phenomenon is impossible under normal condition.

An overestimation of the equivalence ratio values at the end of compression is also present in the cases 005_PL_EOI250 and 006_PL_EOI100. Therefore, the influence of pressure and temperature cannot be negligible during the calibration of the equivalence ratio.

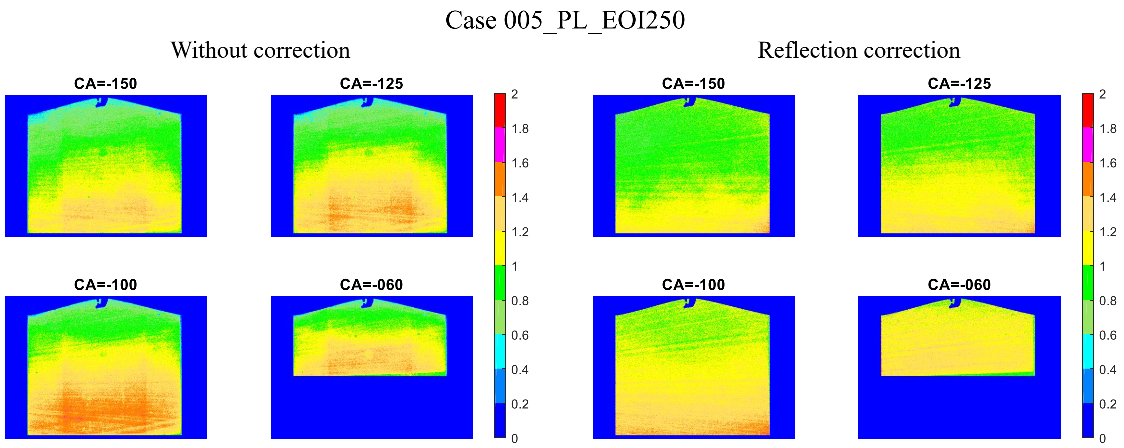

Figure 4.18: Equivalence ratio calibrated without & with reflection correction in case 005_PL_EOI250

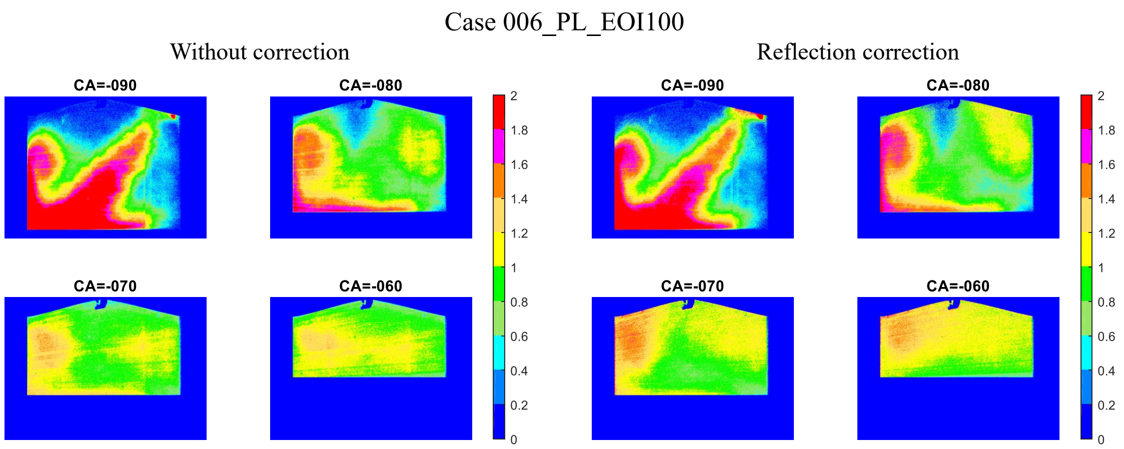

Figure 4.19: Equivalence ratio calibrated without & with reflection correction in case 006_PL_EOI100

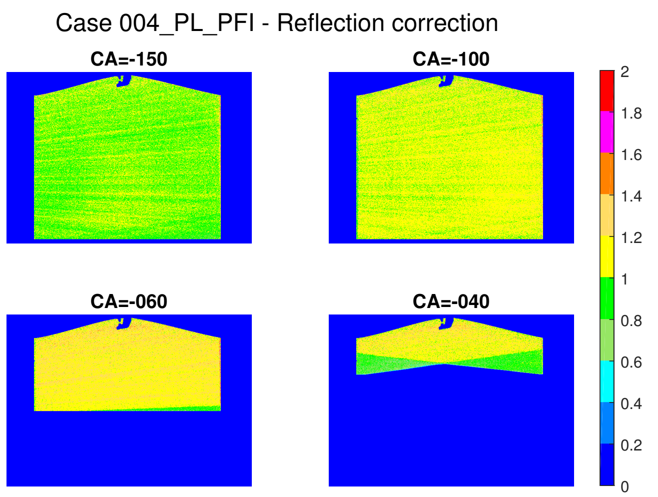

Figure 4.20: Equivalence ratio calibrated with reflection correction in case 004_PL_PFI

4.4.4 Pressure and temperature correction

In the Subsection 4.4.1, the average PLIF intensities in CA050 have a decline due to the shadows of the piston. In order to analyze the variation of the PLIF intensity along the crank angle (or pressure and temperature), the average PLIF intensity must be calculated in the same zone for all 4 CA positions. Therefore, the Upper zone is a zone to analyze the variation of the PLIF intensity for the CAs, the Figure 4.21 shows the Upper zone in the PLIF image of part load operation.

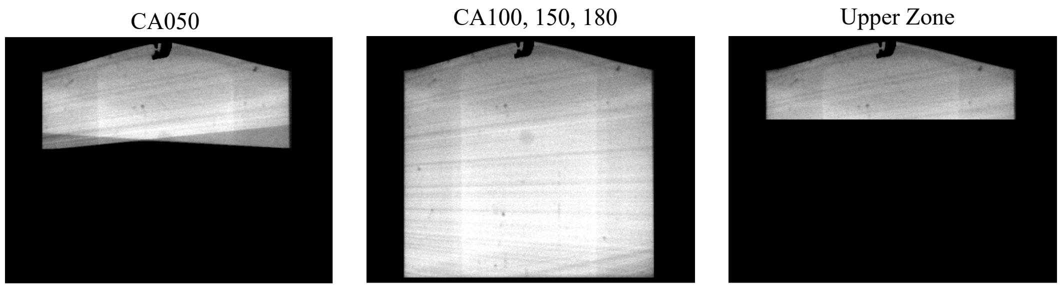

Figure 4.21: Upper zone in PLIF image of part load operation

The Figure 4.22 shows the trends of the average PLIF intensities with the CAs. Lower PLIF intensity in the zone of the CA050 is not considered, therefore, the average PLIF intensities have increments with the CAs. In order to determine that the average intensities in the upper zone may represent the average PLIF intensities in the entire zone, the ratio between average intensities in upper zones and those in entire zones in CA -180, -150 and -100 are listed in the Table 4.1. The mean value is 0.7592, and the CoV of the ratio values is 1.53%, which can deduce that the average PLIF intensity in the upper zone of CA050 is about 0.76 of the average PLIF intensity of the virtual entire zone (entire zone of CA180, 150 and 100).

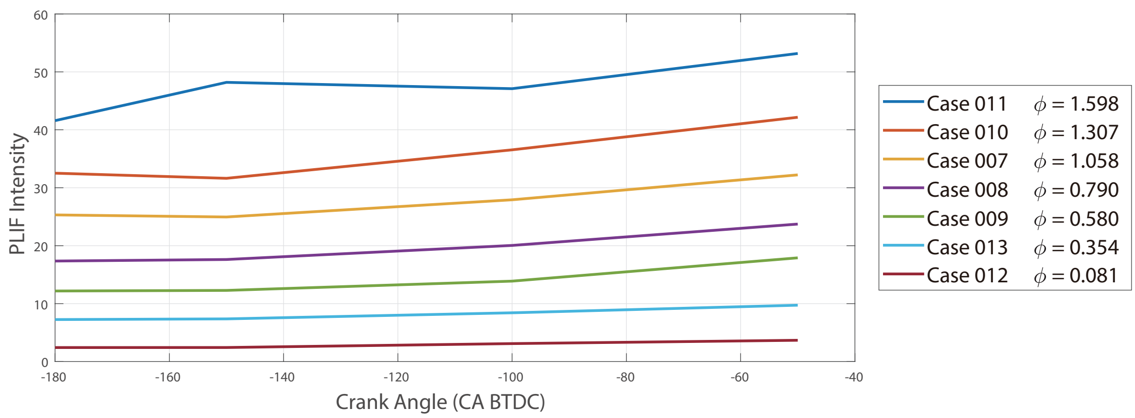

Figure 4.22: The trends of the average PLIF intensities in Upper zone with CAs

A semi-empirical model is established to determine the influence of pressure and temperature at the PLIF intensity, the model is as follows:

	Intensity Upper zone/Entire zone		
Case	CA100	CA150	CA180
Case 011	0.74825	0.77882	0.75612
Case 010	0.74764	0.75321	0.75877
Case 007	0.74827	0.75647	0.75748
Case 008	0.75790	0.75284	0.75780
Case 009	0.75050	0.76289	0.76440
Case 013	0.76000	0.75538	0.77859
Case 012	0.78837	0.73963	0.76885

Table 4.13: The ratio of average intensities in upper zone and in entire zone

$$I_{predi.} = I_{CA180} \cdot \left[1 + k_p \cdot (p - p_{CA180}) + k_T \cdot \left(\frac{T - T_{CA180}}{100}\right)\right] \tag{4.26}$$

Where:
k_p: the rate coefficient of pressure
k_T: the rate coefficient of temperature

Using the least squares method, and a transformation of the equation (4.26) of the semi-empirical model, the rate coefficients can be found.

$$\frac{I_i - I_{CA180}}{I_{CA180}} = k_{CA180} - 1 = k_p \cdot (p - p_{CA180}) + k_T \cdot \left(\frac{T - T_{CA180}}{100}\right) \tag{4.27}$$

Where the subscript i is corresponding to the values of CA150, 100 and 050, the average intensities are the mean values of PLIF intensity in the Upper zone, and the pressures and temperatures are the results of the TPA model in the Section 3.5.

The results of rate coefficients and the coefficient of determination (R^2) are shown in the Table 4.14. Furthermore, the predicted average PLIF intensities plot in the Figure 4.23, because the coefficient of determination is not too high, the difference between the experimental and estimated values is great when the pressure and temperature are high (CA = -050).

k_T	0.4470
k_p	-0.2148
R^2	91.12%

Table 4.14: The rate coefficients of the semi-empirical model in part load operation

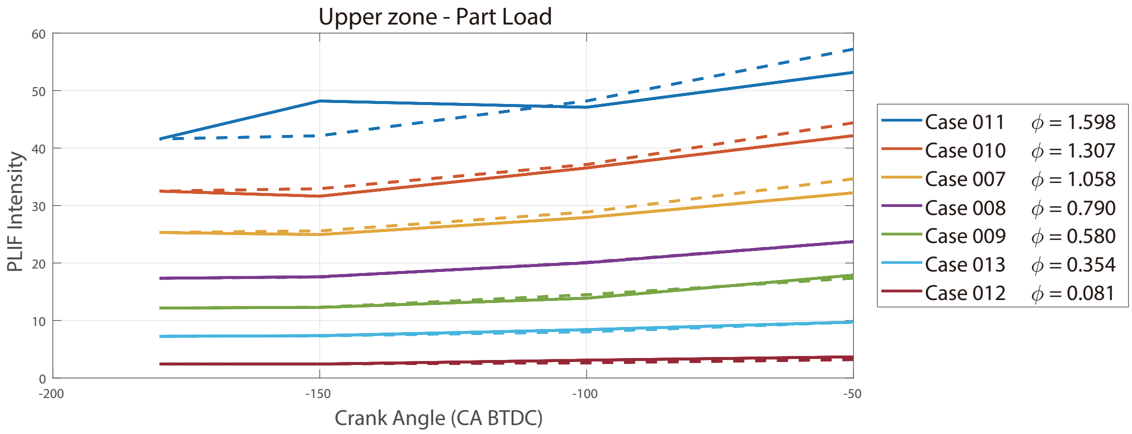

Figure 4.23: The experimental average intensities (solid lines) e predicted PLIF intensities (dotted lines) of part load operation

Using the Equation (4.26) of semi-empirical model and the rate coefficients of k_T and k_p of part load operation, the PLIF intensity can be corrected in the condition of CA = 180 where the pressure is 0.31 bar and the temperature is 340 K.

The Figure 4.10 is shown the distribution of the CAs for the PLIF images and the corresponding pressures and temperatures in motored and fired conditions. Due to the different types of natural gas injection, there are differences in pressure and temperature between fired and motored conditions. The Table 4.15 shows the pressure and temperature ranges in motored and fired conditions.

Parameter	Motored condition	Fired condition
Pressure [bar]	0.3 ~2.2	0.7 ~4.5
Temperature [K]	340 ~510	360 ~570

Table 4.15: The rate coefficients of the semi-empirical model in part load operation

The rate coefficients (k_p and k_T) in the Table 4.15 can predict the PLIF intensity in the pressure lower than 2.2 bar and temperature less than 500 K. But for the high pressure and temperature, these two rate coefficients cannot predict the PLIF intensity, because the fluorescence characteristic of the tracer may be different in high pressure and/or temperature. The Table 4.16 lists the CAs in which the pressure is greater than 2 bar and/or the temperature higher than 500 K.

The degree of mixing before the ignition is significant for the engine performance. Thus, the calibration accuracy of the equivalence ratio in the last CAs (CA 060, 050 and 040) is important. In order to determine the rate coefficients at high pressure and temperature, the behavior of the PLIF intensity in full load operation should play an important role.

Case	CA	Pressure [bar]	Temperature [K]
Case 004	-060	2.298	488.11
	-050	4.164	566.57
Case 005	-060	2.458	490.56
	-050	4.506	569.33
	-070	1.978	468.80
Case 005	-060	2.494	498.70
	-050	3.281	534.98
	-040	4.508	578.04

Table 4.16: The CAs for pressure higher than 2 bar and/or temperature higher than 500 K

Due to the late closing of the intake valve, at the crank angle 180 BTDC, the intake valve is still open, therefore, in the PLIF image, the intake valve covers a part of the PLIF zone. A Central zone is chosen to analyze the variation of the average PLIF intensities with the pressure and temperature. The Figure 4.24 shows the Central zone in the PLIF image of full load operation.

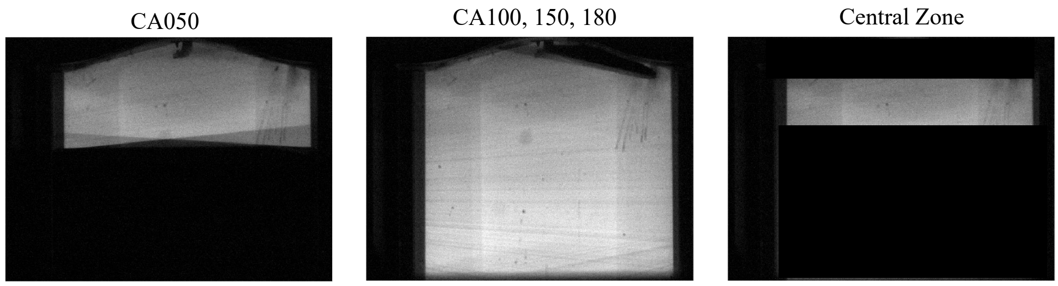

Figure 4.24: Central zone in PLIF image of full load operation

The engine temperature of full load operation in motored conditions can be simulated by the GT-Power model, the model is validated by calibrating the measured signals in the case 024_FL_SOI-350. With the same methodology, the rate coefficients of pressure and temperature can be found and are listed in the Table 4.17. And the Figure 4.25 shows the experimental average PLIF intensity and predicted PLIF intensity in the Central zone of full load operation. Furthermore, the CoV of ratio of the PLIF intensity between the Central zone and the entire zone is 1.193%, which means that the PLIF intensities in central zones can represent the intensity in entire areas.

Using the Equation 4.26 and the rate coefficients k_p and k_T of full load operation, the PLIF intensity can be corrected in the condition of CA = 180 of full operation

k_{T_FL}	0.12790
k_{p_FL}	-0.0265
R^2	75.54%

Table 4.17: The rate coefficients of the semi-empirical model in full load operation

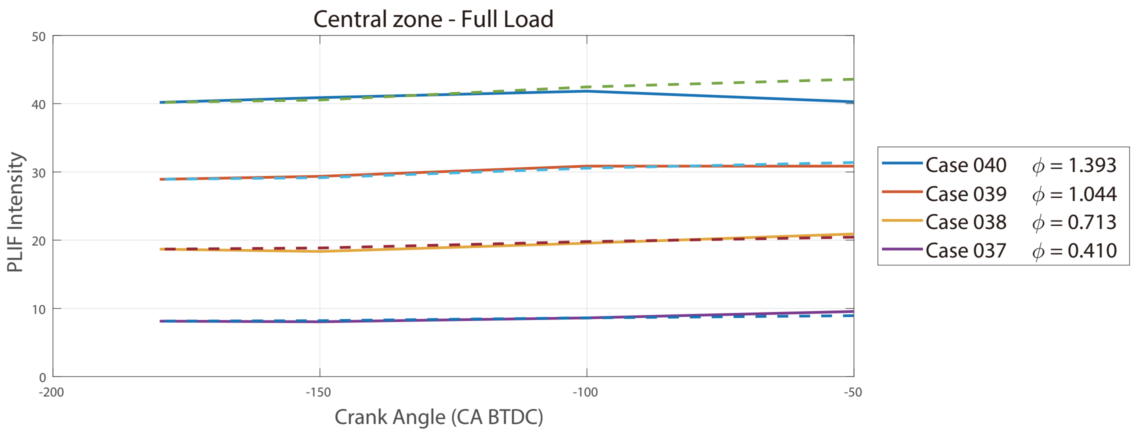

Figure 4.25: The experimental average intensities (solid lines) e predicted PLIF intensities (dotted lines) of full load operation

where the pressure is 2.23 bar and the temperature is 432 K. Then, the corrected PLIF intensity of full load operation can be corrected in the condition of part load operation by the Equation (4.26) and the pressure and temperatures in CA = 180 of part load operation (p = 0.31 bar, T = 340 K).

- For low pressure and temperature ($k_{CA180} - PL$):

  $k_{CA180} = 1 + k_p \cdot (p - p_{CA180}) + k_T \cdot \left(\frac{T - T_{CA180}}{100}\right)$

  $p_{CA180} = 0.31bar; T_{CA180} = 340K$

- For high pressure and temperature (in the Table 4.16) ($k_{CA180} - PL + FL$):

  $k_{CA180\_FL} = 1 + k_{p\_FL} \cdot (p - p_{CA180\_FL}) + k_{T\_FL} \cdot \left(\frac{T - T_{CA180\_FL}}{100}\right)$

  $p_{CA180_{FL}} = 2.23bar; T_{CA180_{FL}} = 432K$

  $k_{CA180} = k_{CA180\_FL} \cdot \left[1 + k_p \cdot (p - p_{CA180}) + k_T \cdot \left(\frac{T - T_{CA180}}{100}\right)\right]$

The Figures 4.26, 4,27 e 4,28 show the trends of pressure, temperature and the coefficients of CA180 calculated in the PL and PL+FL. At high pressure and temperature, an increase of coefficient of k_{CA180} lowers the PLIF intensity. Therefore, the p and T corrected PLIF intensities can be calculated by the Equation (4.28):

$$I_{p\&Tcorr} = \frac{I_{fired}}{k_{CA180}} \tag{4.28}$$

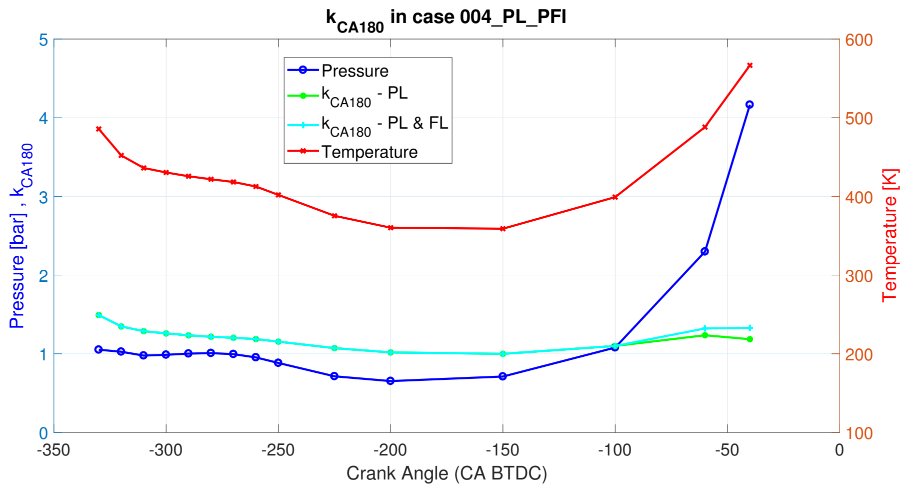

Figure 4.26: The coefficient of CA180 in case 004_PL_PFI

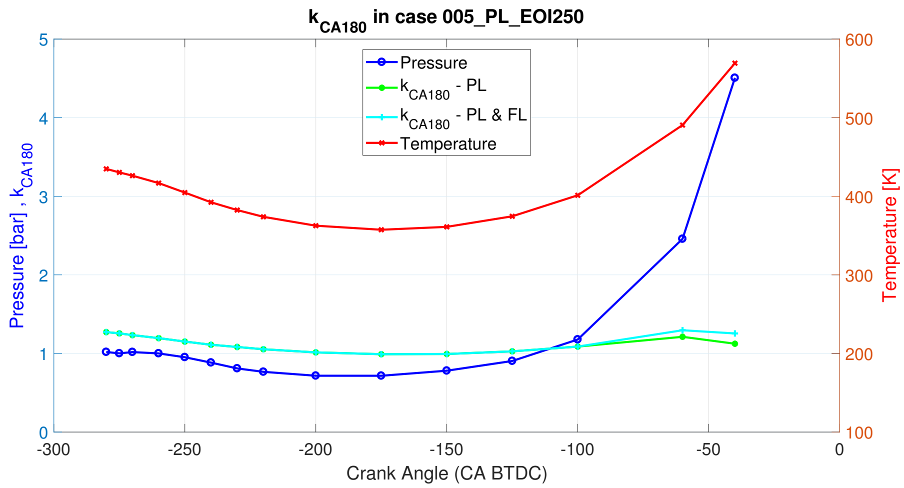

Figure 4.27: The coefficient of CA180 in case 005_PL_EOI250

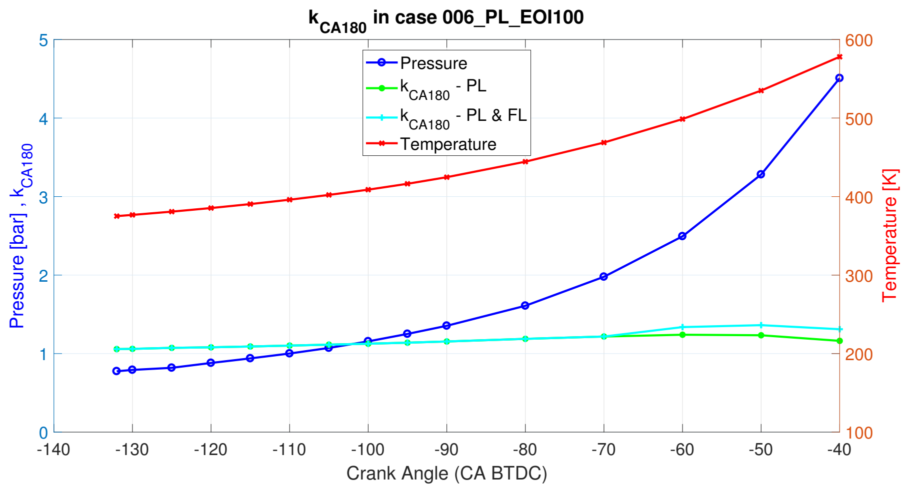

Figure 4.28: The coefficient of CA180 in case 006_PL_EOI100

Because the reference is the engine condition of CA180, therefore, the calibration curve is not curve fitting of all the PLIF intensity of part load operation in motored condition, instead it is the fitting curve of PLIF intensities of CA180, the equation of curve fitting is as follows, and the coefficient of determination R^2 is 99.95%.

$$Intensity = 7.3336 \cdot \phi^2 + 22.3382 \cdot \phi + 0.9974 \tag{4.29}$$

Using the coefficient of k_{CA180} and the calibration equation (4.28), the results of equivalence ratio can be obtained, in the Appendix C.5 shows the results of equivalence ratio maps of cases in fired condition by calibrating with p & T correction. Furthermore, the Figures 4.28, 4.29 and 4.30 show the last 4 equivalence ratio images of each case by calibrating without (reflection correction) and with p & T correction. Because k_{CA180} lowers intensities at high pressure and temperature, the equivalence ratio tends to stoichiometric value.

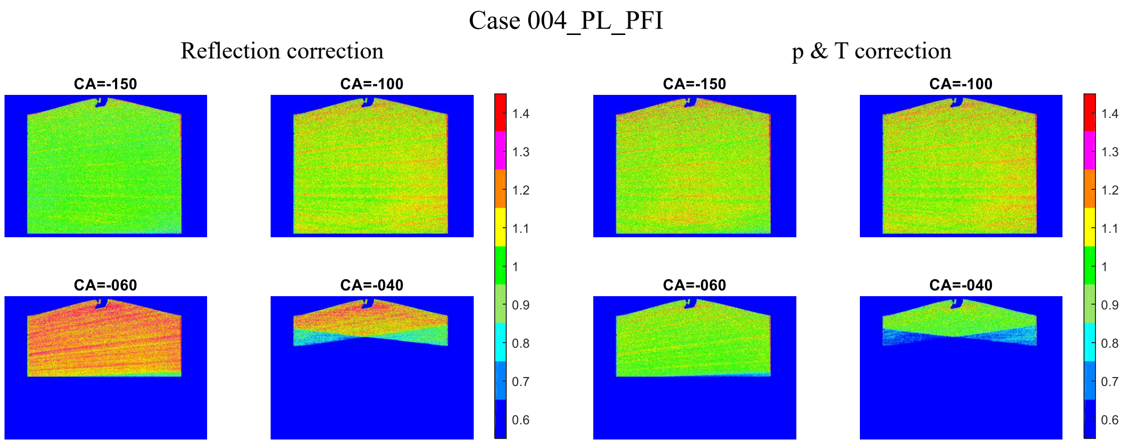

Figure 4.29: Equivalence ratio images in case 004_PL_PFI

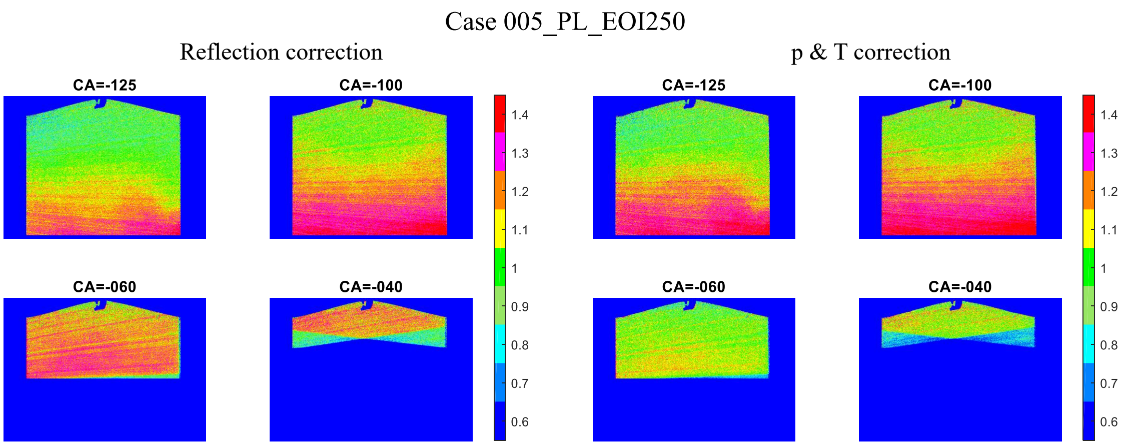

Figure 4.30: Equivalence ratio images in case 005_PL_EOI250

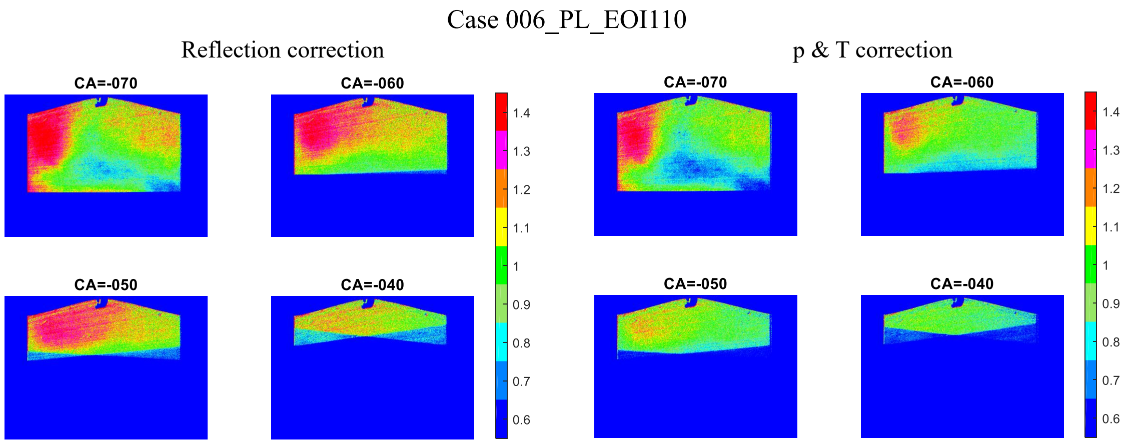

Figure 4.31: Equivalence ratio images in case 006_PL_EOI100

Chapter 5

Conclusion

The present work aimed at analyzing the mixing process in a direct injection natural gas engine, through the experimental investigations with the PLIF techniques and data post-processing optimization. This work started from the original experimental database and a 3-cylinder engine GT-power model, which results in the heavy works faced. The work is composed of two parts, including numerical simulation and PLIF investigation. For both of them, the first step is the experimental data processing, which contains the extraction of experimental data from the experimental database and the verification of the validation of the extracted experimental data; the second step is the calibration, which contains the calibration of the single-cylinder engine TPA model and the calibration of the equivalence ratio with the different corrections.

The first part of the work is focused on the numerical simulation of the mixture temperature in the engine cylinder with the help of the TPA approach of GT-Power. The first step is the experimental data processing, the input data of GT-Power SCE model is obtained by the processing and analyzing the original experimental data, in which the air flow rate is calculated from the duration of injection and the experimental data of the Delphi injector due to the failure of the air flow rate sensor. The second step of the numerical simulation is the calibration of the TPA model by calibrating the air flow rate and the engine cylinder pressure. Since the single-cylinder engine is not a conventional one, the convection multiplier is higher than the default value.

- The simulated results can be coincident with the experimental results using the engine parameters Modifired_1, under the condition that the engine head, cylinder and piston temperature are default temperatures. And from the results of TPA simulation, it can be deduced that the case 004_PL_PFI is the worst case in all three cases in fired condition;

- Although the simulated results can be better matched with the experimental results, specifically on the cylinder pressure during compression stroke and on the air flow rate. However, a problem is neglected in the calibration processing, which is the exhaust port pressure higher than the engine cylinder pressure in the exhaust stroke, which is mentioned in the Subsection 3.27. This error contributed a part of error of the simultaneous results in the TPA simulation;

- There is a significant interstice between the piston and cylinder in the single-cylinder transparent engine. Due to restriction of software, the blow-by cannot be analyzed. This is an important parameter that influences the compression slop. In the results of the diagram LogP-logV, the simultaneous compression slop is always greater than the experimental one, even if the compression ratio has a value lower than 11. The restriction of the blow-by analysis causes a high convection multiplier value durаing the engine model calibration. Therefore, in the future work, the blow-by should be analyzed in the latest version of GT-Power software.

In the second part of the work, the main task is the post-processing of the PLIF images and the calibration of the equivalence ratio in fired condition. Therefore, the first step is the calculated equivalence ratio in motored condition by relationships established by the theory and by the curve fitting of experimental data. The second step is the post-processing of PLIF images in motored and fired conditions through the Matlab and obtained the average PLIF intensities in motored condition by the statistical analysis. The final step is that the calibration of the equivalence ratio, in the process of calibration two new methods have tried to correct the influence of reflection by the glass liner and the influence of pressure and temperature.

- The equivalence ratio results have high consistency with theoretical analysis by the calibration with reflection correction and p & T correction, especially, at the moment before ignition, the values of equivalence ratio are closed to 1;
- The semi-empirical model to quantify the pressure and temeprature inlfuences can effectively predict PLIF intensities in a certain range of pressure and temperature. However, due to the lack of references on the fluorescence characteristic of the tracer TMA at different pressures and temperatures, the rate coefficient of pressure and temperature should be verified by experimentation in the future;
- The error of equivalvence ratio results is composed of two main parts, one is the calibration method, another comes from calculating the equivalence ratio in motored condition. Because the range of experimental data for fitting is less than the data to be calculated, therefore, the values close to the two extremes may be over- or under-timated;
- In the future work, in addition to increasing the accuracy of the equivalence ratio in motored condition by more experimental data, the optimization of

the methodologie of reflection correction and p & T correction can offer more accurate results of equivalence ratio in fired condition.

Appendix A

Experimental Data Overview

In the following pages a list is given with the pressures in fired condition case 005_PL_EOI250 and 006_PL_EOI100, including intake/exhaust port pressure and cylinder pressure. And input data in motored condition cases.

A.1 Intake/Exhaust Port Temperatures

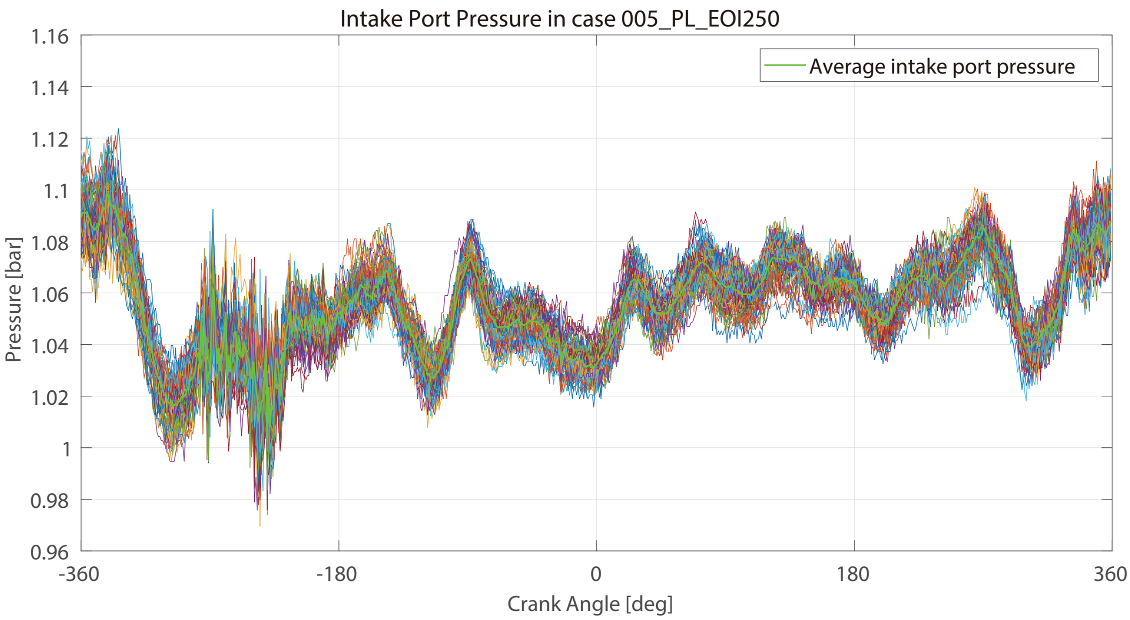

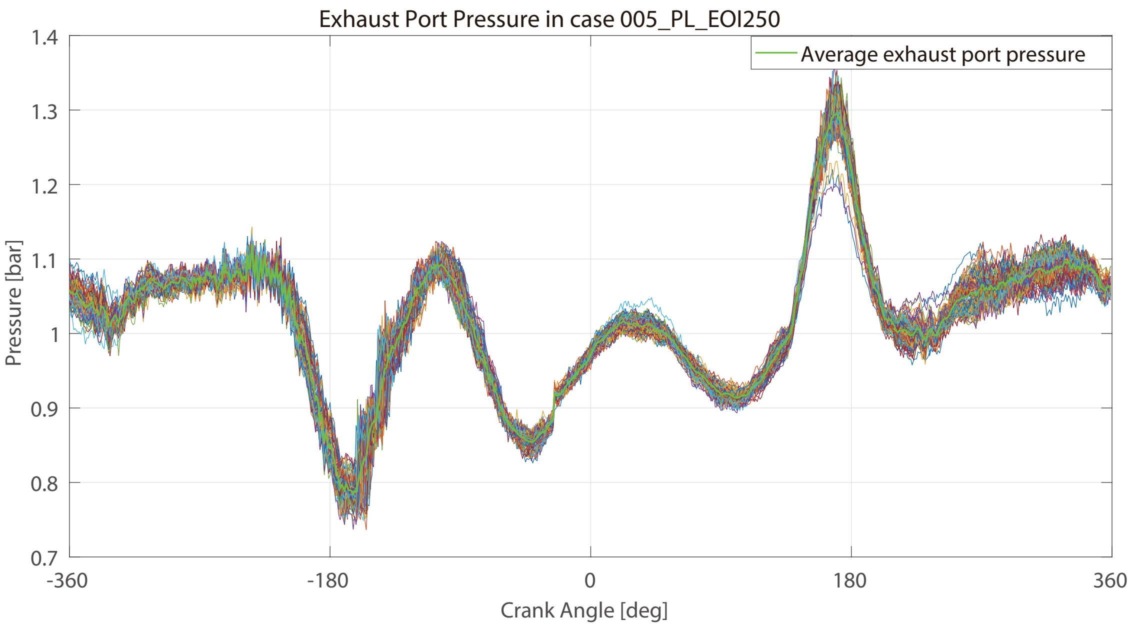

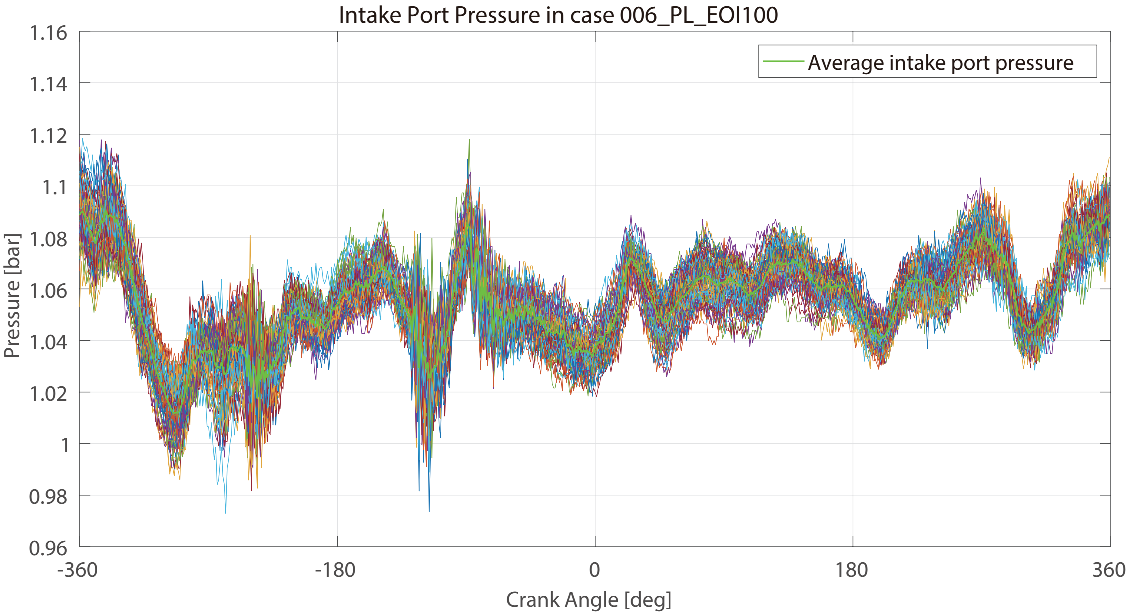
Intake Port Pressure in case 006_PL_EOI100
Average intake port pressure
Pressure [bar]
1.16
1.14
1.12
1.1
1.08
1.06
1.04
1.02
1
0.98
0.96
-360
-180
0
180
360
Crank Angle [deg]

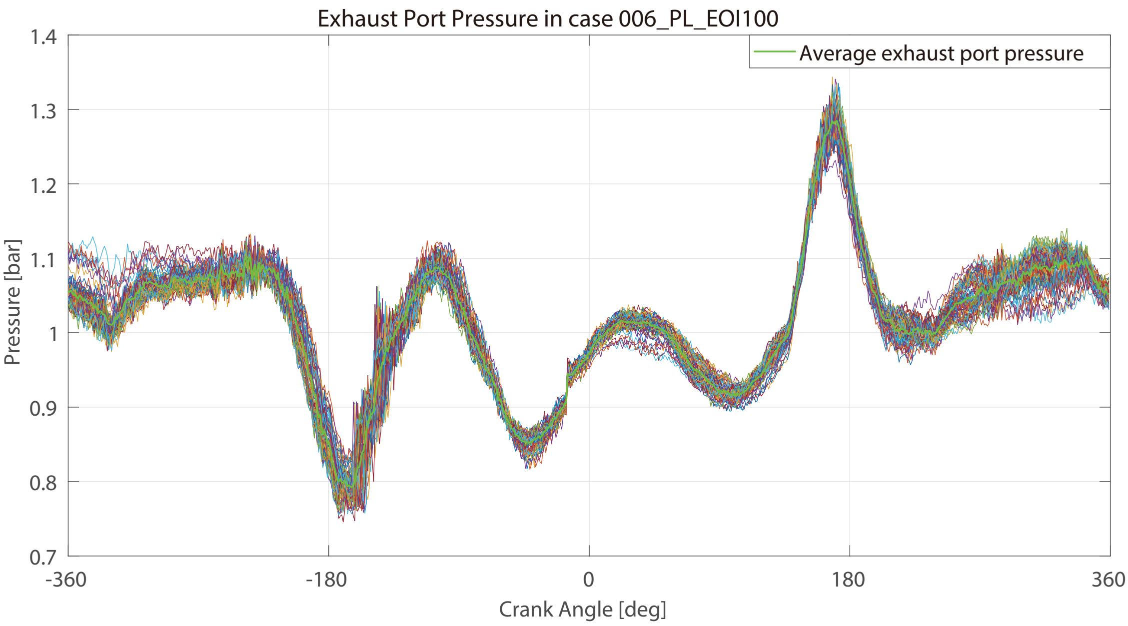
Exhaust Port Pressure in case 006_PL_EOI100
Average exhaust port pressure
Pressure [bar]
1.4
1.3
1.2
1.1
1
0.9
0.8
0.7
-360
-180
0
180
360
Crank Angle [deg]

A.2 Cylinder Pressure

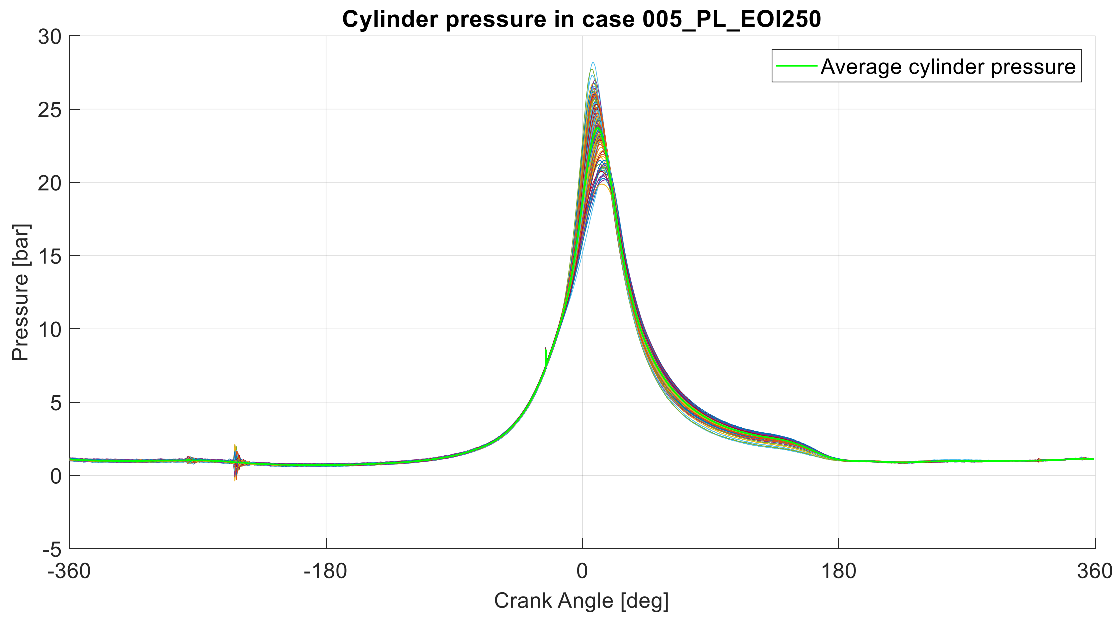

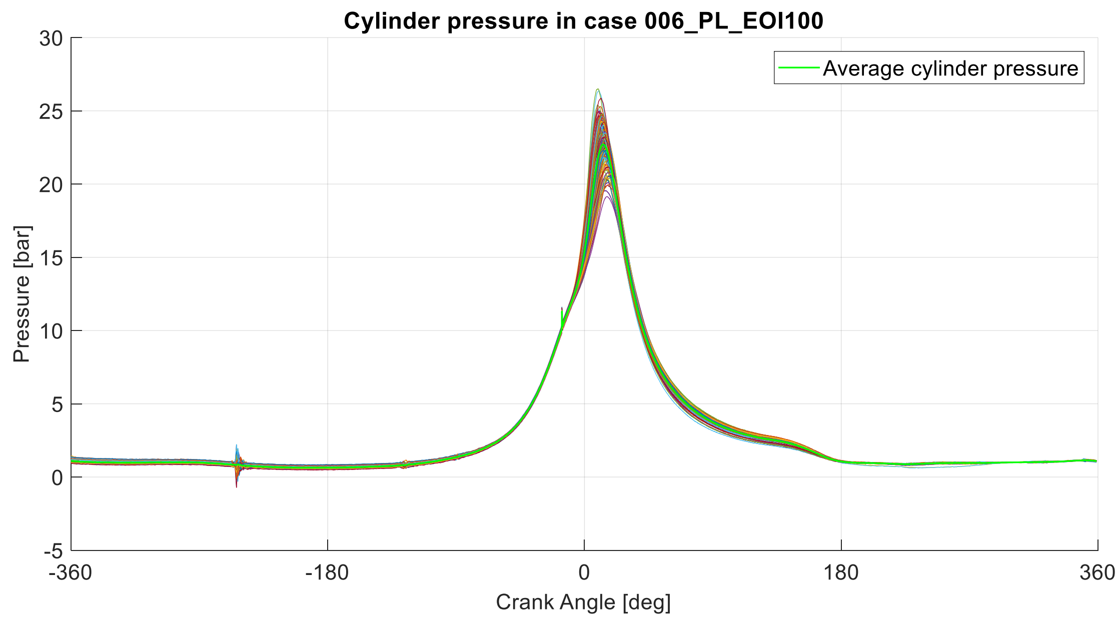

A.3 Input Data in Motored Condition

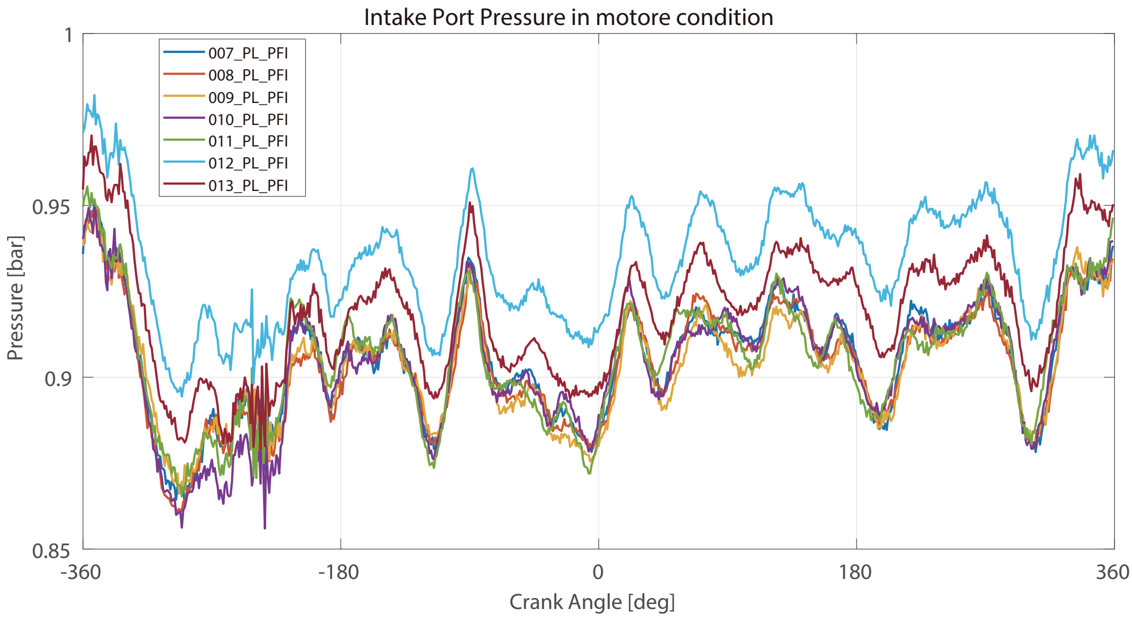

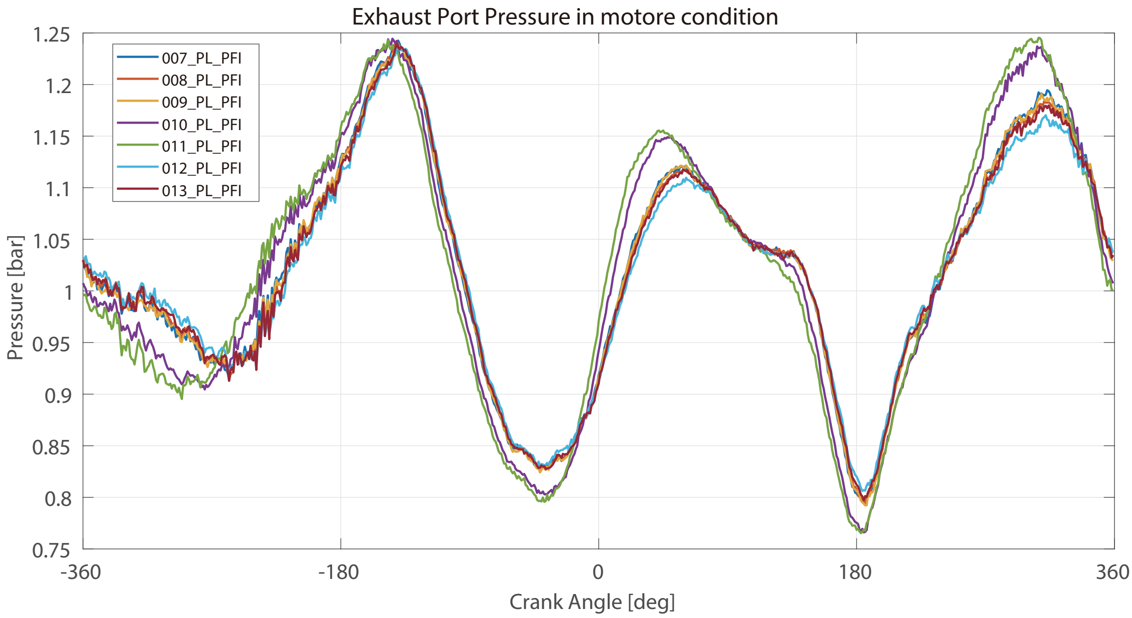

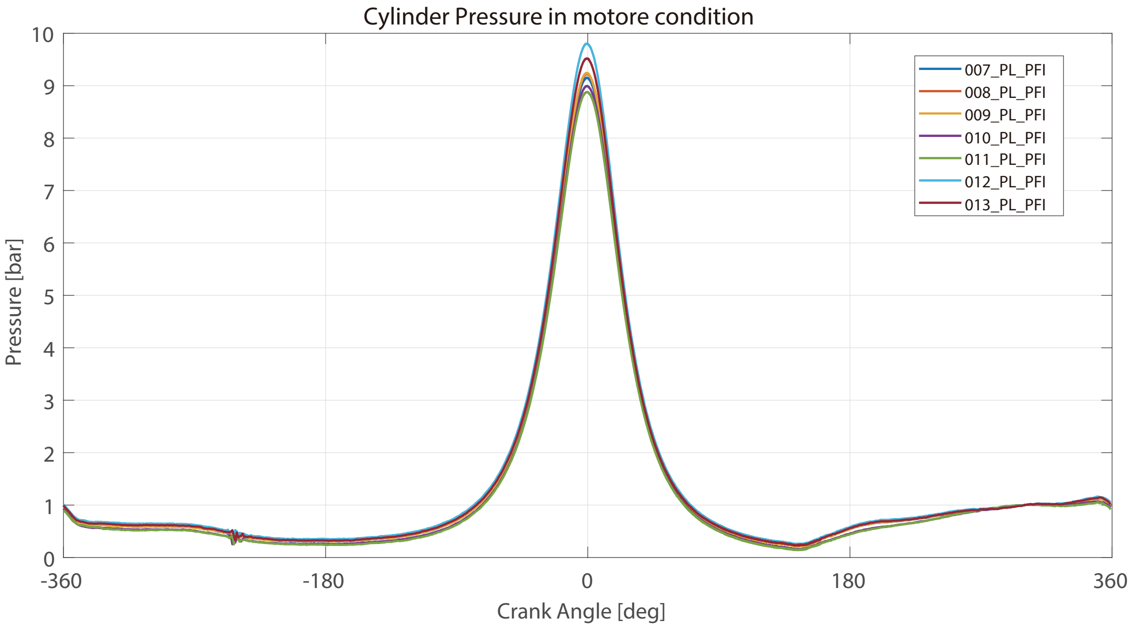

Temperatures and Lambda in motored condition

T[K]\Cases	**007**	**008**	**009**	**010**	**011**	**012**	**013**
T_Intake	308.75	308.77	308.85	308.85	309.00	309.17	309.14
T_Exhaust	339.85	339.49	340.03	338.92	338.54	339.29	338.44
T_Fuel	311.14	311.43	313.80	312.06	312.07	313.89	314.46
Lambda	0.945	1.266	1.725	0.765	0.626	12.314	2.824

Appendix B

Simulation Models Layout and Results

In the following pages a list is given with the 1.0L 3-cylinder engine model, the intake/exhaust port geometric parameters, the calibration results of TPA model and the TPA simulation results in fired condition.

B.1 Three-cylinder DING Engine Model

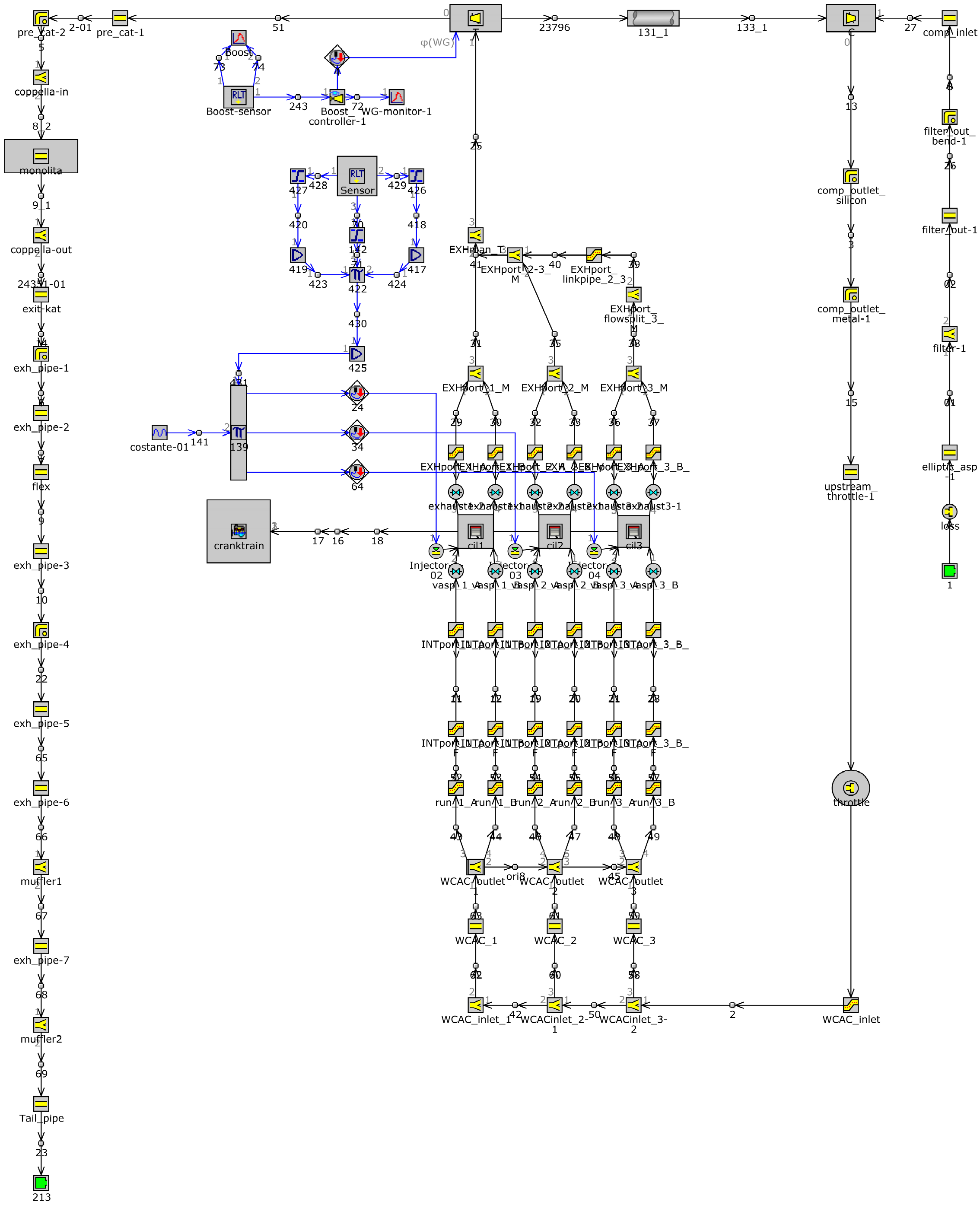

B.2 Geometric parameters of intake port

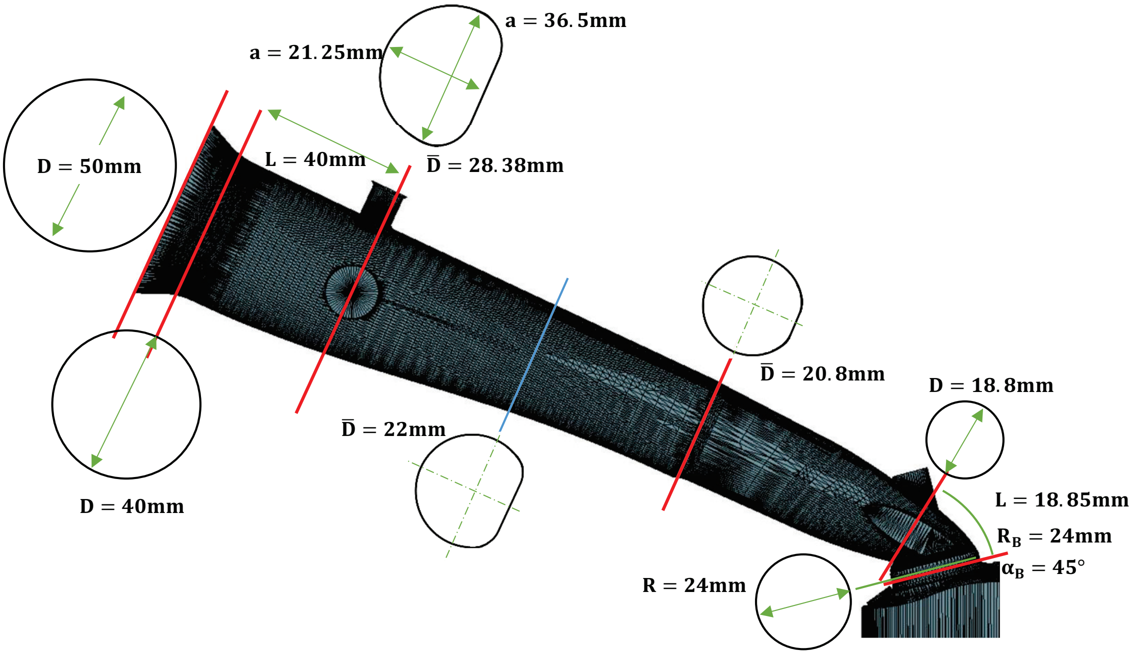

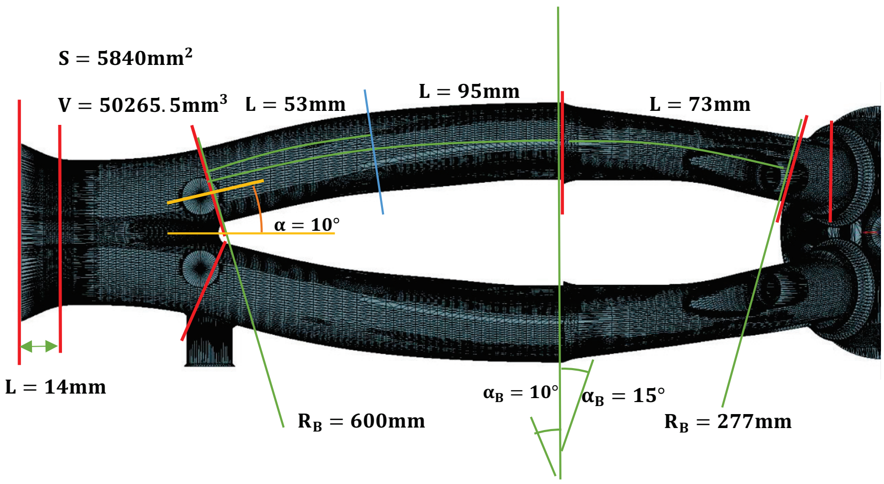

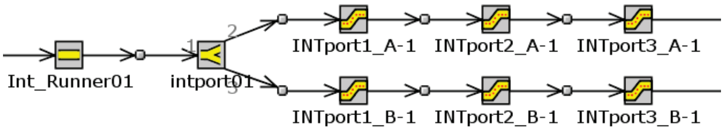

B.3 Geometric parameters of exhaust port

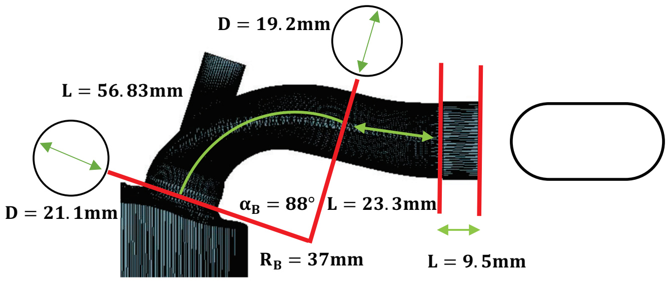

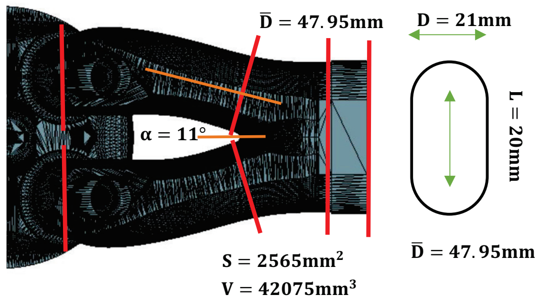

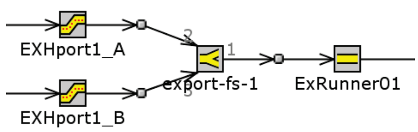

B.4 Calibration Resultas of TPA model

Comparison to Test Data

	Cyl1 (Baseline)	Cyl1 (Modified)	Cyl1 (Modified_1)
Object Name	Cyl1	Cyl1	Cyl1
Consistency Check	E,21,22	OK	OK
Air Flow [mg/cycle]	177.38	167.85	167.86
Air Flow - Test Data [mg/cycle]	164.11	164.11	164.11
Fuel Flow [mg/cycle]	10.313	9.759	9.759
Fuel Flow - Test Data [mg/cycle]	9.541	9.541	9.541
Fuel/Air Ratio	0.0581	0.0581	0.0581
Fuel/Air Ratio - Test Data	0.0581	0.0581	0.0581
Combustion Efficiency	0.998	0.998	0.998
Combustion Efficiency - Test Data	1.000	1.000	1.000
Burned Fuel Fraction	0.998	0.998	0.999
Burned Fuel Fraction - Test Data	1.000	1.000	1.000

Fuel Energy and Adjustments

	Cyl1 (Baseline)	Cyl1 (Modified)	Cyl1 (Modified_1)
Object Name	Cyl1	Cyl1	Cyl1
Consistency Check	E,12	E,12	OK
Fuel Energy (LHV) Mult. (1)	0.734	0.771	0.966
Energy Balance Ratio (2)	0.725	0.766	0.963
Fuel Energy Entering Cylinder [J]	515.64	487.93	487.96
Fuel Power Entering Cylinder [kW]	8.59	8.13	8.13
Indicated Cylinder Power [kW]	1.858	1.858	1.858
Apparent Indicated Efficiency [%]	21.62	22.85	22.85
Heat Transfer During Analysis [%]	14.93	15.30	35.21
Fraction of Fuel Injected Late (3)	0.0000	0.0000	0.0000

Engine Performance Predictions (SI)

	Performance (Baseline)	Performance (Modified)	Performance (Modified_1)
Brake Power [kW]	2.1	2.0	1.4
Brake Power [HP]	2.8	2.6	1.9
Brake Torque [N-m]	10.0	9.3	6.6
IMEP [bar]	4.62	4.35	3.35
FMEP [bar]	0.97	0.96	0.95
PMEP [bar]	-0.20	-0.21	-0.22
Air Flow Rate [kg/h]	10.6	10.1	10.1
BSAC [g/kW-h]	5064	5154	7260
Fuel Flow Rate [kg/h]	0.6	0.6	0.6
BSFC [g/kW-h]	294.4	299.7	422.1
Volumetric Efficiency [%]	43.4	41.0	41.0
Volumetric Efficiency (M) [%]	43.4	41.0	41.0
Trapping Ratio	0.999	1.000	1.000
A/F Ratio	17.20	17.20	17.20
Brake Efficiency [%]	24.5	24.0	17.1

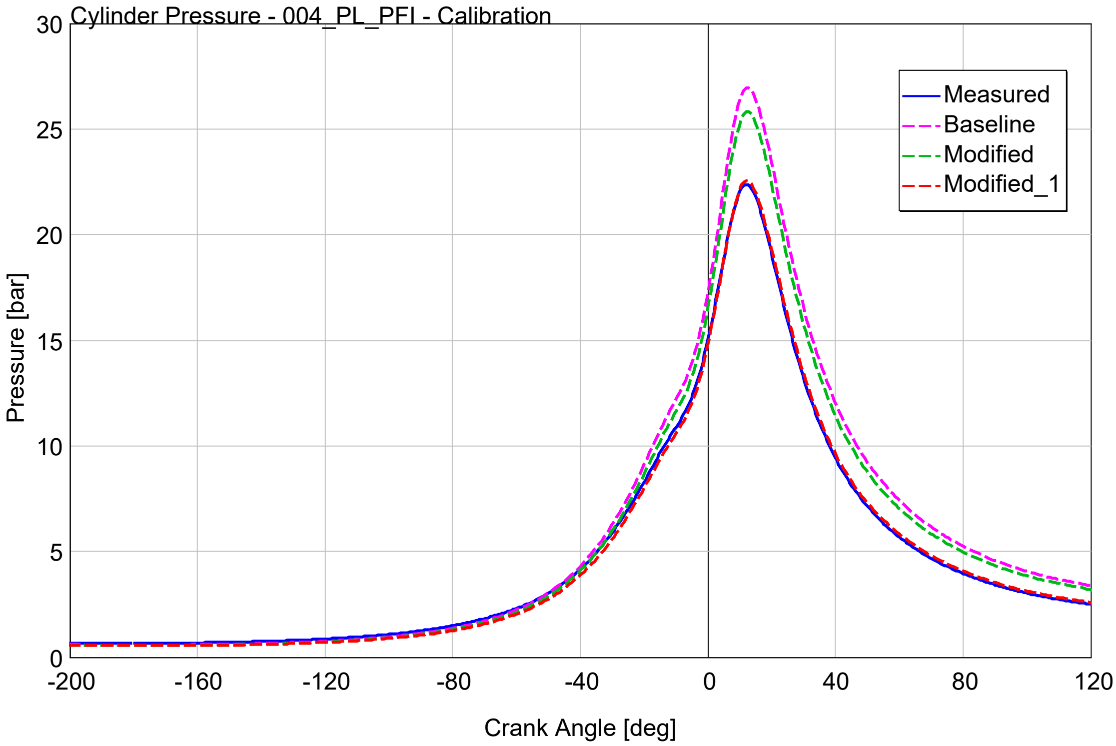
Cylinder Pressure - 004_PL_PFI - Calibration
Measured
Baseline
Modified
Modified_1
Pressure [bar]
Crank Angle [deg]
30
25
20
15
10
5
0
-200
-160
-120
-80
-40
0
40
80
120

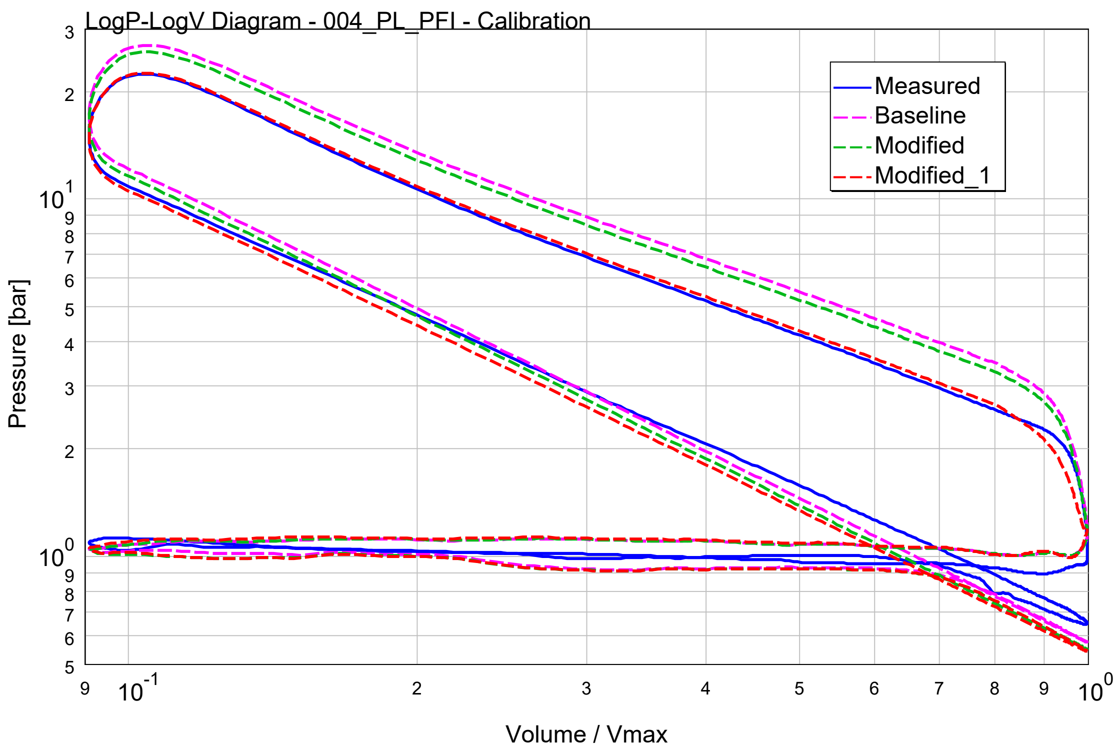
LogP-LogV Diagram - 004_PL_PFI - Calibration
Measured
Baseline
Modified
Modified_1
Pressure [bar]
Volume / Vmax
10^1
10^0
10^-1

B.5 Resultas TPA simulation: Tables

Comparison to Test Data

	Cyl1 (004_PL_PFI)	Cyl1 (005_PL_EOI250)	Cyl1 (006_PL_EOI100)
Object Name	Cyl1	Cyl1	Cyl1
Consistency Check	OK	OK	OK
Air Flow [mg/cycle]	167.86	176.37	177.56
Air Flow - Test Data [mg/cycle]	164.11	174.17	176.85
Fuel Flow [mg/cycle]	9.759	10.254	10.323
Fuel Flow - Test Data [mg/cycle]	9.541	10.126	10.282
Fuel/Air Ratio	0.0581	0.0581	0.0581
Fuel/Air Ratio - Test Data	0.0581	0.0581	0.0581
Combustion Efficiency	0.998	0.999	0.999
Combustion Efficiency - Test Data	1.000	1.000	1.000
Burned Fuel Fraction	0.999	0.999	0.999
Burned Fuel Fraction - Test Data	1.000	1.000	1.000

Fuel Energy and Adjustments

	Cyl1 (004_PL_PFI)	Cyl1 (005_PL_EOI250)	Cyl1 (006_PL_EOI100)
Object Name	Cyl1	Cyl1	Cyl1
Consistency Check	OK	OK	OK
Fuel Energy (LHV) Mult. (1)	0.966	0.993	0.984
Energy Balance Ratio (2)	0.963	0.989	0.981
Fuel Energy Entering Cylinder [J]	487.96	512.71	516.17
Fuel Power Entering Cylinder [kW]	8.13	8.55	8.60
Indicated Cylinder Power [kW]	1.858	2.024	2.033
Apparent Indicated Efficiency [%]	22.85	23.68	23.64
Heat Transfer During Analysis [%]	35.21	35.68	34.65
Fraction of Fuel Injected Late (3)	0.0000	0.0000	0.0000

Engine Performance Predictions (SI)

	Performance (004_PL_PFI)	Performance (005_PL_EOI250)	Performance (006_PL_EOI100)
Brake Power [kW]	1.4	1.5	1.5
Brake Power [HP]	1.9	2.0	2.0
Brake Torque [N-m]	6.6	7.0	7.3
IMEP [bar]	3.35	3.50	3.59
FMEP [bar]	0.95	0.95	0.95
PMEP [bar]	-0.22	-0.21	-0.23
Air Flow Rate [kg/h]	10.1	10.6	10.7
BSAC [g/kW-h]	7260	7200	6999
Fuel Flow Rate [kg/h]	0.6	0.6	0.6
BSFC [g/kW-h]	422.1	418.6	406.9
Volumetric Efficiency [%]	41.0	42.8	43.2
Volumetric Efficiency (M) [%]	41.0	42.8	43.2
Trapping Ratio	1.000	1.000	1.000
A/F Ratio	17.20	17.20	17.20
Brake Efficiency [%]	17.1	17.2	17.7

B.6 Resultas TPA simulation: Plots

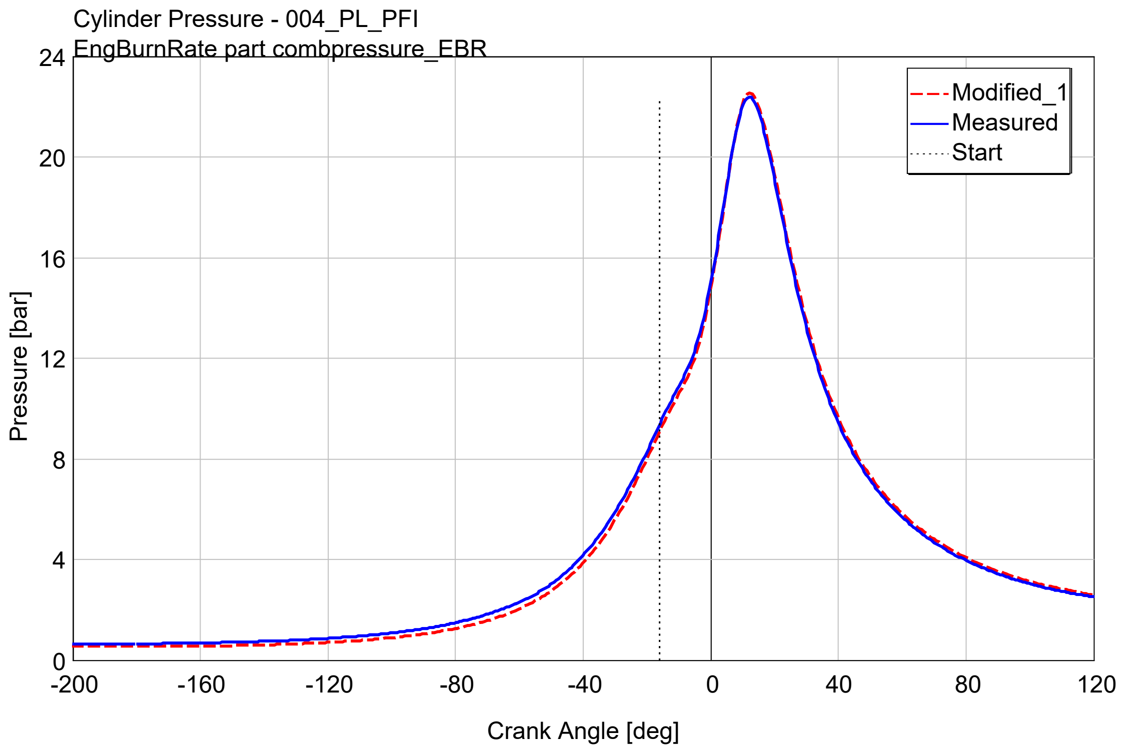

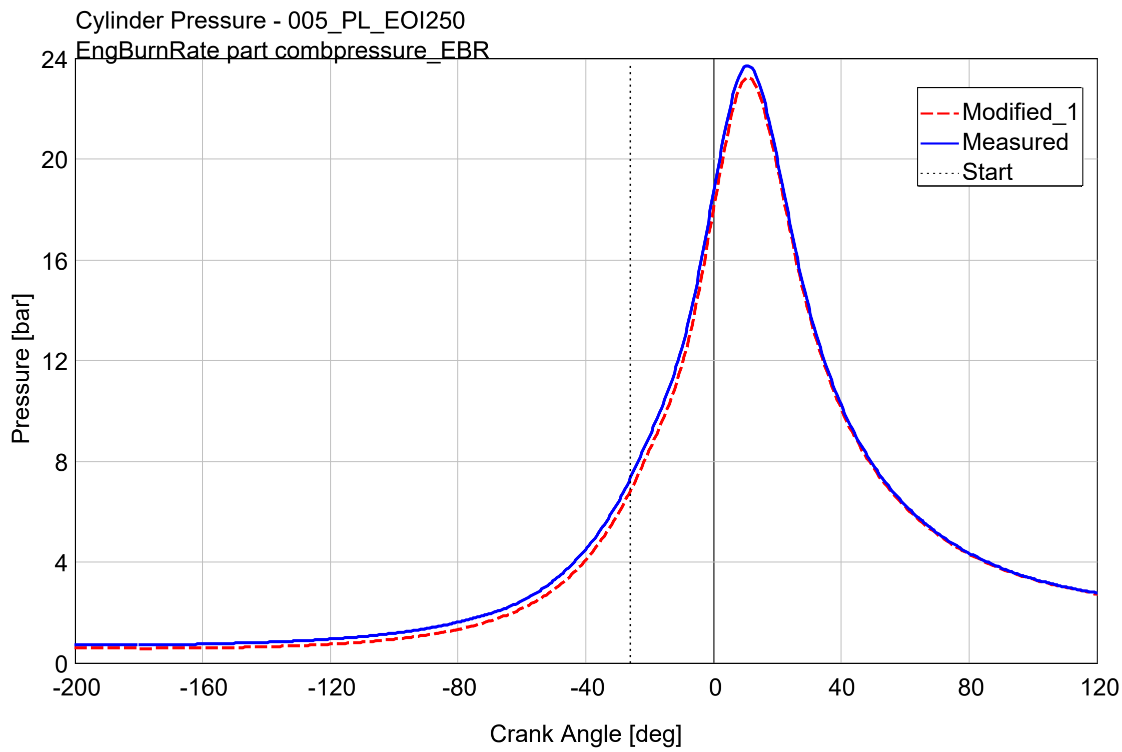

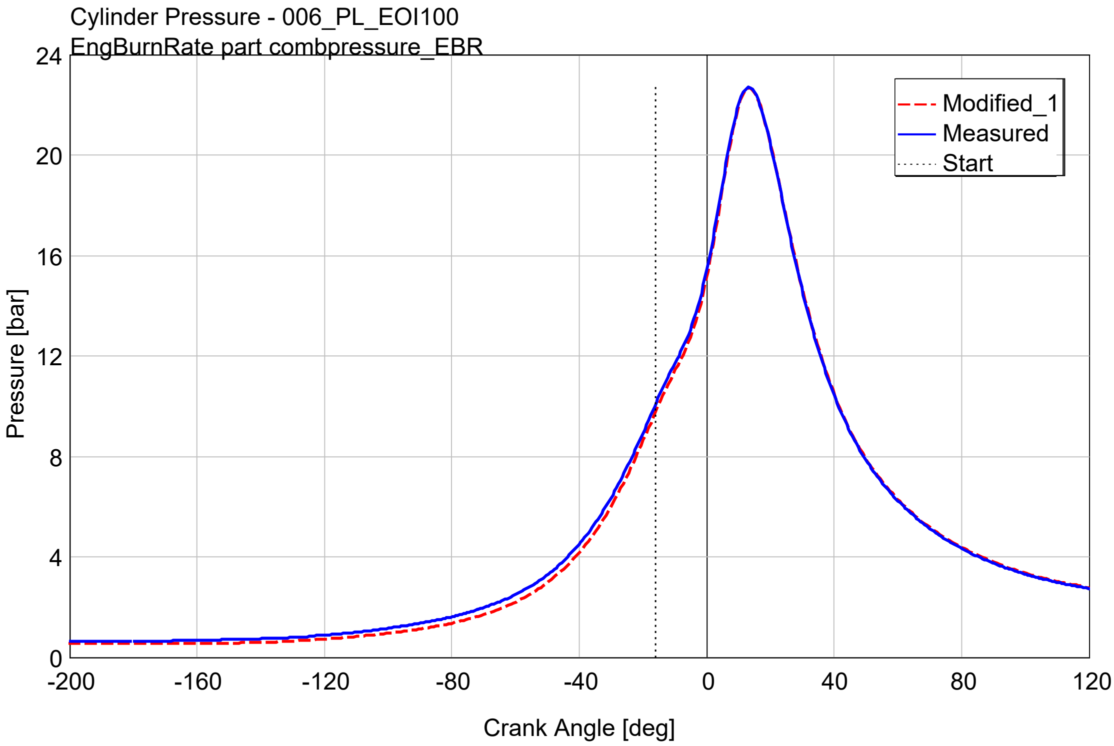
Cylinder Pressure - 006_PL_EOI100
EngBurnRate part combpressure_EBR
Modified_1
Measured
Start
Pressure [bar]
Crank Angle [deg]
24
20
16
12
8
4
0
-200
-160
-120
-80
-40
0
40
80
120

Appendix C

Various Figures in PLIF Processing

In the following pages a list is given with all the PLIF images in motored and fired condition and results of equivalence ratio map in cases of fired condition

C.1 PLIF images in motored condition

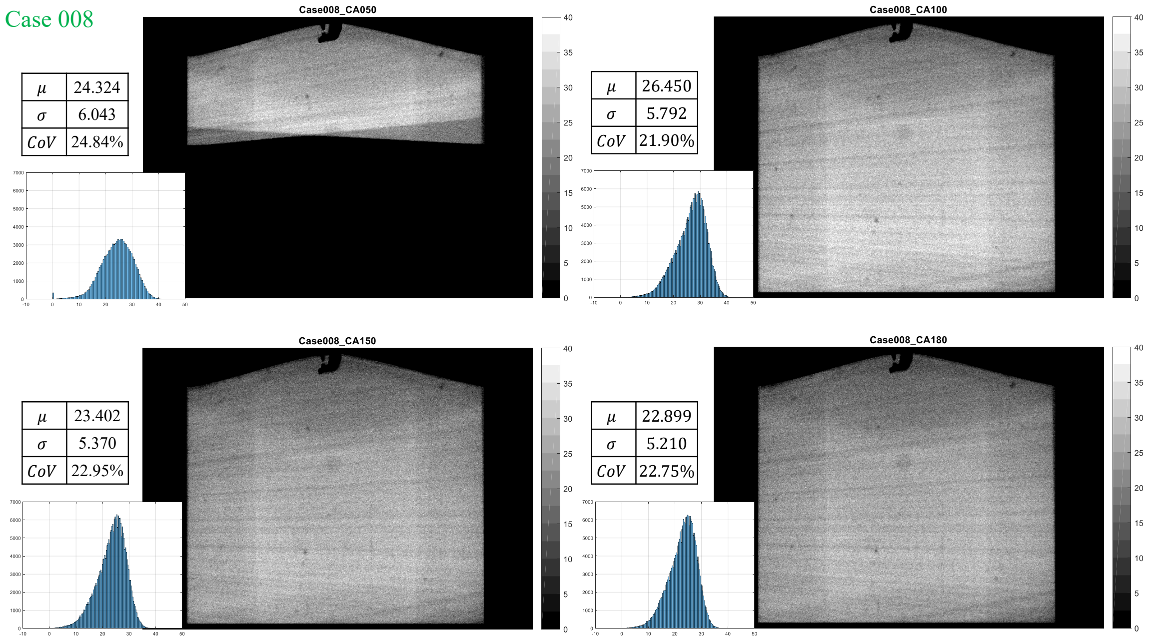

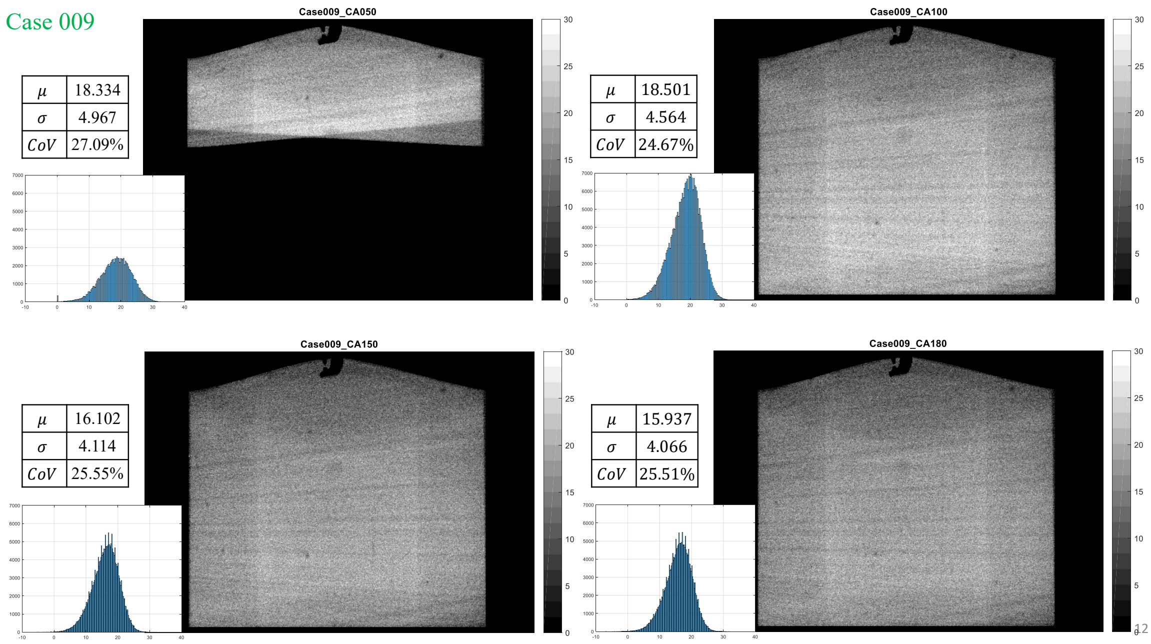

Case 010

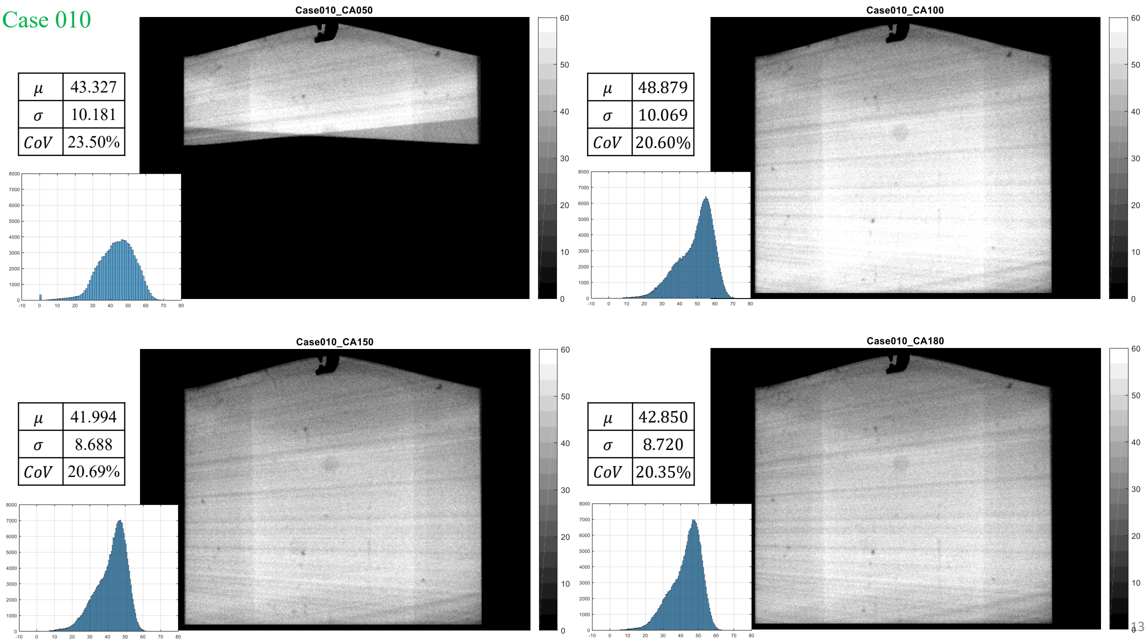

Case 011

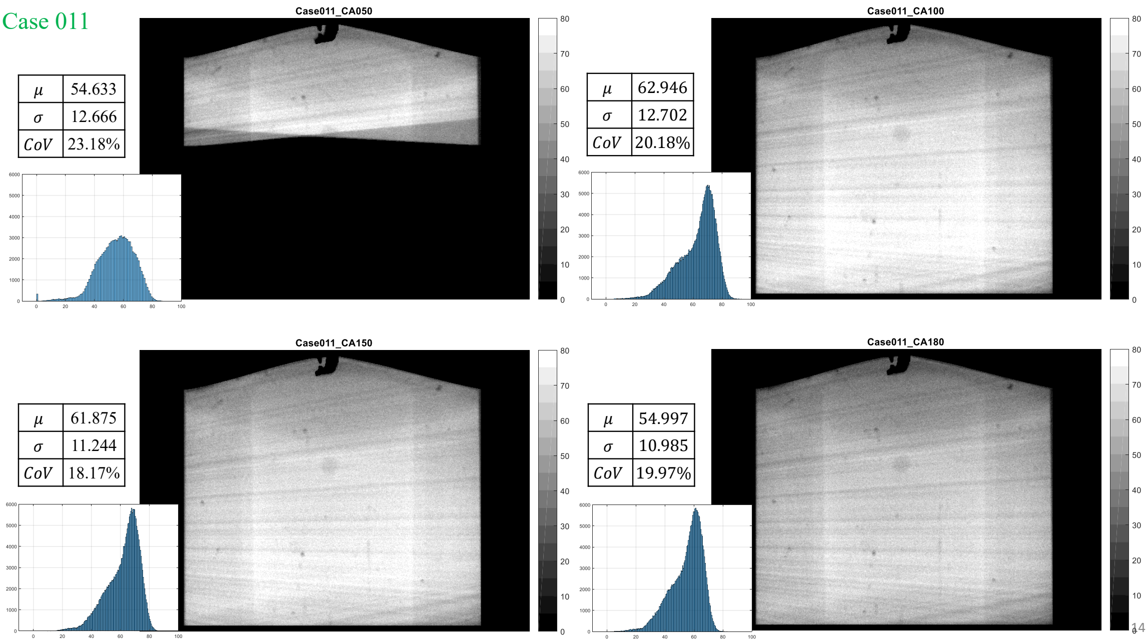

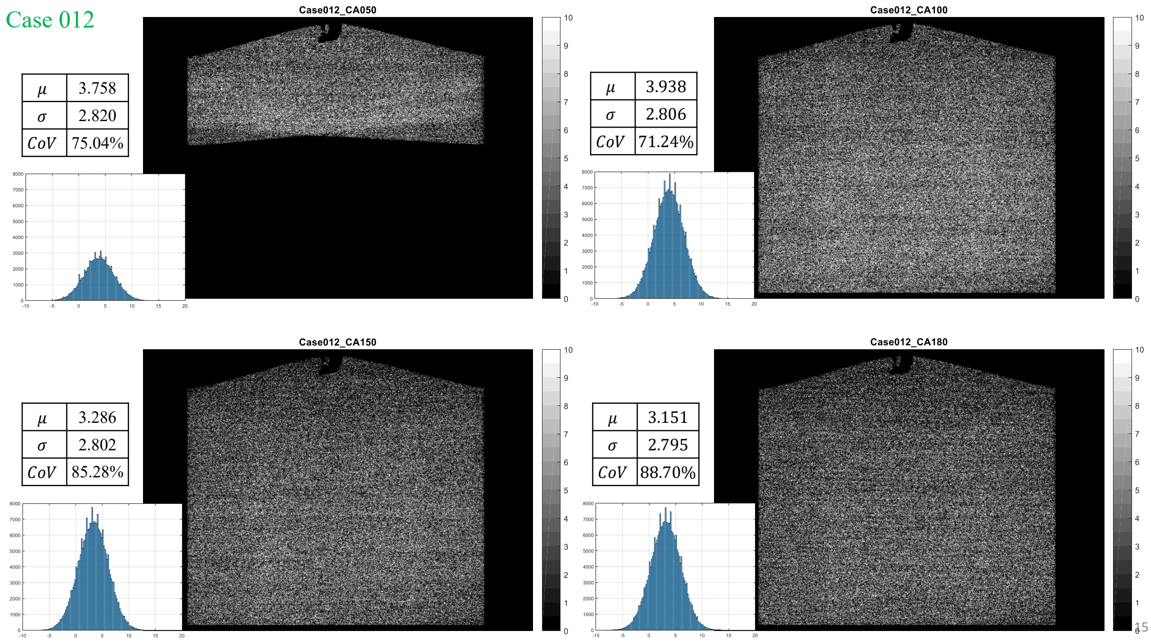
Case 012
Case012_CA050
μ 3.758
σ 2.820
CoV 75.04%
Case012_CA100
μ 3.938
σ 2.806
CoV 71.24%
Case012_CA150
μ 3.286
σ 2.802
CoV 85.28%
Case012_CA180
μ 3.151
σ 2.795
CoV 88.70%

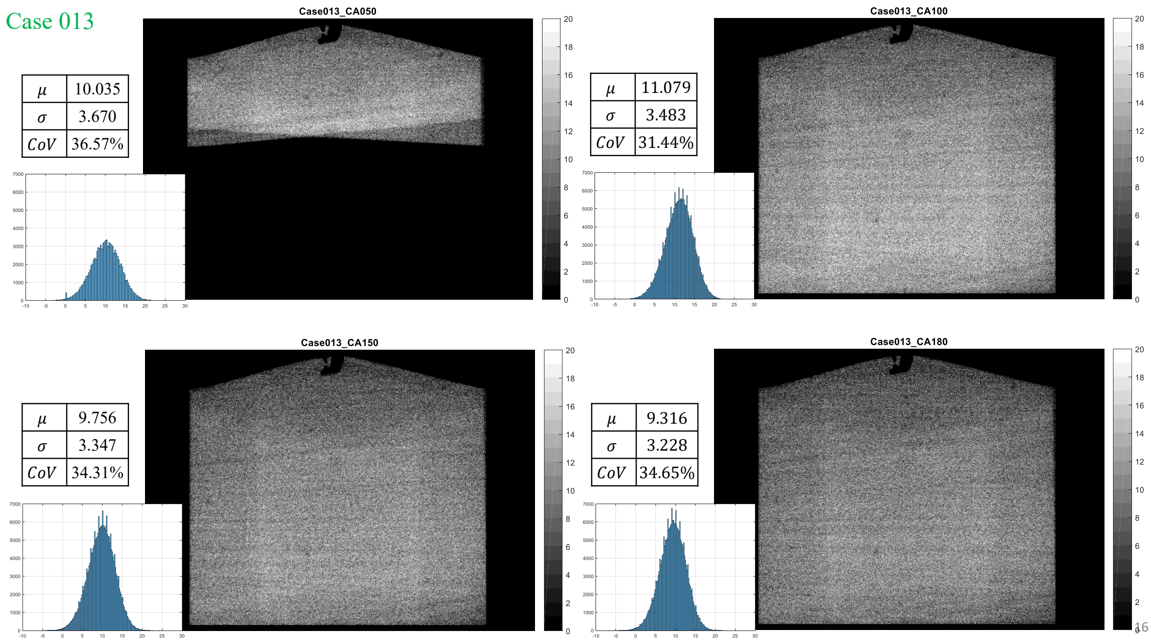
Case 013
Case013_CA050
μ 10.035
σ 3.670
CoV 36.57%
Case013_CA100
μ 11.079
σ 3.483
CoV 31.44%
Case013_CA150
μ 9.756
σ 3.347
CoV 34.31%
Case013_CA180
μ 9.316
σ 3.228
CoV 34.65%

C.2 PLIF images in fired condition

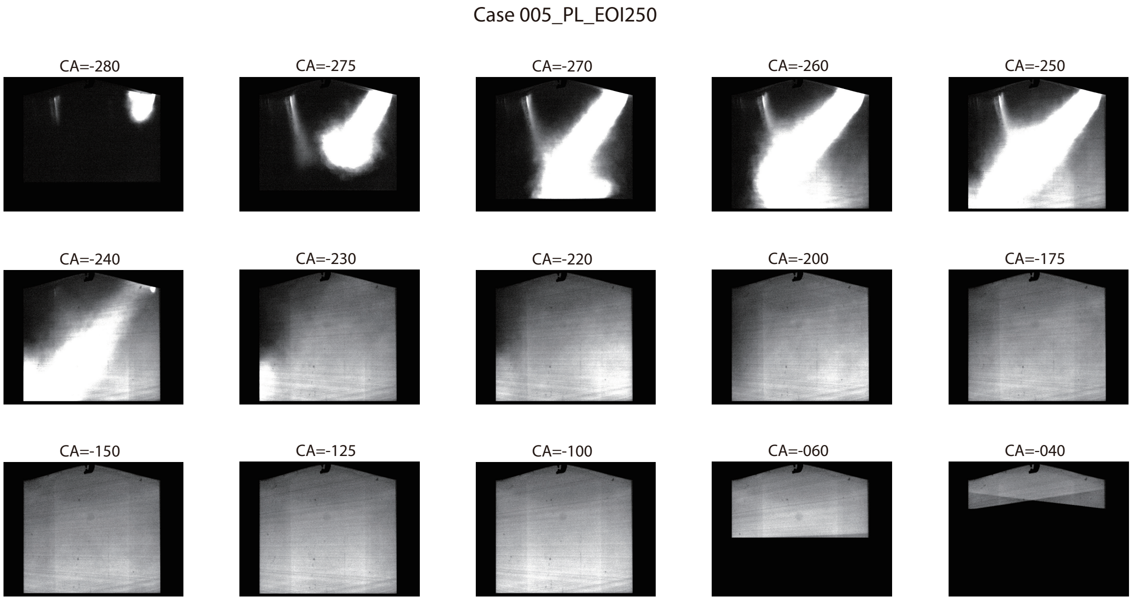

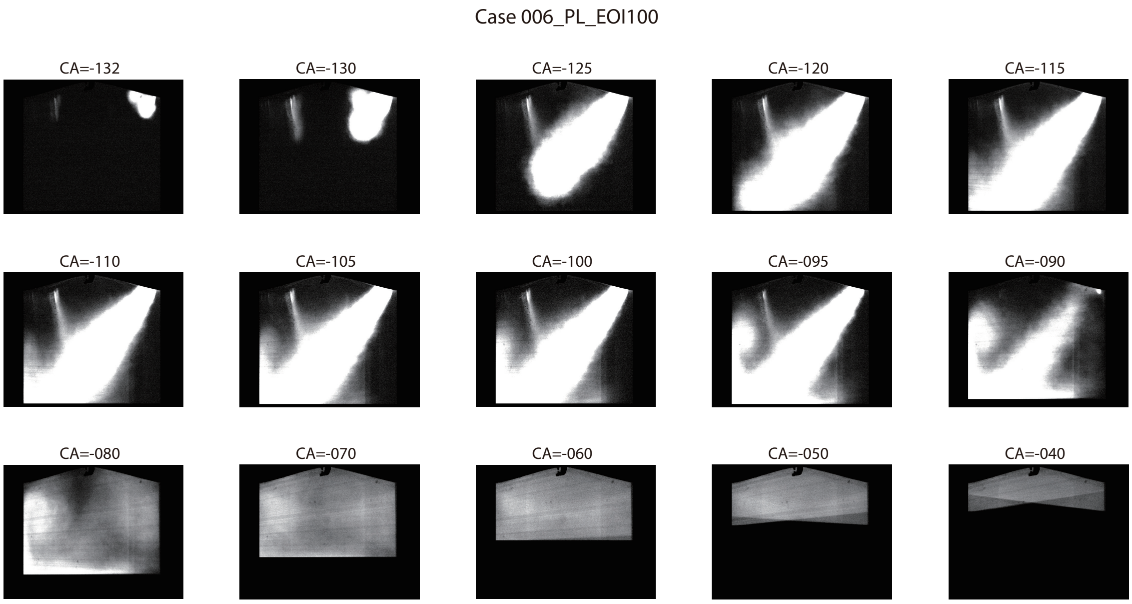

C.3 Equivalence ratio maps without correction

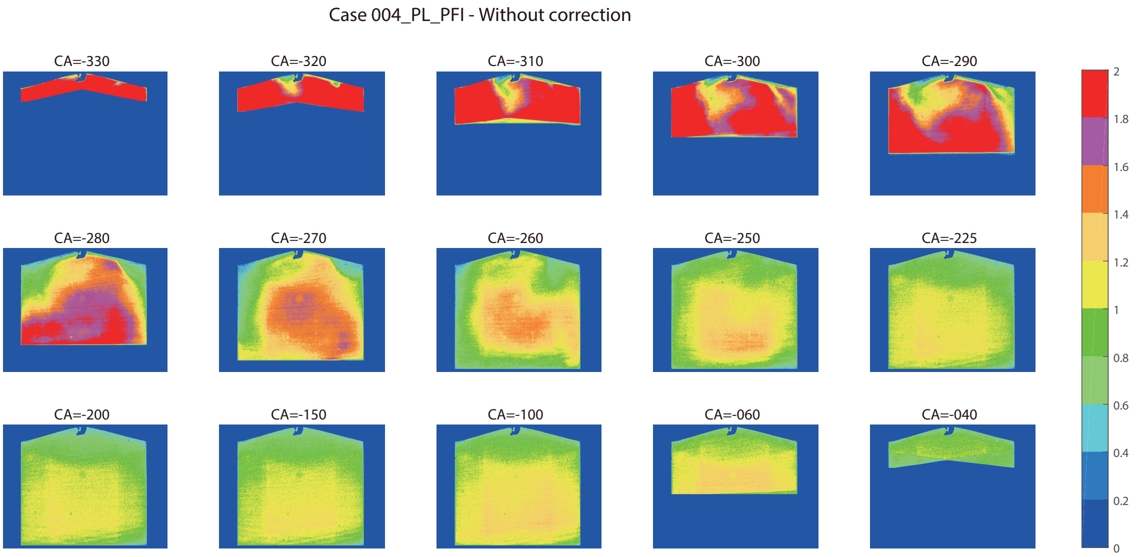

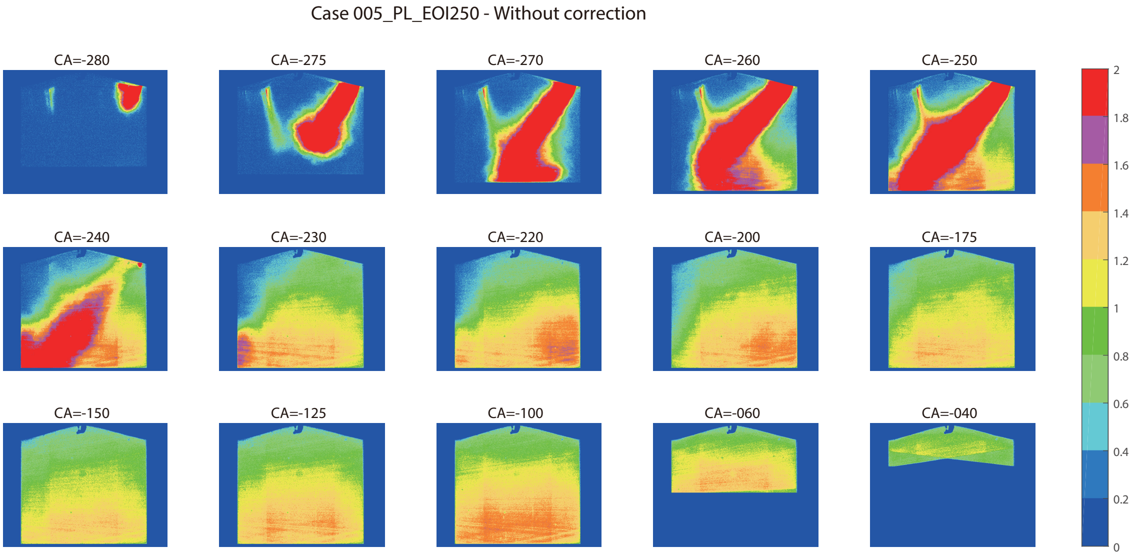

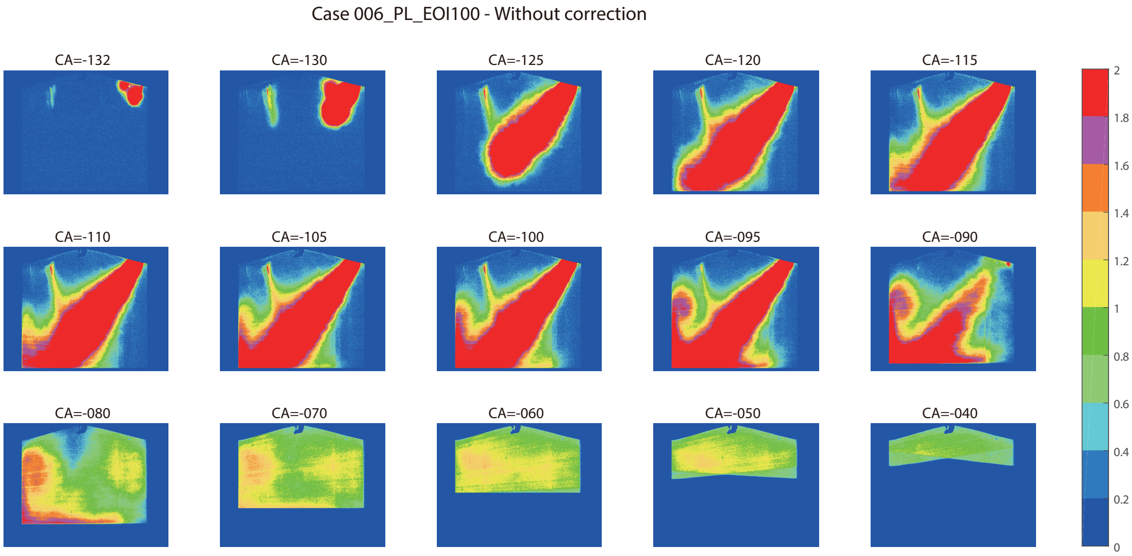
Case 006_PL_EOI100 - Without correction
CA=-132
CA=-130
CA=-125
CA=-120
CA=-115
CA=-110
CA=-105
CA=-100
CA=-095
CA=-090
CA=-080
CA=-070
CA=-060
CA=-050
CA=-040
2
1.8
1.6
1.4
1.2
1
0.8
0.6
0.4
0.2
0

C.4 Equivalence ratio maps with Reflection Correction

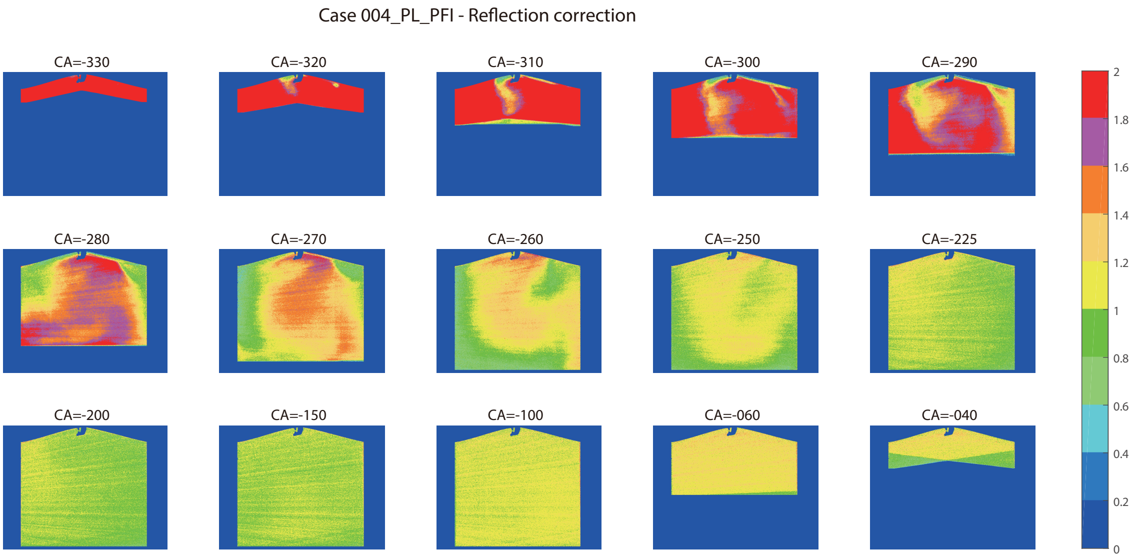

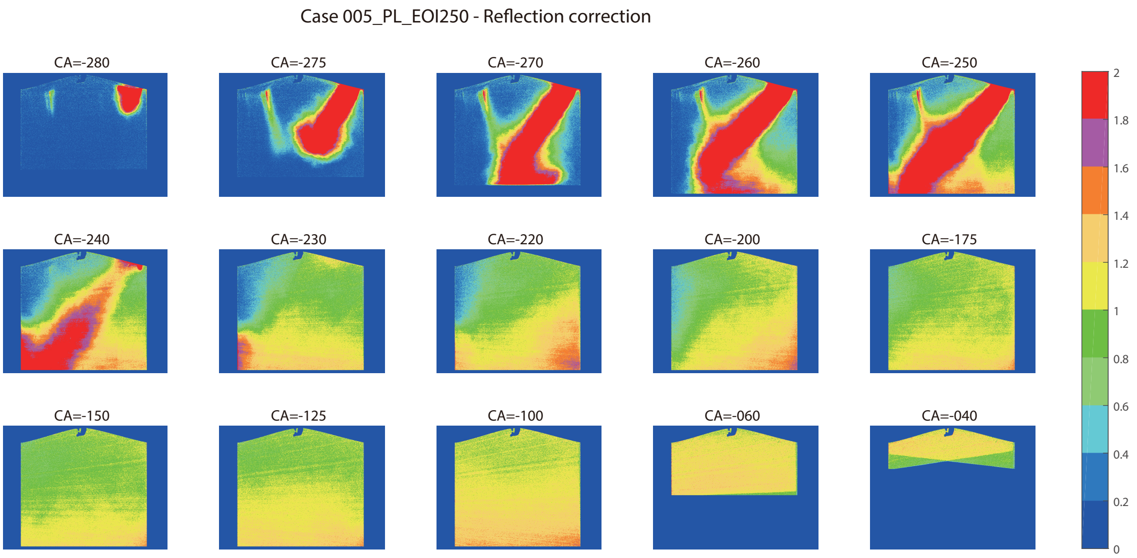

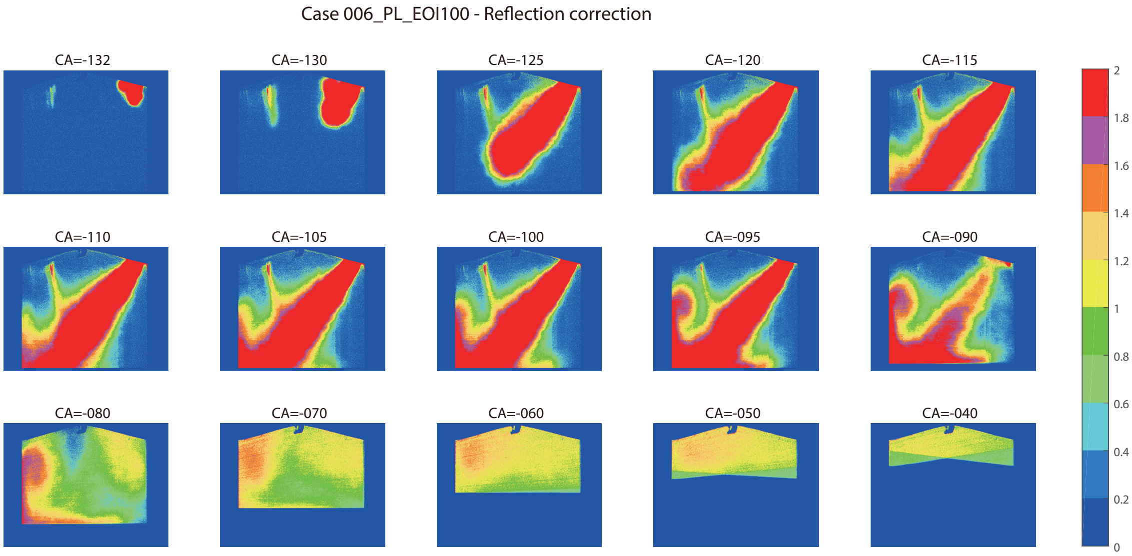
Case 006_PL_EOI100 - Reflection correction
CA=-132
CA=-130
CA=-125
CA=-120
CA=-115
CA=-110
CA=-105
CA=-100
CA=-095
CA=-090
CA=-080
CA=-070
CA=-060
CA=-050
CA=-040
2
1.8
1.6
1.4
1.2
1
0.8
0.6
0.4
0.2
0

C.5 Equivalence ratio maps with p & T Correction

Case 004_PL_PFI - p & T correction

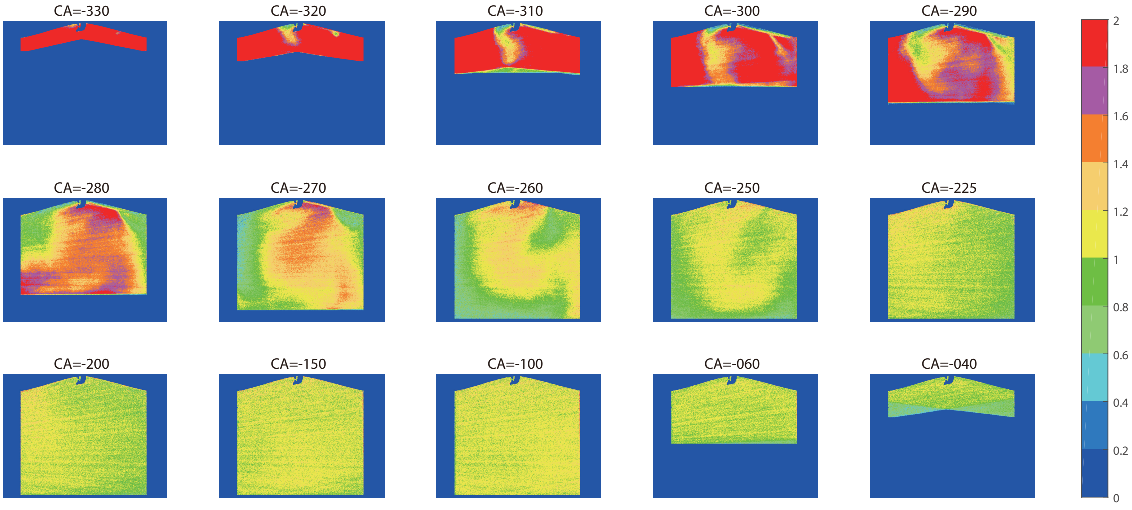

Case 005_PL_EOI250 - p & T correction

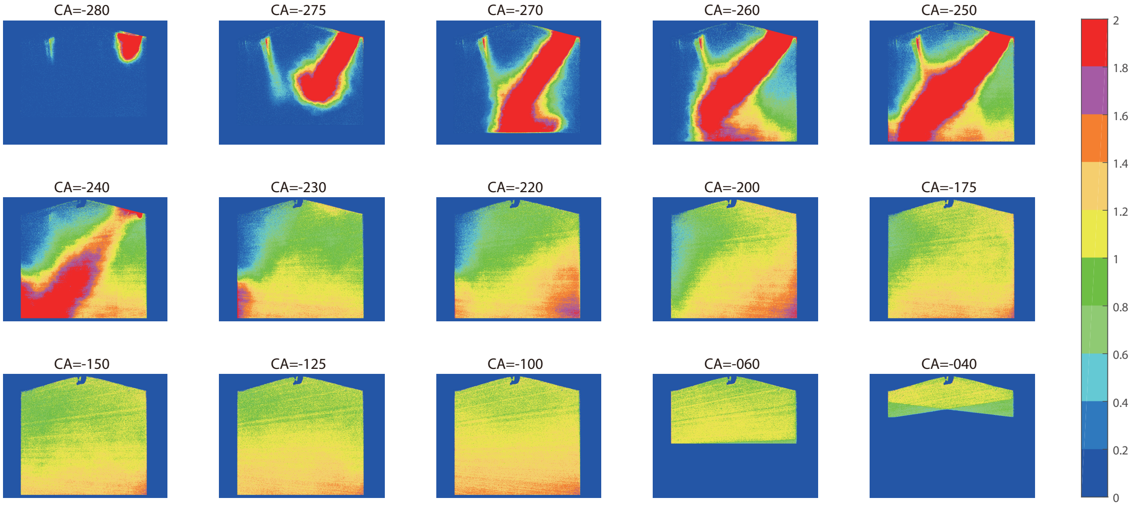

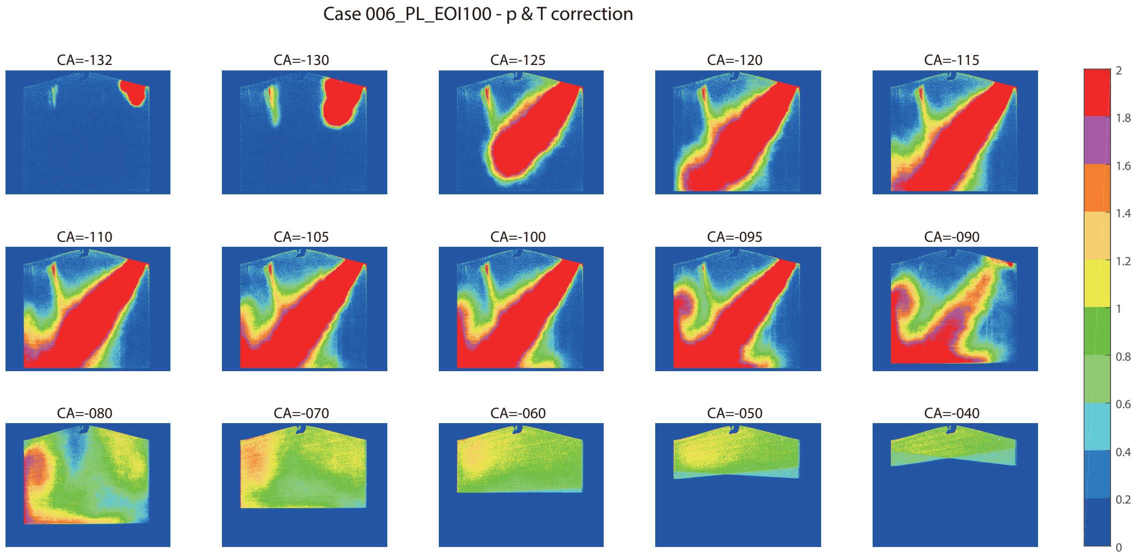
Case 006_PL_EOI100 - p & T correction
CA=-132
CA=-130
CA=-125
CA=-120
CA=-115
CA=-110
CA=-105
CA=-100
CA=-095
CA=-090
CA=-080
CA=-070
CA=-060
CA=-050
CA=-040
2
1.8
1.6
1.4
1.2
1
0.8
0.6
0.4
0.2
0

Bibliography

[1] Transport emissions | Climate Action:
https://ec.europa.eu/clima/policies/transport_en

[2] gason.eu | Project: http://www.gason.eu/page/index/project.

[3] Douailler, B., Ravet, F., Delpech, V., Soleri, D. et al., "Direct Injection of CNG on High Compression Ratio Spark Ignition Engine: Numerical and Experimental Investigation," SAE Technical Paper 2011-01-0923, 2011, https://doi.org/10.4271/2011-01-0923.

[4] http://www.informinc.org/pages/research/sustainable-transportation/reports/129.html

[5] Andamento storico prezzi e costi kmetrici | Costi carburanti - Dal 2005 la comunita italiana del metano per auto:
https://www.metanoauto.com

[6] Choongsik Bae and Jaeheun Kim. Alternative fuels for internal combustion engines. Proceedings of the Combustion Institute, 2016.

[7] Benefits of Natural Gas Vehicles | SoCalGas: https://www.socalgas.com/for-your-business/natural-gas-vehicles/benefits

[8] Baratta, M., & Rapetto, N. (2015). "Mixture formation analysis in a direct-injection NG SI engine under different injection timings". Fuel, 159, 675-688.

[9] R Ebrahimi and M Mercier. "Experimental study of performance of spark ignition engine with gasoline and natural gas". International Journal of Engineering, 24(2010):65 - 74, 2010.

[10] Chincholkar, S. P., & Suryawanshi, J. G. (2016). "Gasoline Direct Injection: An Efficient Technology". Energy Procedia, 90, 666-672.

[11] Investigation into Advanced Architecture and Strategies for Turbocharged Compressed Natural Gas Heavy Duty SI-engine.

[12] K. Keskinen, O. Kaario, M. Nuutinen, V. Vuorinen, Z. Kunsch, L.O. Liavag, M. Larmi, "Mixture formation in a direct injection gas engine: Numerical study on nozzle type, injection pressure and injection timing effects", Energy 94 (2016), 542-556.

[13] Li, Tie, Gao, Yi, Wang, Jiasheng, & Chen, Ziqian (2014). "The Miller cycle effects on improvement of fuel economy in a highly boosted, high compression ratio, direct-injection gasoline engine: EIVC vs LIVC". Energy Conversion and Management, 59-65.

[14] Millo, F., Luisi, S., Borean, F., & Stroppiana, A. (2014). "Numerical and experimental investigation on combustion characteristics of a spark ignition engine with an early intake valve closing load control". Fuel, 121, 298-310.

[15] Baratta, M., Rapetto, N., Spessa, E., Fuerhapter, A. et al., "Numerical and Experimental Analysis of Mixture Formation and Performance in a Direct Injection CNG Engine," SAE Technical Paper 2012-01-0401, 2012.

[16] Haslacher, R., Kirchweger, W., and Eichlseder, H., "Laser-Optical Methods for Diagnostics of NG Combustion Processes with Internal Mixture Formation (in German)", 8th Symposium on Engine Combustion - Current Problems and Modern Approaches, Munich, Germany, March 15-16, 2007.

[17] Star-CD v4.12 Methodology Manual, Computational Dynamics Ltd, 2009.

[18] Gamma Technologies. GT-SUITE - Engine Performance Tutorials, 2013.

[19] Performance Trends Inc | Valve Lash:
http://performancetrends.com/Definitions/Valve-Lash.htm

[20] Christof Schulza, Volker Sickb, "Tracer-LIF diagnostics: quantitative measurement of fuel concentration, temperature and fuel/air ratio in practical combustion systems", Progr. Energy Combust. Sci., Vol. 31, pp. 75-121, 2005.

[21] Fluorescence and Phosphorescence - Chemistry LibreTexts

[22] Zhao, H., and Laddomatos, N., "Optical Diagnostics for In-Cylinder Mixture Formation Measurements in IC Engines", Progr. Energy Combust. Sci., Vol. 24, pp. 297-336, 1998.

[23] Measurement of Fluorescence Quantum Yields on ISS Instrumentation Using Vinci:
http://www.iss.com/Measurement_Fluorescence_Quantum_Yields.pdf

[24] Koch JD, Hanson RK. Temperature and excitation wavelength dependencies of 3-pentanone absorption and fluorescence for PLIF applications. Appl Phys B 2003; 76:319-24.

[25] Koban W, Koch JD, Hanson RK, Schulz C. Absorption and fluorescence of toluene vapor at elevated temperatures. Phys Chem Chem Phys 2004; 6:2940-5.

[26] Thurber MC, Grisch F, Kirby BJ, Votsmeier M, Hanson RK. Measurements and modeling of acetone laser-induced fluorescence with implications for temperature-imaging diagnostics. Appl Opt 1998; 37:4963-78.

[27] Grossmann F, Monkhouse PB, Ridder M, Sick V, Wolfrum J. Temperature and pressure dependencies of the laser-induced fluorescence of gas-phase acetone and 3-pentanone. Appl Phys B 1996; 62:249-53.

[28] Hentschel W, Block B, Hovestadt T, Meyer H, Ohmstede G, Richter V, et al. Optical diagnostics and CFD-simulations to support the combustion process development of the Volkswagen FSI direct injection gasoline engine. SAE technical paper series 2001-01-3648; 2001.

[29] Reboux J, Puechberty D.: "A new approach of PLIF applied to fuel/air ratio measurement in the compression stroke of an optical SI engine", SAE technical paper, series 941988, 1994.

[30] KOBAN, Wieland; SCHULZ, Christof. Toluene laser-induced fluorescence (LIF) under engine-related pressures, temperatures and oxygen mole fractions. SAE Technical Paper, 2005.

[31] Fröba, AP and Rabenstein, F and Münch, K-U and Leipertz, A, "Mixture of triethylamine (TEA) and benzene as a new seeding material for the quantitative two-dimensional laser-induced exciplex fluorescence imaging of vapor and liquid fuel inside SI engines", Combustion and Flame, Vol. 112, pp. 199-209, 1998.

[32] Engel, S. R., Koch, P., Braeuer, A., & Leipertz, A. (2009). "Simultaneous laser-induced fluorescence and Raman imaging inside a hydrogen engine". Applied optics, 48(35), 6643-6650.

[33] Guillaume de Sercey, Graeme Awcock, Morgan Heikal: "Use of LIF image acquisition and analysis in developing a calibrated technique for in-cylinder investigation of the spatial distribution of air-to-fuel mixing in direct injection gasoline engines", Computers in Industry 56, pp. 1005-1015, 2005.

[34] G de Sercey, M Heikal, M Gold, S Begg, R Wood, G Awcock, and O Laguitton, "On the use of laser-induced fluorescence for the measurement of in-cylinder air-fuel ratios", Journal of Mechanical Engineering Science, Vol 216, Issue 10, pp. 1017-1029, 2002.